
The SoLid antineutrino detector: construction and commissioning with cosmic ray muons

Author

Céline Moortgat

Promotor

Prof. Dr. Dirk Ryckbosch

SCK•CEN Mentor

Dr. Lucia Popescu



SoLid



Preface

The SoLid experiment, located at the BR2 reactor at SCK•CEN, is designed to resolve the reactor antineutrino anomaly. This anomaly refers to a set of short-baseline reactor experiments, where, after a re-evaluation of the neutrino flux, the ratio of measured over predicted rate of antineutrinos deviates from unity at the 98.6 % C.L.. A result clearly in tension with the existing framework of three families of neutrinos oscillating into each other. Chapter 1 will provide more details on the existing neutrino framework and the anomalies.

The approach used by SoLid consists of a novel technique to detect reactor anti-neutrinos via the inverse beta decay interactions (IBD), combining $5 \times 5 \times 5 \text{ cm}^3$ PVT scintillator cubes equipped with ${}^6\text{LiF:ZnS(Ag)}$ neutron sensitive screens. This technology is explained in dept in chapter 2.

Chapter 3 discusses the SM1 prototype detector built at Ghent University in the summer of 2014. As a part of this thesis I was heavily involved in the construction and quality assurance of this detector. Despite a limited reactor-on data set collected in February 2015, a sub-optimal electronics system and a relatively low light-yield, the prototype was able to show that neutrons can be distinguished from other particle interactions. The results of the SM1 prototype lead to several design changes for the full-scale Phase 1 detector.

Since the SoLid experiment is located above ground, it will detect high rates of cosmic particles. These cosmic neutrons and muons can generate several backgrounds to the IBD signal and it is therefore very important to investigate these interactions. Chapter 4 provides information on a dedicated cosmic simulation package “CosmicGen”, developed as part of this thesis. A good agreement with SM1 data shows that the simulation chain is trustworthy and can thus provide valuable information on cosmic backgrounds.

The full-scale Phase 1 detector was built from December 2016 until November 2017 at Ghent University. The construction protocols and quality assurance are discussed in chapter 5. The procurement of materials, training of

manpower and the construction and quality control of the detector took up a large part of this thesis.

In October 2017, 4 out of 5 Phase 1 modules were transported to the BR2 reactor. After a relatively short installation and commissioning period, the detector was able to collect reactor-on and -off data in December. This dataset was used as a burn sample for the proto-IBD analysis group. The goal of this group was to understand the basic properties of the detector by performing initial studies of the data quality, object reconstruction, backgrounds and to perform an initial IBD search.

Chapter 6 discusses the reconstruction of the muon objects, performed within the scope of this thesis. These reconstructed muons were used as the basis of a muon veto in the IBD search of the proto-IBD group. Analysis of the muons could also indicate a stable behaviour of the detector. Coincidence studies of muons with Michel electrons and neutrons resulted, respectively, in a value of the muon decay time and of the neutron capture time on the Li screens.

The results of the proto-IBD group were able to show a good understanding of the Phase 1 detector and provide a decent basis for further studies that will be performed within the SoLid Collaboration. It is expected that SoLid will be able to provide an explanation for the reactor antineutrino anomaly within a few years of data taking. Thereby either rejecting or confirming the existence of the sterile neutrino, one of the most enigmatic particles in physics.

Contents

Preface	iii
1 The road to sterile neutrinos	1
1.1 Standard Model of particle physics	2
1.2 History of neutrinos	4
1.3 Neutrino oscillations	7
1.3.1 Solar neutrinos	7
1.3.2 Atmospheric neutrinos	8
1.3.3 Oscillation parametrisation	8
1.3.4 Measurements	11
1.4 Neutrino anomalies	16
1.4.1 The accelerator anomaly	17
1.4.2 The Gallium anomaly	17
1.4.3 The reactor anomaly	19
1.4.4 The 5 MeV spectral distortion	19
1.5 Sterile neutrinos	21
1.5.1 Parameterisation extension	22
1.5.2 Current status	23
1.6 Next-generation experiments	24
1.7 Conclusion	29
2 SoLid	31
2.1 Belgian Reactor 2	31
2.2 SoLid technology	34
2.2.1 Antineutrino interaction	34
2.2.2 Composite scintillator cubes	35
2.3 Detectors	36
2.4 Conclusion	39

3	The SM1 prototype	41
3.1	SM1 properties	42
3.2	Construction and protocols	45
3.3	Proton content	46
3.4	Frame commissioning	48
3.5	Data taking and analyses	49
3.6	Conclusion	53
4	Simulation of cosmic rays	55
4.1	CosmicGen	56
4.1.1	CosmicGen muon files	57
4.1.2	CosmicGen neutron files	63
4.1.3	Settings for the CosmicGen files used in Geant4	65
4.2	SM1 data and simulation comparison for muons	71
4.3	Muons and “after-muon” events in SM1	72
4.4	Conclusion	81
5	Phase 1 detector	83
5.1	Lessons learned from SM1	83
5.2	Phase 1 properties	84
5.3	Construction and protocols	88
5.3.1	$^6\text{LiF:ZnS}$ screens protocol	89
5.3.2	Cube construction protocol	89
5.3.3	Frame construction protocol	93
5.4	Frame commissioning with Calipso	100
5.5	Conclusion	103
6	Cosmic ray induced backgrounds in Phase 1	105
6.1	Cosmic simulations	106
6.2	DAQ settings	107
6.3	Object reconstruction	108
6.3.1	Neutron selection	109
6.3.2	SPEak and SEvent Finding	110
6.3.3	Muon identification	112
6.3.4	Muon efficiency	113
6.3.5	Muon rates and environmental correlations	116
6.4	Muon tracking	121
6.5	“After-muon” events	126
6.5.1	Michel electrons	127
6.5.2	Spallation neutrons	132

<i>CONTENTS</i>	vii
6.6 Conclusion	136
7 Conclusion	139
8 Nederlandstalige samenvatting	143
ALOA (A Lot Of Abbreviations)	147
List of Figures	149
List of Tables	155
Bibliography	157

The road to sterile neutrinos

1

Since the existence of mankind, people have been anxious to learn about the world surrounding them. Even the history of particle physics can be traced back to the ancient Greeks who first wondered about atoms and conservation of matter. The word 'atom' itself was conceived by Democritus in 400BC and translates to 'indivisible'. Even then this indestructible nature of atoms was subject to heavy debate. A discussion only to be solved at the turn of the 19th century.

At that time J. Thompson put forward his plum-pudding model of the atom [1], a positive sphere with electrons embedded therein, after his discovery of the electron in 1897 [2]. In fact, at the start of the 20th century, most physicists believed that they understood the fundamental principles of nature quite well, based on Newtonian mechanics and with atoms as the building blocks of nature. However, radical proposals, such as Einsteins theory of general relativity, made it clear that the scientific knowledge at that time was far from complete.

Thompson's atomic model was disproved by Rutherford's alpha-scattering experiment in 1911, showing that the atom consists of a small positively charged nucleus surrounded by electrons [3]. But after the discovery of the proton by Rutherford in 1919 [4], and the neutron by Chadwick in 1932 [5], the idea of a nucleus as elementary particle changes yet again. And the story does not stop here: with the advent of particle accelerators in the 60's it was finally proven that the neutron and proton itself are composites of quarks, a theory proposed by Gell-Mann [6] and Zweig [7]. Meanwhile, technological advancements marked the beginning of a true particle explosion. To find order in the different particle types, a mathematical scheme started to take form, the basis of the Standard Model of particle physics.

Now, more than 60 years later, this Standard Model of interactions and particles, which will be discussed in sec. 1.1, is supported by many experimental results and therefore widely accepted. However, some inconsistencies still remain, see for example section 1.4, and one could wonder: have we yet again arrived at a moment in time where we think to understand the lion's share about the universe, only to discover at the next turn that we need to alter our knowledge completely?

1.1 Standard Model of particle physics

The Standard Model of particle physics (SM) describes all known elementary particles. The matter particles can be split into 2 groups, the leptons and the quarks. All these particles are fermions, meaning that they have half-integer spin values. Each particle has a corresponding antiparticle with the same mass but opposite quantum numbers to those shown in table 1.1. Every charged lepton has a corresponding neutrino. Both leptons and quarks can be divided in 3 generations or families, whereby the second and third generations can be regarded as a heavier version of the first. Particles of the first family are the constituents of ordinary matter that surrounds us in day-to-day life. Only in high-energy environments, such as cosmic rays and particle accelerators, particles of the higher families are present.

Hadrons are particles that consist of quarks. Together they represent the so-called hadron zoo. Protons (1 up quark and 2 down quarks) and neutrons (2 up quarks and 1 down quark) are examples of hadrons that each contain 3 quarks, the so-called baryons. Particles that consist of 2 quarks (a quark and an antiquark) are called mesons, such as the kaons and pions.

The SM incorporates not only the fermions, but also integer spin particles. These are the bosons that mediate the forces between particles. There are 4 fundamental forces in the universe: the weak, the electromagnetic, the strong and the gravitational force. Only the first 3 forces and their corresponding bosons are described in the SM as it has proven impossible to include gravity in this framework. The theory of general relativity that describes the macro-world and the theory of quantum mechanics used to describe the micro-world seem to be mathematically incompatible [8]. Fortunately, the effect of gravity on the scale of elementary particles is negligible.

The strong force acts solely on quarks as the gluon force carrier only couples to particles with a colour charge, see table 1.1. The strong force is responsible for binding quarks together in hadrons. The electromagnetic force carrier is the photon and only couples to electrically charged particles, the quarks and charged leptons. This force is a.o. responsible for magnetic at-

Table 1.1: The elementary fermions [9].

Fermions	Generation	Name	Symbol	Mass (MeV/c ²)	Charge (e)	Weak isospin	Colour
Quarks	1	up	u	~2.3	+2/3	+1/2	r, g, b
		down	d	~4.8	-1/3	-1/2	r, g, b
	2	charm	c	~1.28 × 10 ³	+2/3	+1/2	r, g, b
		strange	s	~95	-1/3	-1/2	r, g, b
	3	top	t	173.5 × 10 ³	+2/3	+1/2	r, g, b
		bottom	b	4.7 × 10 ³	-1/3	-1/2	r, g, b
Leptons	1	electron	e	0.511	-1	-1/2	-
		electron neutrino	ν_e	< 2.2 × 10 ⁻⁶	0	+1/2	-
	2	muon	μ	105.7	-1	-1/2	-
		muon neutrino	ν_μ	< 0.19	0	+1/2	-
	3	tau	τ	1.777 × 10 ³	-1	-1/2	-
		tau neutrino	ν_τ	< 18.2	0	+1/2	-

traction and the propagation of light. The weak force is carried by the W and the Z bosons, which couple to weak isospin and therefore to all elementary fermions. The weak force explains for example some forms of radioactivity and the energy production in the sun. An overview of the fundamental forces and the particles to which they couple can be found in figure 1.1. In this figure one can also find the final element of the Standard Model, the Higgs-boson.

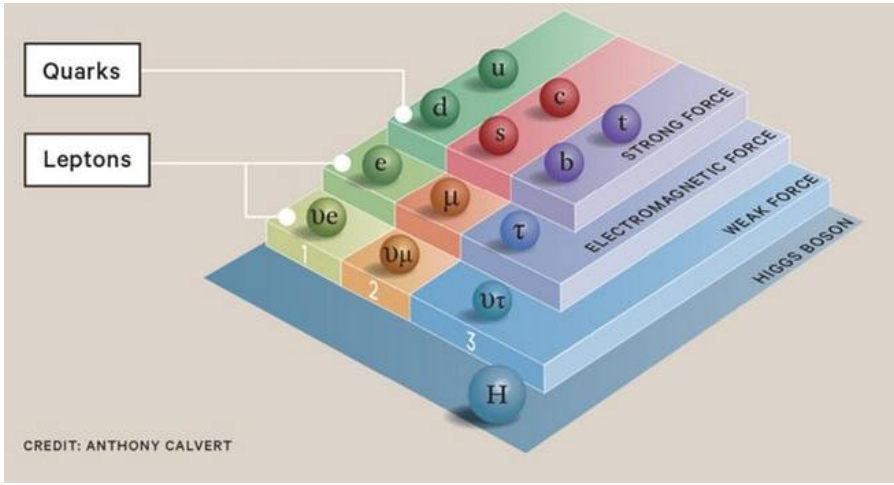


Figure 1.1: The elementary particles and forces of the Standard Model of particle physics [10].

The Higgs particle was only recently discovered in 2012 by both the CMS [11] and ATLAS [12] experiments at the Large Hadron Collider (LHC) at CERN. It is a spin-0 particle and plays a very important role in the SM; it provides the mechanism by which other fundamental particles acquire mass [13]. However, the neutrino masses are much smaller than the masses of the other elementary particles, which might indicate the existence of another mechanism for generating the neutrino mass. The seesaw mechanism provides an explanation for the smallness of these masses. An overview of this mechanism and its many different extensions can be found in [14].

1.2 History of neutrinos

Neutrinos are elusive particles, interacting only via the weak interaction, which makes them very hard to detect. Therefore they have been the subject of much research. They were only discovered decades after their existence

was proposed by Pauli in 1930. With this suggestion he wanted to explain the beta decay experimental results. The beta decay interaction, without neutrino involved, would simply be the conversion of a neutron into a proton with the creation of an electron, also called “beta particle”:



The kinetic energy of the electron would be fixed and equal to the energy released in the beta decay $Q_{\beta} = M_{(A,Z)} - M_{(A,Z+1)} - m_e$. However, experimental results showed a continuous beta energy spectrum, with an end energy of Q_{β} , see figure 1.2. The existence of an undetected neutral particle that carries away a fraction of the energy was proposed as an explanation for the observed energy loss. Thereby improving the beta decay formula to:

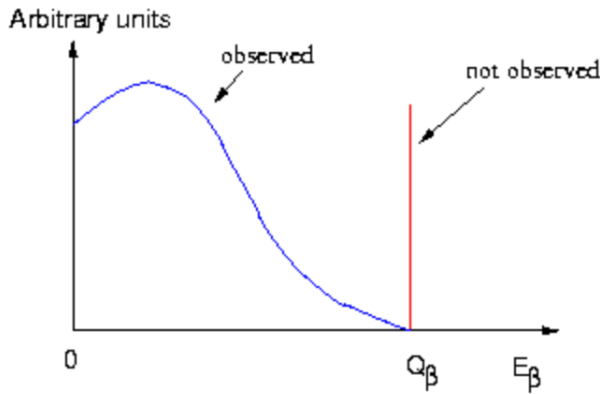
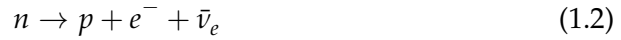


Figure 1.2: The kinetic energy spectrum of the emitted electron in β -decay process (observed). If no antineutrino is emitted, the total available energy would be carried by the electron and we would observe a peak at $E_{\beta}=Q_{\beta}$ (not observed) [15].

E. Fermi developed a beta decay theory by building on Pauli’s idea. He named the particle “neutrino”, meaning “little neutral one” in Italian, and stated that it was massless [16].

With the rise of nuclear reactors, powerful antineutrino sources with an expected flux of 10^{12} to 10^{13} neutrinos per second per cm^2 became available. Because neutrinos are so weakly interacting a source of this intensity

is needed to perform neutrino experiments. A first neutrino search was attempted by F. Reines and C. Cowan at the Hanford reactor and later at the Savannah River Plant. The detector was a big tank of water with a neutron-absorber additive, cadmium chloride. Reactor antineutrinos interacting with protons in the tank would create a neutron and a positron, known as the inverse beta decay (IBD):



High backgrounds and low counting rates caused several months delay, but the existence of a free antineutrino was finally announced in 1956 [17]. On account of their discovery Cowan and Reines received the Nobel Prize in Physics in 1995.

The detection of muon neutrinos took place in 1962, when the Alternating Gradient Synchrotron (AGS) was constructed. The AGS was able to produce a high-energy proton beam, that in turn could create a pion (π) beam when directed on a beryllium target. The pions would consequently decay into muons, which would then be detected in a spark chamber, and muon neutrinos:



L. Lederman, M. Schwartz and J. Steinberger received the Nobel Prize in Physics in 1988 for the demonstration of the lepton doublet structure and the discovery of the muon neutrino [18].

Evidence that could indicate the decay of a new heavy lepton was published by M. Perl in 1975 [19]. This lepton was symbolised by the character τ , derived from the greek word $\tau\rho\iota\tau\omicron\nu$ (triton), which means “third”. The third generation neutrino, ν_τ , was only discovered in 2000 by the DONUT Collaboration [20].

Through the measurement of the Z boson lifetime in 1989 it was confirmed that there are exactly 3 types of light weakly-interacting neutrinos [21]. The more particles the Z boson can decay to, the larger the width of this distribution and the shorter its lifetime. In figure 1.3 the mass distribution of the Z boson is shown and it is clear that the curve corresponding to 3 neutrino flavors matches the data best. The discovery of the six quarks over the course of several decades shows a similar 3 family structure. This simplicity and symmetry adds to the confidence in the Standard Model scheme.

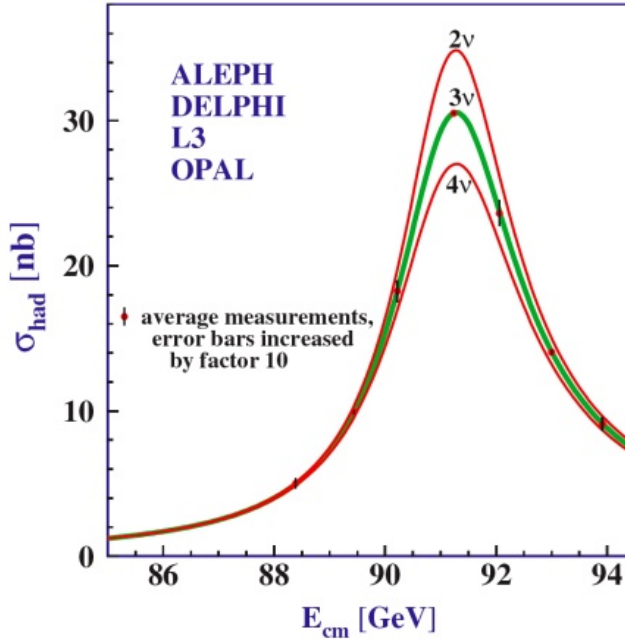


Figure 1.3: Points indicating the measured mass distribution of the Z boson. The lines are predictions corresponding to the different N_ν hypotheses [22].

1.3 Neutrino oscillations

1.3.1 Solar neutrinos

Aside from nuclear reactors, it was assumed that the sun is also a powerful source of neutrinos due to the nuclear fusion reactions that take place inside [23]:



To prove that the sun runs on thermonuclear power R. Davis and J. Bahcall designed the Homestake experiment. In this experiment a huge tank of cleaning fluid was deployed deep underground as a target for the IBD interaction of solar neutrinos. However, the first published results [24] showed a considerable difference between the amount of predicted and measured neutrinos. This discrepancy was dubbed the “solar neutrino problem”. Several explanations were proposed, such as a problem with the detection, a faulty prediction of the captured neutrino rate or a misunderstanding of the so-

lar interior. However, in combination with similar results obtained by the Kamiokande experiment in 1989 [25], an issue with neutrino physics seemed the more likely cause of the solar neutrino problem.

1.3.2 Atmospheric neutrinos

Cosmic rays collide with nuclei in the atmosphere, thereby creating showers that hit the earth at a steady rate. These showers contain mostly pions that decay into a muon and a muon-neutrino. Consecutively, the muon decays into an electron, an electron-neutrino and a muon-neutrino.

$$\pi \rightarrow \mu + \nu_{\mu} \quad (1.6)$$

$$\mu \rightarrow e + \nu_e + \nu_{\mu} \quad (1.7)$$

These equations show that one expects a 2:1 ratio of muon- to electron-neutrinos coming from cosmic rays, but experimental results are not in agreement. The Irvine-Michigan-Brookhaven detector obtained a ratio of 0.54 ± 0.13 and the Kamiokande Collaboration 0.60 ± 0.08 [26]. The combination of these results with the solar neutrino problem gives a strong indication for new physics.

1.3.3 Oscillation parametrisation

Neutrino oscillations could explain both the solar and atmospheric neutrino anomalies discussed in sections 1.3.1 and 1.3.2. The former problem could be clarified by a solar electron-neutrino changing into a different type of neutrino before interacting with the detector on earth. Similarly, the lack of atmospheric muon-neutrinos could be resolved by muon-neutrinos changing into a different flavour.

Neutrino oscillations were proposed in 1967 by B. Pontecorvo [27] by stating that lepton family number was not a conserved quantity. This also implied that neutrinos are not massless, and furthermore, that all neutrino flavours would have a different mass. This was a first indication of physics beyond the Standard Model.

It were Pontecorvo, Maki, Nakagawas and Sakata who described the theoretical extension to the SM to include the oscillation of neutrinos. Therein each neutrino flavour is in fact a superposition of 3 mass eigenstates. As neutrinos interact with matter, for example when they are created, they have a definite flavour, but this changes after they have travelled a certain distance. This is due to the different rates at which the quantum mechanical phases of the mass eigenstates progress, resulting in a different superposition of mass

states and thereby also a different flavour at distinct times. The neutrinos with a definite mass ($|\nu_i\rangle$, with $i = 1,2,3$) can be related to the neutrinos with a definite flavour ($|\nu_\alpha\rangle$, with $\alpha = e, \mu, \tau$) by a unitary transformation [28]:

$$|\nu_i\rangle = \sum_\alpha U_{\alpha i}^* |\nu_\alpha\rangle \quad (1.8)$$

$$|\nu_\alpha\rangle = \sum_i U_{\alpha i} |\nu_i\rangle \quad (1.9)$$

Where $U_{\alpha i}$ represents the PMNS matrix, named after the theorists mentioned before.

$$U_{\alpha i} = \begin{pmatrix} U_{e1} & U_{e2} & U_{e3} \\ U_{\mu1} & U_{\mu2} & U_{\mu3} \\ U_{\tau1} & U_{\tau2} & U_{\tau3} \end{pmatrix}$$

The matrix can be parametrised with four real parameters $\theta_{12}, \theta_{23}, \theta_{13}$ and δ :

$$U_{\alpha i} = \begin{pmatrix} c_{12}c_{13} & s_{12}c_{13} & s_{13}e^{-i\delta} \\ -s_{12}c_{23} - c_{12}s_{23}s_{13}e^{i\delta} & c_{12}c_{23} - s_{12}s_{23}s_{13}e^{i\delta} & s_{23}c_{13} \\ s_{12}s_{23} - c_{12}c_{23}s_{13}e^{i\delta} & -c_{12}s_{23} - s_{12}c_{23}s_{13}e^{i\delta} & c_{23}c_{13} \end{pmatrix}$$

Where $c_{ij} = \cos \theta_{ij}$, $s_{ij} = \sin \theta_{ij}$. The parameter δ still remains to be determined. A non-zero value would only be expected in the case that neutrino oscillations violate CP symmetry¹.

An interesting simplification is the case of just 2 oscillating neutrinos [30], for example $|\nu_e\rangle$ and $|\nu_\mu\rangle$. At a given time, the true mass eigenstates $|\nu_1\rangle$ and $|\nu_2\rangle$ are just a linear combination:

$$|\nu_1\rangle = \cos \theta |\nu_\mu\rangle - \sin \theta |\nu_e\rangle \text{ and } |\nu_2\rangle = \sin \theta |\nu_\mu\rangle + \cos \theta |\nu_e\rangle \quad (1.10)$$

Analogously:

$$|\nu_e\rangle = \cos \theta |\nu_1\rangle + \sin \theta |\nu_2\rangle \text{ and } |\nu_\mu\rangle = -\sin \theta |\nu_1\rangle + \cos \theta |\nu_2\rangle \quad (1.11)$$

¹When CP symmetry is valid, the fundamental laws of physics remain the same when a particle is interchanged by its antiparticle (C symmetry) and the spatial coordinates are inverted (P symmetry) [29].

The mass eigenstates propagate according to the Schrödinger equation in time as plane waves:

$$|v_i(t)\rangle = |v_i(0)\rangle e^{-iE_i t/\hbar} \quad (1.12)$$

Assume that at time $t = 0$ the particle starts out as an electron-neutrino:

$$|v_e(0)\rangle = 1, |v_\mu(0)\rangle = 0 \text{ so } |v_1(0)\rangle = -\sin\theta, |v_2(0)\rangle = \cos\theta \quad (1.13)$$

Substituting eq. 1.13 in eq. 1.12 and solving eq. 1.11 for $|v_\mu\rangle$:

$$|v_\mu\rangle = \sin\theta \cos\theta (e^{-iE_1 t/\hbar} + e^{-iE_2 t/\hbar}) \quad (1.14)$$

To calculate the probability that the neutrino, which was produced as an electron-neutrino, has converted into a muon-neutrino after time t :

$$P_{v_e \rightarrow v_\mu} = [\sin(2\theta) \sin(\frac{E_2 - E_1}{2\hbar} t)]^2 \quad (1.15)$$

For highly relativistic particles with a mass m and momentum p it is possible to make the approximation $E \approx p + m^2/2p$. Substituting the former and replacing t by the distance travelled L in natural units, eq. 1.15 becomes:

$$P_{v_e \rightarrow v_\mu} = [\sin(2\theta) \sin(\frac{m_2^2 - m_1^2}{4E} L)]^2 \quad (1.16)$$

This equation shows the need for non-zero and different neutrino masses to allow neutrino oscillations.

In general, the probability that a neutrino of flavour α , with an energy E , will be detected as a neutrino of flavour β after travelling a distance L , is given by [28]:

$$\begin{aligned} P_{v_\alpha \rightarrow v_\beta} = & \delta_{\alpha\beta} - 4\sum_{i>j} \text{Re}(U_{\alpha i}^* U_{\beta i} U_{\alpha j} U_{\beta j}^*) \sin^2\left(\frac{\Delta m_{ij}^2 L}{4E}\right) \\ & + 2\sum_{i>j} \text{Im}(U_{\alpha i}^* U_{\beta i} U_{\alpha j} U_{\beta j}^*) \sin\left(\frac{\Delta m_{ij}^2 L}{2E}\right) \end{aligned} \quad (1.17)$$

Where $\Delta m_{ij}^2 = m_i^2 - m_j^2$ (with m_i the neutrino masses), is a parameter known as the mass splitting. This formula is valid for any number of neutrinos.

In the case of the SM with 3 oscillating neutrinos, there are 2 distinct mass splittings: $\Delta m_{21}^2 = m_2^2 - m_1^2$ and $\Delta m_{32}^2 = m_3^2 - m_2^2$. Oscillation experiments can

be used to determine these values. However, it is not possible to measure the ordering of the masses. This is known as the mass hierarchy problem and is one of the big open questions in particle physics. In figure 1.4 the 2 mass ordering possibilities are depicted: the normal hierarchy $m_1 < m_2 < m_3$ and the inverted hierarchy $m_3 < m_1 < m_2$. In both cases $m_1 < m_2$ as this was confirmed by the observation of the MSW effect [31], [32].

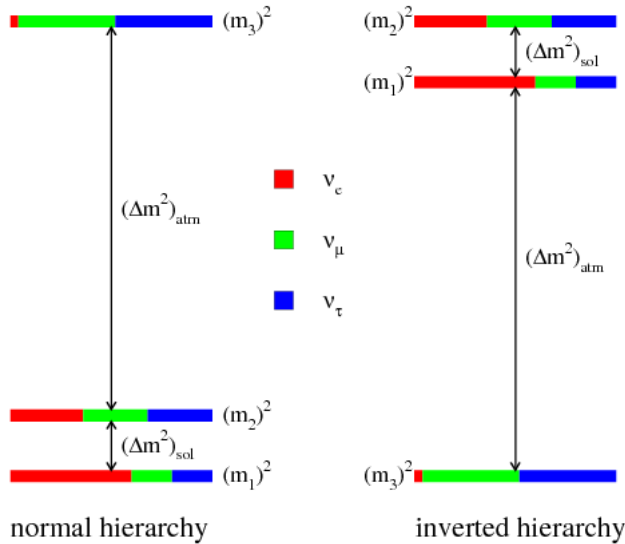


Figure 1.4: The normal and inverted mass hierarchy [33].

Also indicated are $\Delta m_{sol}^2 = \Delta m_{21}^2$ and $\Delta m_{atm}^2 = |\Delta m_{32}^2| \approx |\Delta m_{31}^2|$, depicting the mass splitting related to solar and atmospheric mixing. As will be shown in section 1.3.4, measurements of the mixing angle θ_{13} and the mass difference Δm_{21}^2 indicate very small values. Therefore it is possible to make an approximation in the case of solar and atmospheric oscillations, by assuming respectively the mixing of $\nu_e \leftrightarrow \nu_x$ (where ν_x is a superposition of ν_τ and ν_μ) and $\nu_\mu \leftrightarrow \nu_\tau$. This reduces to the 2 oscillating neutrino approximation discussed earlier, whereby the oscillation probability is given by formula 1.15.

1.3.4 Measurements

Although neutrino oscillations were already predicted in the late 1960's, it took until 1998 for the first results consistent with neutrino oscillations to

become published [34]. This research was done by the Super-Kamiokande experiment (see figure 1.5) looking at the zenith angle distribution of atmospheric muon-neutrinos. The atmospheric ν_μ were detected via the charged-current (CC) interaction on oxygen in the water detector tank and by observing the final state muon:



It was noted that muon-neutrinos coming from above the detector were more numerous than neutrinos coming from below. This can be interpreted as follows: neutrinos that traverse through the entire earth and enter the detector through the bottom have more chance to oscillate in a different type of neutrino. This result solved the atmospheric neutrino problem.

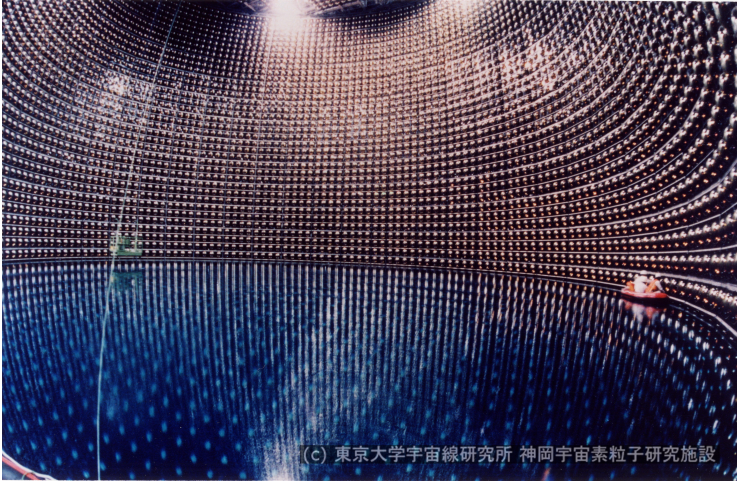


Figure 1.5: Inside view of the 50 000 ton water detector tank of the Super-Kamiokande experiment [35].

Oscillations as the cause of the solar neutrino problem were confirmed in 2001 by the Sudbury Neutrino Observatory (SNO) experiment [36]. This set-up, consisting of a vessel containing 1000 tons of heavy water, is shown in figure 1.6. Due to the relatively low binding energy (2.2 MeV) of the deuteron compared to solar neutrino energies, the CC interaction



is kinematically allowed. While the charged-current interaction is only sensitive to the ν_e component, the neutral-current (NC) interaction is sensitive

to the total neutrino flux. In the NC interaction the neutrino breaks up the deuteron in a proton and a neutron. This neutron will eventually be captured on another deuteron, producing a photon which will be detected in the SNO vessel.

The electron-neutrino rate measured in SNO was, as in previous experiments, too low to match theoretical predictions. However, the total rate was consistent with the theoretical solar neutrino rate. This showed that aside from ν_e , also ν_μ and ν_τ interacted in the detector. Since these latter particles are not created by fusion processes in the sun, they were clearly the result of neutrino oscillations. Note that this measurement could not be performed by the Super-Kamiokande collaboration as oxygen, in contrast to the deuteron, is a very stable nucleus and the CC interaction is not kinematically allowed for solar neutrino energies.



Figure 1.6: The Sudbury Neutrino Observatory 12m diameter vessel [37].

Since, and even before, the confirmation of neutrino oscillations, many experiments set out to measure the neutrino oscillation parameters. In table 1.2 the results of a recent (2014) global fit of neutrino oscillations can be found [38]. The data have been obtained with experiments performed at different neutrino sources. The observation of reactor, solar, atmospheric and accelerator neutrinos provides sensitivities to different oscillation parameters. Moreover, one can look for signatures of neutrino oscillations in 2 ways. Indications can be found in the disappearance of the flavour in question, for

example observing less muons than expected from a pure ν_μ -beam. Alternatively one can look for the appearance of an unexpected flavour, such as the measurement of electrons or tau's from a pure ν_μ -beam.

Table 1.2: Neutrino oscillation parameters. For Δm_{31}^2 , $\sin^2 \theta_{23}$, $\sin^2 \theta_{13}$ and δ the upper (lower) row corresponds to the normal (inverted) neutrino mass hierarchy [38].

Parameter	Best fit	3σ range
$\Delta m_{21}^2 [10^{-5} \text{eV}^2]$	7.60	7.11-8.18
$\Delta m_{31}^2 [10^{-3} \text{eV}^2]$	2.48	2.30-2.65
	2.38	2.20-2.54
$\sin^2 \theta_{12}$	0.323	0.278-0.375
$\sin^2 \theta_{23}$	0.567	0.393-0.643
	0.573	0.403-0.640
$\sin^2 \theta_{13}$	0.0226	0.0190-0.0262
	0.0229	0.0193-0.0265
δ	1.41π	0.00- 2.00π
	1.48π	0.00- 2.00π

As mentioned before, nuclear reactors are powerful neutrino sources. They provide a pure $\bar{\nu}_e$ source with a mean energy of a few MeV. Because of this low energy a neutrino oscillating into another flavour would not be detectable, since the threshold for muon or tau production in the final charged-current state is much higher. One can therefore only observe oscillations through the disappearance of $\bar{\nu}_e$. This can be expressed as, see [13] for derivation:

$$P_{\bar{\nu}_e \rightarrow \bar{\nu}_e} = 1 - \cos^4(\theta_{13}) \sin^2(2\theta_{12}) \sin^2\left(\frac{\Delta m_{21}^2 L}{4E}\right) - \sin^2(2\theta_{13}) \sin^2\left(\frac{\Delta m_{32}^2 L}{4E}\right) \quad (1.20)$$

There are 2 components present in the oscillation, one with a short wavelength with amplitude $\sin^2(2\theta_{13})$, depending on Δm_{32}^2 and a long-wavelength component fixed by Δm_{21}^2 . The former occurs on the scale of a few km, while the latter can be measured at the order of a few 100 km.

One of the first experiments measuring the long-wavelength oscillation, was KamLAND, co-located with Super-Kamiokande. By detecting neutrinos from several reactors located in the range of 130-240 km distance they

were able to determine the value of Δm_{21}^2 and $\sin^2(2\theta_{12})$. These parameters can also be found by measuring solar neutrinos. Experiments as SNO and Super-Kamiokande have added to the measurement precision shown in table 1.2. The allowed contours in neutrino oscillation parameter space from both KamLAND and solar experiments can be found in figure 1.7.

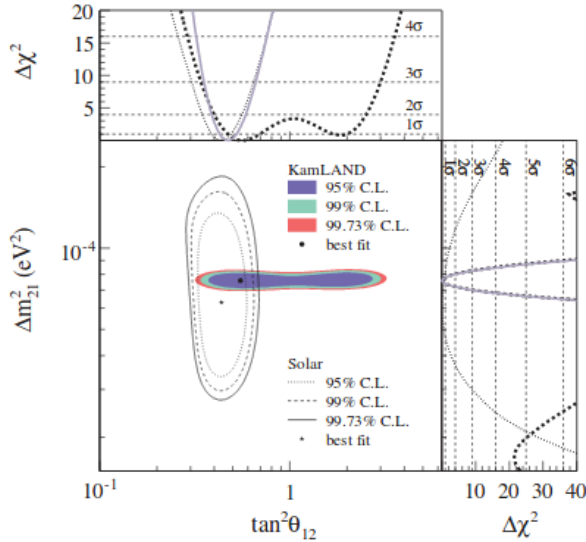


Figure 1.7: Allowed neutrino oscillation parameter space from solar neutrino experiments and KamLAND [39].

To access the other oscillation parameters, one needs different L/E . Experiments with atmospheric and beam neutrinos are suitable to access Δm_{32}^2 and $\sin^2 \theta_{23}$ by studying the survival probability of the muon-neutrinos [13]:

$$P_{\nu_\mu \rightarrow \nu_\mu} \approx 1 - [\sin^2(2\theta_{23}) \cos^4(\theta_{13}) + \sin^2(2\theta_{13}) \sin^2(\theta_{23})] \sin^2\left(\frac{\Delta m_{32}^2 L}{4E}\right) \quad (1.21)$$

One of the experiments investigating the oscillation of beam neutrinos is MINOS, with an L/E value of the order of 500 km/GeV. The allowed neutrino oscillation parameter space from the MINOS experiment can be seen in figure 1.8. Also indicated are the results of Super-Kamiokande, obtained by observing the disappearance of atmospheric neutrinos.

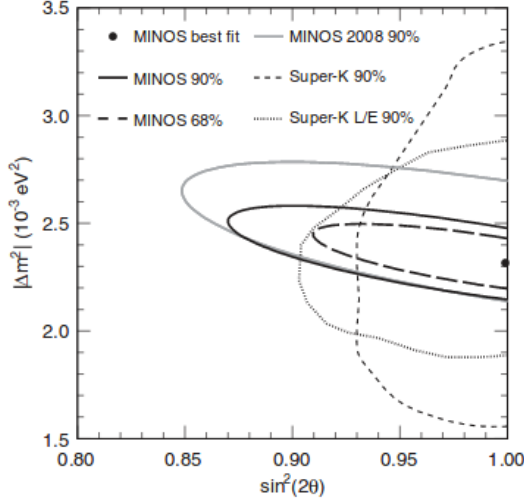


Figure 1.8: Allowed neutrino oscillation parameter space ($\sin^2 \theta_{23}$ and Δm_{32}^2) from the MINOS and Super-Kamiokande experiment [40].

It can be shown that neutrino beam experiments such as MINOS are also capable of measuring δ and $\sin^2(2\theta_{13})$ by investigating ν_e appearance data. However, short baseline, $\mathcal{O}(\text{km})$, reactor experiments give more significant values for the latter parameter by measuring the $\bar{\nu}_e$ disappearance:

$$P_{\bar{\nu}_e \rightarrow \bar{\nu}_e} \approx 1 - \sin^2(2\theta_{13}) \sin^2\left(\frac{\Delta m_{32}^2 L}{4E}\right) \quad (1.22)$$

The most significant results come from the Daya Bay [41] and RENO reactor [42] experiments. The RENO results are shown in figure 1.9.

1.4 Neutrino anomalies

As discussed in the previous sections, there is much experimental evidence for the 3 oscillating neutrino framework and it is therefore widely accepted. Nonetheless, there are several experimental results that are in tension with this theory. These issues are named the neutrino anomalies.

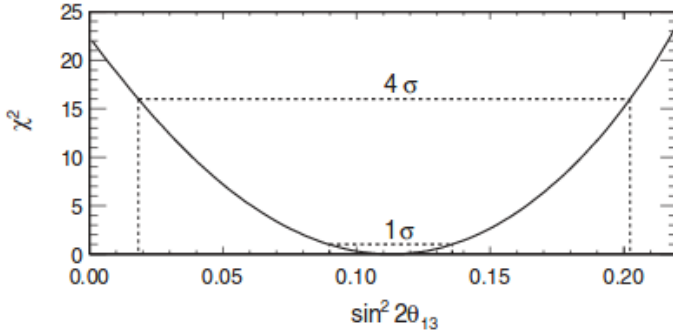


Figure 1.9: RENO χ^2 distribution as a function of $\sin^2(2\theta_{13})$ [42].

1.4.1 The accelerator anomaly

The first inconsistent data sets were found by the Liquid Scintillator Neutrino Detector (LSND) experiment. Using the accelerator at the Los Alamos Meson Physics Facility, the collaboration searched for the $\bar{\nu}_\mu \rightarrow \bar{\nu}_e$ appearance using $\bar{\nu}_\mu$ from μ^+ decay. The electron-antineutrinos were detected via the IBD interaction inside a 167 ton tank filled with mineral oil and organic scintillator. A 3.8σ excess of $\bar{\nu}_e$ was found [43].

The MiniBooNE experiment at Fermilab was designed to confirm or dispute the LSND results. At a similar L/E ($\mathcal{O}(1 \text{ m/MeV})$) as the LSND experiment both $\bar{\nu}_\mu \rightarrow \bar{\nu}_e$ and $\nu_\mu \rightarrow \nu_e$ searches were performed. The former search is consistent with the results obtained by the LSND. The latter channel shows a 3.0σ ν_e excess for $E_\nu^{QE} < 475 \text{ MeV}$, while there is no excess reported for higher energies [44]. The MicroBooNE experiment, currently taking data, will provide more insight into this low energy excess.

The $\bar{\nu}_e$ excesses reported in this section are referred to as the accelerator anomaly.

1.4.2 The Gallium anomaly

The GALLEX [45] and SAGE [46] experiments have been very important in uncovering the solar neutrino problem discussed in section 1.3.1. To be able to trust the measurements pointing towards a deficit of solar neutrinos, it was necessary to perform some calibration tests of the gallium detectors. These were performed by placing radioactive sources with known activity levels inside the detectors and measuring the produced electron neutrinos. The sources that were used during these test were ^{51}Cr and ^{37}Ar , which both

decay via electron capture:



The emitted ν_e are detected by the same mechanism as solar neutrinos:



The average ratio R^{Ga} of measured over predicted ${}^{71}\text{Ge}$ rates for both SAGE and GALLEX is [14]:

$$R^{Ga} = 0.86 \pm 0.05 \quad (1.26)$$

Thus showing a 2.8σ deficit of measured neutrinos, which is known as the gallium anomaly. Taking into account the large uncertainty on the neutrino cross-sections, a deficit of 1.8σ still remains. Figure 1.10 shows the ratios R^{Ga} for the different measurements.

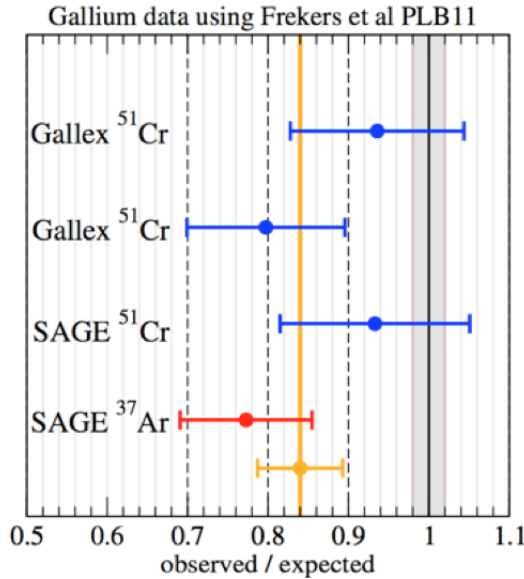


Figure 1.10: The observed deficit of neutrinos in radioactive source experiments [47].

1.4.3 The reactor anomaly

Many reactor neutrino experiments have been performed over the past few decades to establish the parameters of the 3 oscillating neutrino framework, see section 1.3.4. Amongst these are experiments placed at relatively short distances from the reactor cores (<100 m): ILL-Grenoble, Bugey, Goesgen, ROVNO, Krasnoyarsk and Savannah River [48], [49], [50]. The ratio of measured over predicted rate of reactor antineutrinos was in agreement with 1:

$$R^{\bar{\nu}_e} = 0.976 \pm 0.024 \quad (1.27)$$

However, during the preparations for the Double Chooz experiment in 2011, the neutrino flux was reevaluated taking into account new information on the decay of thousands of fission products, leading to a new ratio of [51]:

$$R^{\bar{\nu}_e} = 0.934 \pm 0.024 \quad (1.28)$$

Resulting in a deviation from unity at 98.6% C.L., in other words: a 5.7% deficit of reactor antineutrinos, called the reactor antineutrino anomaly (RAA). The rate ratios of several reactor experiments are shown in figure 1.11, while figure 1.12 shows the ratios versus reactor-detector distance.

Flux predictions are very difficult, requiring contributions from hundreds to thousands of fission products of the uranium and plutonium isotopes inside the reactor core. A fault in these calculations is therefore often suspected as the cause of the anomaly. Although it could also be explained by the presence of a sterile neutrino, further discussed in section 1.5.

1.4.4 The 5 MeV spectral distortion

Aside from the 3 neutrino anomalies mentioned in the previous sections, another unexpected artefact shows up in some reactor neutrino data sets. The Double Chooz experiment, 2 detectors located at the Chooz nuclear power plant, reported a distortion in the energy spectrum of the prompt signal coming from the IBD interaction of the reactor antineutrinos in the detector. The spectrum is shown in figure 1.13 where an excess of 3.0σ between 4.25 and 6 MeV and a 1.6σ deficit between 6 and 8 MeV can be seen [53]. It was also shown that the amplitude of the excess shows strong correlation with the reactor power. The so-called “5 MeV spectral distortion” was confirmed by RENO, where 2 detectors were placed at the Hanbit reactors, and the Daya Bay experiment, with 8 detector modules at the Daya Bay reactor cluster [54]. Combining these results leads to a $\approx 4 \sigma$ distortion of the spectrum.

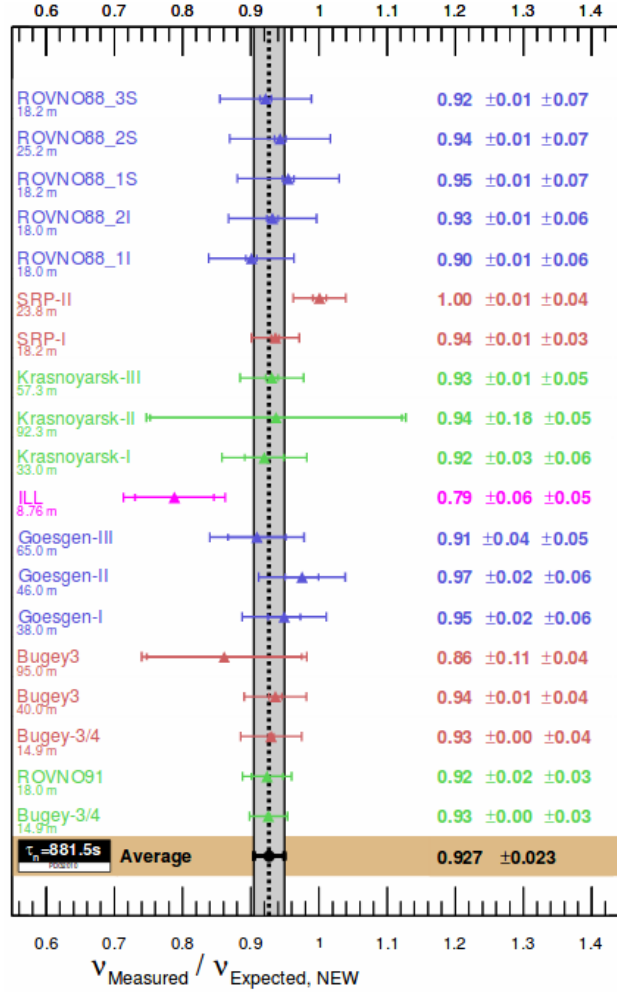


Figure 1.11: R^{ν_e} measurements at several short baseline reactor neutrino experiments [14].

Because of the dependence on reactor power the most likely cause of the distortion seems to be an error in the reactor flux calculations. It remains to be determined whether 1 fissile isotope or multiple fission fragments are responsible and several experiments set out to tackle this issue by performing measurements at reactors with different fuel contents. A combined analysis of the NEOS and Daya Bay results concludes at the 3-4 σ significance level that ^{239}Pu and ^{241}Pu are unlikely to be the single source of the 5 MeV bump.

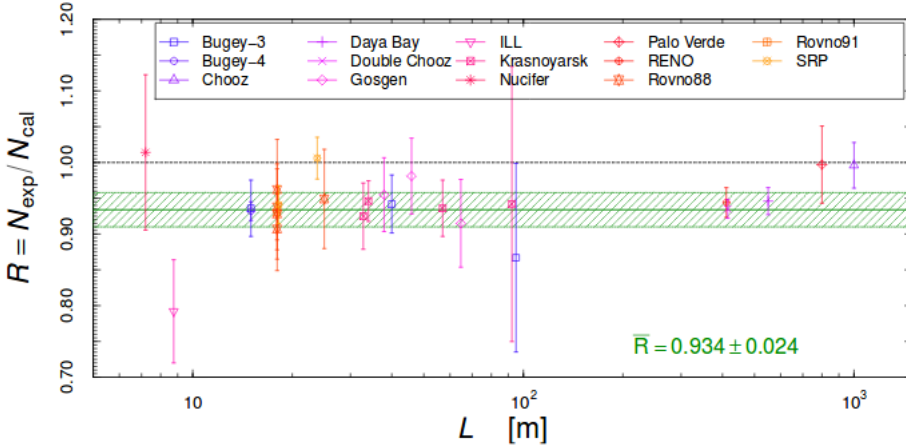


Figure 1.12: $R^{\bar{\nu}_e}$ measurements versus reactor-detector distance for several short baseline reactor neutrino experiments [52].

In fact, a preference is found for ^{235}U to be the sole origin [55]. It would therefore be highly interesting to investigate a prompt energy spectrum at a highly ^{235}U enriched core to identify the origin of the spectral distortion.

1.5 Sterile neutrinos

Taking into account all the anomalies discussed in section 1.4, discovered with different detection techniques and at different neutrino sources, new physics beyond the Standard Model seems to be a possible explanation. The LSND result in itself already suggests this as the measurement, discussed in section 1.4.1, can be interpreted as a neutrino oscillation with a Δm^2 of about 1 eV^2 . Since the atmospheric and solar oscillations correspond to $\Delta m_{atm}^2 \approx 2.48 \cdot 10^{-3} \text{ eV}^2$ and $\Delta m_{sol}^2 \approx 7.6 \cdot 10^{-5} \text{ eV}^2$ respectively, see table 1.2, the LSND results require a fourth neutrino. As mentioned in section 1.2, it was measured that the Z-boson couples to only 3 neutrinos. A fourth neutrino would therefore not interact weakly and is thus dubbed a “sterile” neutrino. The reactor and gallium anomalies are also compatible with the sterile neutrino hypothesis, as an oscillation of reactor/source neutrinos into the sterile state would explain the observed deficit.

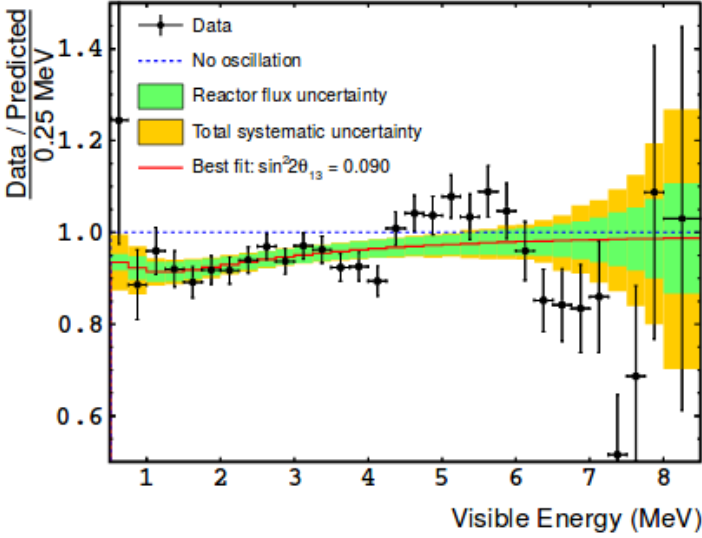


Figure 1.13: Black points show the ratio of the data, after subtraction of the background, to the non-oscillation prediction as a function of the visible energy of the prompt signal. Overlaid red line is the rate of the best-fit to the non-oscillation prediction with the reactor flux uncertainty (green) and total systematic uncertainty (orange) [53].

1.5.1 Parameterisation extension

To include 1 sterile neutrino $|\nu_s\rangle$ (3+1 neutrino mixing) in the parametrisation discussed in section 1.3.3, a fourth mass state $|\nu_4\rangle$ needs to be introduced. Altering the PMNS matrix to:

$$U_{\alpha i} = \begin{pmatrix} U_{e1} & U_{e2} & U_{e3} & U_{e4} \\ U_{\mu1} & U_{\mu2} & U_{\mu3} & U_{\mu4} \\ U_{\tau1} & U_{\tau2} & U_{\tau3} & U_{\tau4} \\ U_{s1} & U_{s2} & U_{s3} & U_{s4} \end{pmatrix}$$

The sterile neutrino is mainly composed of this fourth mass state and therefore $\Delta m_s^2 = \Delta m_{41}^2$. As $m_4 \gg m_1, m_2, m_3$:

$$\sqrt{\Delta m_{41}^2} \approx m_4 \quad (1.29)$$

In the case of 3+1 mixing, the appearance and disappearance probabilities in short baseline (SBL) reactor experiments are given by [14]:

$$P_{\nu_\alpha \rightarrow \nu_\beta} = \sin^2(2\theta_{\alpha\beta}) \sin^2\left(\frac{\Delta m_{41}^2 L}{4E}\right) \quad (\alpha \neq \beta) \quad (1.30)$$

$$P_{\nu_\alpha \rightarrow \nu_\alpha} = 1 - \sin^2(2\theta_{\alpha\alpha}) \sin^2\left(\frac{\Delta m_{41}^2 L}{4E}\right) \quad (1.31)$$

Where $\theta_{\alpha\beta}$ and $\theta_{\alpha\alpha}$ are effective oscillation angles. In the case of electron antineutrino disappearance this angle is often represented by θ_{ee} . The formulas show that the high mass of the sterile neutrino leads to a more pronounced effect at very short baselines.

1.5.2 Current status

An analysis by Mention et al. [51] in 2011 combines the reactor data with the gallium calibration experiments and the MiniBooNE results, concluding that the no-sterile-oscillation hypothesis is disfavoured at 99.8 % C.L.. The corresponding oscillation parameters are $|\Delta m_{41}^2| > 1.5 \text{ eV}^2$ (95%) and $\sin^2(2\theta_{ee}) = 0.14 \pm 0.08$ (95%). Figure 1.14 shows the ratio of observed to predicted reactor antineutrinos for several short baseline (SBL, distance between 10 m and 100 m) experiments. The neutrino-source - detector distance shown goes from zero to the scale of solar oscillations. A solid line shows the best fit to the data according to the 3+1 hypothesis. It is clear that this oscillation is most pronounced at very short baselines (VSBL) below 10 m. Hence new experiments at reactor sites will target these distances to resolve the reactor antineutrino anomaly, see section 1.6.

Due to the observation of the 5 MeV distortion, discussed in section 1.4.4, and the fact that flux deficits seem to depend on the type of fission isotopes, the reliability of flux calculations is questioned. Thus disfavours the sterile neutrino as explanation for the RAA. A recent paper by J. Kopp et al. addresses this issue by reviewing all available electron (anti)neutrino disappearance data [56]. They show that the sterile neutrino hypothesis can not be rejected with the current data set and that there is only a slight preference for the individual rescaling of neutrino fluxes. It is found that the 3+1 oscillation describes the global data with a significance close to 3σ relative to the no-oscillation case. A 2σ effect remains when the reactor fluxes and spectra are left free in the fit to the data. The allowed parameter region established in the analysis is consistent with a sterile neutrino anomaly solution to the gallium and reactor antineutrino anomalies. Figures 1.15 and 1.16 show the

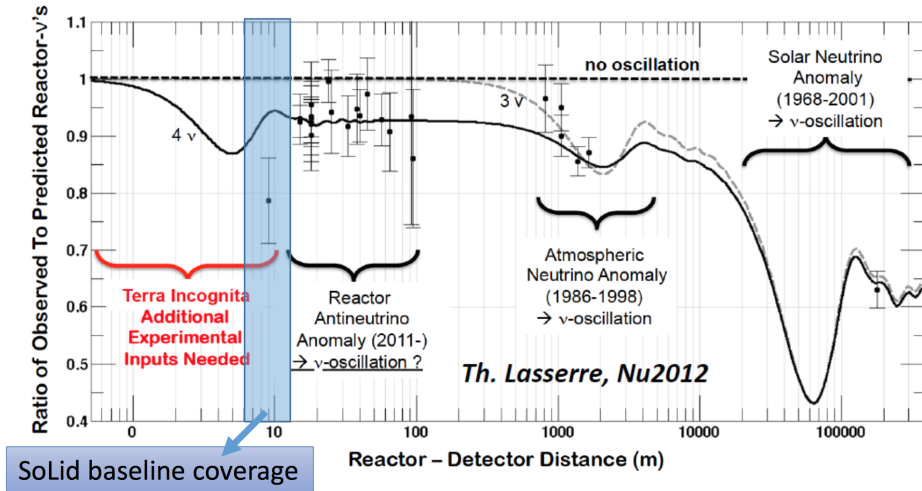


Figure 1.14: The reactor antineutrino anomaly. The striped line indicates the 3 oscillating neutrino solution, the solid line shows the 3+1 sterile neutrino hypothesis. Adapted from Th. Lasserre.

allowed parameter regions for the reactor data and a combination of reactor, gallium, solar and accelerator data, respectively.

1.6 Next-generation experiments

Section 1.5.2 shows that there is an urgent need for sensitive experiments that can either confirm or reject the sterile neutrino hypothesis. As shown in figure 1.14, experiments performed at very short baselines from reactors should be able to see whether the neutrino spectrum shows an oscillation or not. When placed at a highly enriched ^{235}U core, these experiments would also be capable to resolve the 5 MeV spectral distortion.

Currently several experiments are very close to, or are already, taking data. The SoLid collaboration is one of them, but as this thesis is performed within the SoLid experiment, the setup will be discussed in the following chapters. The main competitors of SoLid are STEREO and PROSPECT. Their detectors are placed at the research reactor of respectively the Laue-Langevin Institute (ILL) in Grenoble and at the Oak Ridge National Laboratory (ORNL) in Tennessee. These experiments need to fulfil several requirements to be able to detect the 5.7% deficit of electron-antineutrinos coming from the reactor. These can be split into reactor and detector specifications.

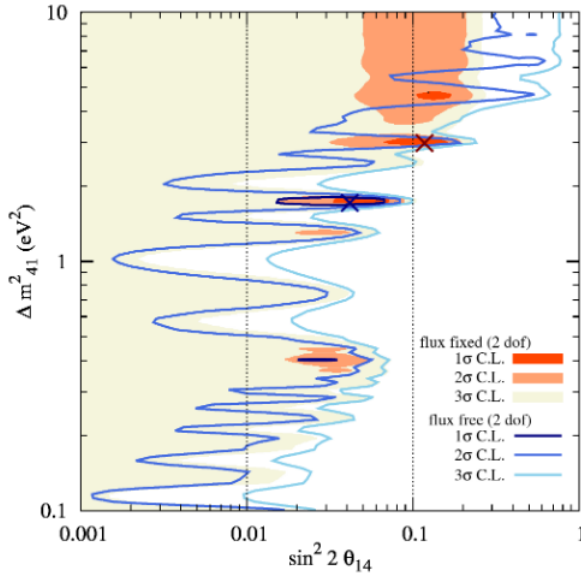


Figure 1.15: Allowed parameter regions for reactor neutrino experiments. The blue (red) cross indicates the best fit point for the flux-free (flux-fixed) analysis [56].

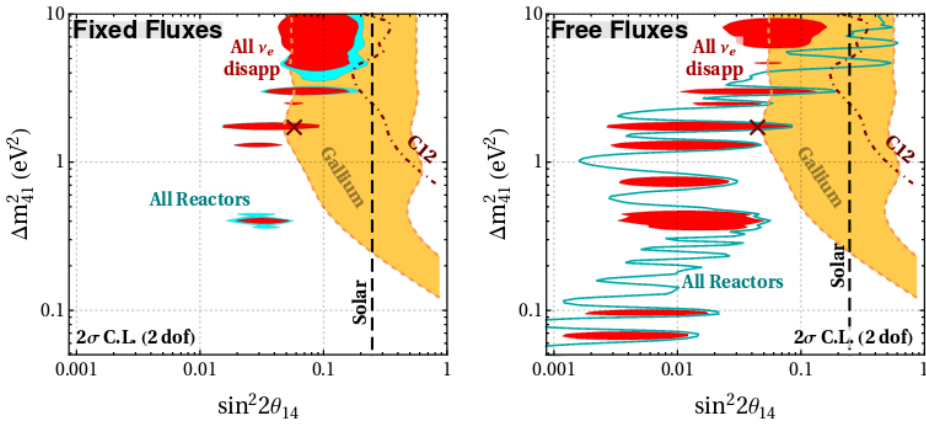


Figure 1.16: Allowed parameter region for fixed (left) and free (right) fluxes for all $\bar{\nu}_e$ disappearance experiments. Regions from reactor data, gallium experiments, solar data and ν_e scattering on ^{12}C are also shown [56].

- Reactor requirements
 - Compact core: a small reactor core reduces oscillation smearing and thereby reduces the uncertainty on the neutrino interaction distance measurement.
 - Baseline coverage: as shown in figure 1.14, a sterile neutrino would show itself as an oscillation over a certain distance. It is therefore important that a sufficient baseline is available. Moreover it is important that the detector can be placed very close to the core.
 - Safety regulations: these can imply that not all detection materials are allowed, such as flammable liquids. Access to the detector can also be restricted, which can introduce construction delays.
- Detector requirements
 - High spatial and energy resolution: as the RAA is only a few percent effect, the position and energy resolutions need to be sufficient to provide conclusive measurements. The position sensitivity is mostly correlated with the detector segmentation, while the energy resolution depends largely on the efficiency of the detection materials.
 - Effective background rejection: a detector above ground suffers from high cosmogenic backgrounds. Furthermore, the reactor will generate several backgrounds as well. It is therefore indispensable to have a powerful background rejection.

These challenges can be approached in several ways. The STEREO collaboration has chosen to use a liquid scintillation detector composed out of 6 target cells with a very good energy resolution and an acceptable position sensitivity [57]. There is both passive and active shielding, but background rejection can also be based on a signal shape analysis. A sketch of this detector is shown in figure 1.17. The PROSPECT detector [58] uses 11×14 cells of liquid scintillator for their antineutrino detector 1 (AD1) shown in figure 1.18, thereby increasing the position sensitivity compared to STEREO. Pulse-shape discrimination is the main way to reduce the backgrounds in PROSPECT as there is little shielding used. SoLid is the first experiment to employ solid scintillator material, thereby worsening the energy resolution slightly, but achieving very high position sensitivity. The SoLid detector design will be discussed in section 2.2.

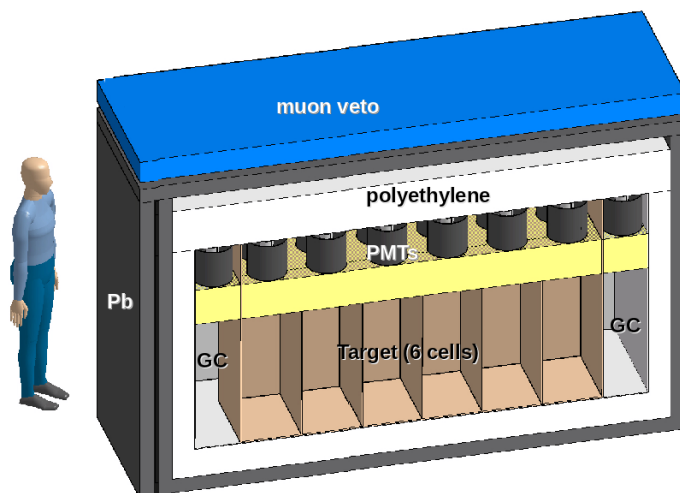


Figure 1.17: Set-up of the STEREO experiment [57].

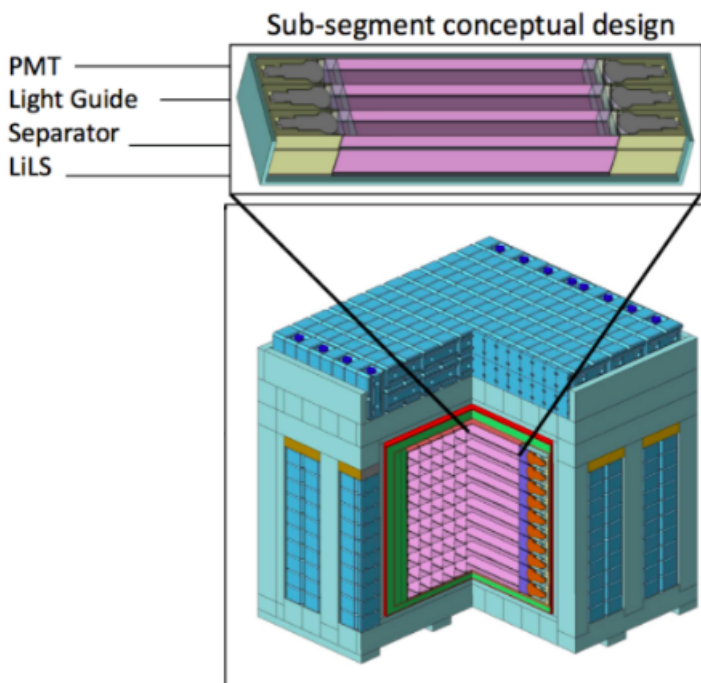


Figure 1.18: Set-up of the PROSPECT AD-1 [58].

A complementary approach to resolve the neutrino anomalies are source-based experiments. These experiments suffer less from flux uncertainties due to the purity of the sources. The downside are the regulations involved in making and transporting these peta becquerel sources. Furthermore, very few radiation facilities exist that are capable of providing these sources. A proposal for a source experiment was SOX, based at Laboratori Nazionali del Gran Sasso. Their aim was to place neutrino sources, ^{51}Cr and ^{144}Ce , at a short distance from the Borexino detector, shown in figure 1.19, and measure short baseline neutrino oscillations.

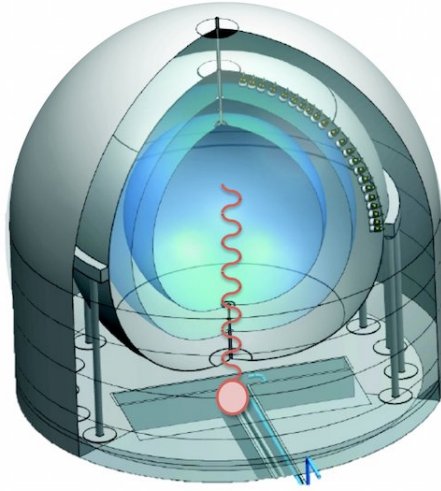


Figure 1.19: Set-up of the SOX source experiment at the Borexino detector [59].

Unfortunately the SOX experiment was suffering from many delays as regional activists feared radioactive contamination of the ground water, thereby postponing the approval of the regional government. Eventually, it was also deemed impossible to produce the required sources and the SOX experiment was stopped. However, given the implications that the sterile neutrino existence would entail, multiple experimental approaches need to be pursued to assure the physics community of the existence or non-existence of sterile neutrinos.

1.7 Conclusion

The discovery of neutrino oscillations requires neutrinos to have non-zero mass and thereby provides the first proof for physics beyond the Standard Model. To determine the oscillation parameters many experiments were carried out, using different neutrino sources: accelerators, the sun, reactors, radioactive sources and cosmic interactions in the atmosphere. A clear picture of 3 oscillating neutrinos was formed. However, several inconsistencies were found in the data. These were dubbed the accelerator, the gallium and the reactor anomalies. Recently another irregularity was observed: the 5 MeV bump in the prompt energy spectrum from reactor antineutrinos. The existence of a sterile neutrino would be able to explain many of these deviations, although many believe inaccuracies in the reactor flux predictions are at the root of the problem. It is clear that new experiments are needed to resolve these open problems in neutrino physics. One of them is the very short baseline experiment SoLid which aims to resolve the RAA and investigate the 5 MeV spectral distortion. The SoLid technology and analyses will be the subject of the following chapters.

It was shown in section 1.6 that very short baseline reactor experiments (\mathcal{O} (10 m)) can help solve several of the existing anomalies in the neutrino sector. One of these experiments is SoLid, short for "Search for oscillation with a ${}^6\text{Li}$ detector". The SoLid collaboration counts around 50 researchers from 13 institutes in Belgium, France, the United Kingdom and the United States of America. The experiment is hosted at the SCK•CEN in Mol, Belgium. This centre researches peaceful applications of radioactivity and has 2 working research reactors on site. The Belgian Reactor 2 (BR2) will act as a reactor antineutrino source for the SoLid detectors and its properties will be discussed in section 2.1. This chapter will also provide an in dept discussion of the SoLid technology and a short description of the prototype detectors NEMENIX and SM1 (SubModule 1) and the full-scale detector Phase 1.

2.1 Belgian Reactor 2

The Belgian Reactor 2 at the SCK•CEN is a research reactor specialised in material research and irradiation of silicon, thereby creating high-quality semiconductors. It is also one of the few reactors in the world producing isotopes for nuclear medicine. The reactor was commissioned in 1961 and has since then undergone several extensive overhauls. The last one took place from March 2015 until July 2016 and provided a limiting factor for the SM1 prototype data taking as will be discussed in section 3.5.

To be able to perform a sensitive neutrino oscillation measurement a reactor needs to fulfil several requirements, as mentioned in section 1.6. The BR2 reactor meets all the essential criteria and is therefore the perfect host location for the SoLid experiment.

- Compact core: because of the twisted matrix structure, the effective diameter of the reactor core is smaller than 1 m.
- Baseline coverage: the SoLid experiment can be placed on the level of the reactor core, thereby achieving a minimum baseline of 5.5 m between the reactor and the start of the detector. For a research reactor, the BR2 building is quite spacious, allowing a baseline up to 11 m.
- Safety regulations: due to a very high engagement between SoLid and the host institution SCK•CEN, access procedures to the reactor building are processed efficiently. Good communication concerning safety regulations and restricted materials keeps delays due to violations of the rules to a minimum.

In addition, SoLid is the only experiment operating in the BR2 building on the reactor core level, shown in figure 2.1. This implies that all other reactor ports (SoLid detectors are placed at port R1) are closed and shielded to keep background radiation stable and reduce it to a minimum. Nonetheless, every experiment close to a reactor will suffer from high neutron and gamma backgrounds and these will have to be discriminated from the antineutrino signal. Aside from these reactor induced backgrounds, the fact that the experiment is located above ground implies important cosmogenic backgrounds of which the impact will be discussed in chapter 4.

Because the reactor antineutrino anomaly is such a small effect, it is necessary to collect sufficient data. With an average reactor-on period of 150 days per year for the BR2 reactor, the aim is to have a sensitive oscillation measurement after a data taking period of 3 years. During this time, the BR2 reactor will run at a thermal power between 40 and 80 MW. As will be shown in section 2.2.1, the power setting has an influence on the number of antineutrino interactions in the detector. However, since precise data on the power of the reactor are available to the SoLid collaboration, this is not an issue and will in fact provide an extra parameter to investigate the RAA.

An added benefit of the BR2 reactor is its highly enriched ^{235}U (93%) core (HEU core). A precise measurement of its antineutrino spectrum will provide valuable insights on underlying nuclear processes and might also indicate an explanation for the 5 MeV spectral distortion discussed in section 1.4.4.

All these properties make the BR2 reactor an excellent setting for the SoLid experiment, but to overcome the high environmental backgrounds a novel detection technology is required as well. This technology will be explained in detail in the following section 2.2. Table 2.1 gives an overview of the important BR2 parameters.

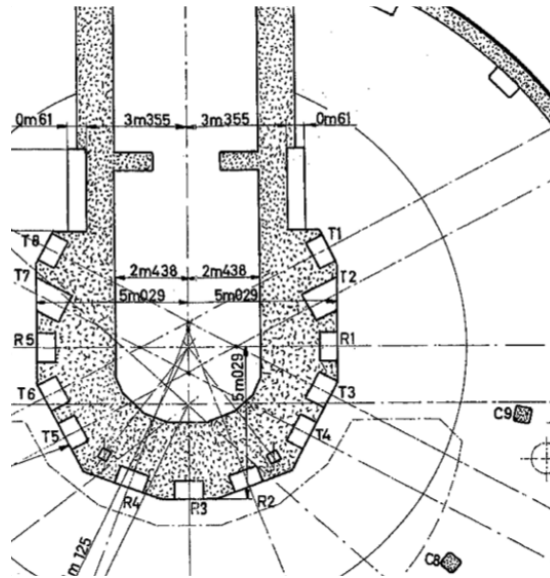


Figure 2.1: Layout of the BR2 building at the SoLid level (from internal communication with A. Vacheret).

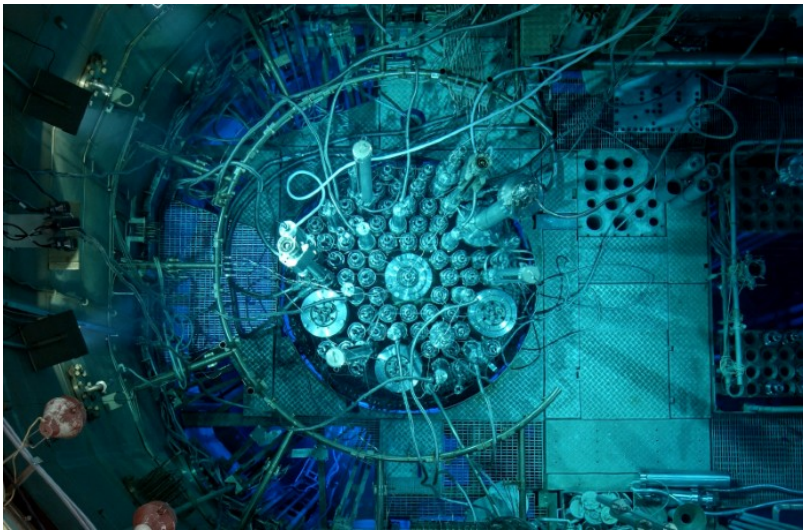


Figure 2.2: The BR2 twisted matrix core from above [60].

Table 2.1: Summary of the BR2 properties.

Reactor power	40 - 80 MW
Core diameter	2 m
Effective core diameter	< 1 m
Mean reactor-on period / year	150 days
Enrichment in ^{235}U	93%

2.2 SoLid technology

2.2.1 Antineutrino interaction

The aim of SoLid is to measure the antineutrino spectrum from the BR2 reactor via the inverse beta decay, see equation 1.3. Here, the antineutrino interacts with a proton of the detector, generating a positron and a neutron. Since the neutron is more massive than the proton, there is a threshold antineutrino energy of 1.805 MeV for the IBD reaction. According to T. Mueller et al. [61] the spectrum of detected antineutrinos spans from 1.805 MeV up until 10 MeV with a peak around 3.5 MeV. This behaviour is due to a falling energy spectrum of emitted antineutrinos from the reactor, compensated by a rise in cross section for the IBD interaction above the threshold energy.

The number of antineutrino interactions N_i from a HEU core for an exposure time T , with a detector at a distance L from the core and for an antineutrino energy range $[E_i, E_{i+1}]$ is given by the following expression:

$$N_i = T \frac{N_p}{4\pi L^2} \frac{P_{th}}{E_{fission}^{235\text{U}}} \int_{E_i}^{E_{i+1}} \sigma(E_{\bar{\nu}_e}) S_{235\text{U}}(E_{\bar{\nu}_e}) R_i(E_{\bar{\nu}_e}) P_{ee}(E_{\bar{\nu}_e}, L, \Delta m_s^2, \theta_s) dE_{\bar{\nu}_e} \quad (2.1)$$

With the probability P_{ee} that the $\bar{\nu}_e$ does not oscillate into a sterile neutrino state:

$$P_{ee}(E_{\bar{\nu}_e}, L, \Delta m_s^2, \theta_s) = 1 - \sin^2(2\theta_s) \sin^2\left(1.27 \frac{\Delta m_s^2 [eV^2] L [m]}{E_{\bar{\nu}_e} [MeV]}\right) \quad (2.2)$$

with N_p the number of protons in the detector, P_{th} the reactor thermal power and $E_{fission}$ the energy released per fission. The IBD cross section is represented by $\sigma(E)$, the reference antineutrino spectrum by $S(E)$ and the detector response by R_i . In the no-oscillation case the probability P_{ee} is assumed to be equal to 1.

Formula 2.2 assumes that the reactor core emitting neutrinos is a point source, this can be tolerated since the BR2 reactor core is relatively small. Another assumption being made is that there is no oscillation of the $\bar{\nu}_e$ into $\bar{\nu}_\tau$ or $\bar{\nu}_\mu$. As shown in figure 1.14, these oscillations are not yet present at the baseline available at the BR2 reactor and the approximation is therefore valid.

Comparing interaction rates at different positions in the detector along the baseline allows for a model independent measurement and cancels out the uncertainties in the reactor antineutrino flux.

As seen in formula 2.1 the number of target protons and the uncertainty on this number plays a big role in the amount of antineutrino interactions. It was therefore highly important to find a method to control this variable, which will be discussed in section 3.3. The reactor site and type of reactor core also control many parameters in the expected number of antineutrinos, such as P_{th} , $E_{fission}^{235U}$, $S(E)$ and the baseline between the reactor core and the detector L . SoLid has a dedicated working group to calculate the expected antineutrino emission spectrum from the BR2 reactor with dedicated MCNP¹ codes. An example of these calculations can be found in [62].

A sterile neutrino search is performed by comparing the expected antineutrino spectrum with a measured spectrum. This measured spectrum needs to be highly accurate, since the reactor antineutrino anomaly is only a 5.7% effect, see section 1.4.3. To tackle this challenge, SoLid adopts a highly segmented composite solid scintillator technique, which was in depth explained in [63] and will be summarised in the next section 2.2.2.

2.2.2 Composite scintillator cubes

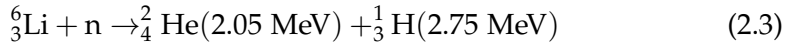
The SoLid collaboration has developed a novel technology to be able to detect both positron and neutron created in the IBD interaction. In contrast to most experiments, SoLid does not use liquid scintillators doped with Gallium, but a solid scintillator detector.

The primary components of a SoLid detector are $5 \times 5 \times 5 \text{ cm}^3$ polyvinyl toluene (PVT) cubes, which are placed in one or more 2D grids called “planes” or “frames”. The cubes are cut from ELJEN Technology’s EJ-200 [64] slabs of scintillating material and grooves are machined to accommodate the readout fibres. The cubes absorb the kinetic energy deposited by the positron created in the IBD and promptly emit scintillation light. Due to the fast nature of this signal, the positron is often referred to as the “prompt” signal. After the

¹Monte Carlo N-particle transport codes are software packages dedicated to the simulation of nuclear processes.

positron has lost its kinetic energy in the cube, it will annihilate with an electron, thereby generating 2 annihilation γ 's with an energy of 511 keV each. These gammas will also produce scintillation light in the cubes.

${}^6\text{LiF:ZnS(Ag)}$ screens are attached to the cubes, as ${}^6\text{Li}$ has a high capture cross section for neutrons. Before a neutron can be captured, it needs to lose energy, a process called thermalisation. This means that the original energy of the neutron gets lost completely. Because of the time the thermalisation takes, the neutron is often dubbed the "delayed" signal. During the interaction of the neutron with the ${}^6\text{Li}$ screens a tritium and an alpha particle are created:



The created particles collide with the ZnS in the screens, thereby exciting several energy levels. The de-excitation of these levels gives rise to scintillation light. As the energy levels of ZnS have slow decay constants, the neutron signal has a longer tail in comparison to the positron. The ZnS screens and the cubes are optically coupled with a very small air gap. Figure 2.3 shows the observed signals, also called waveforms, from an IBD positron and neutron in the detector. The clear distinction in regard to amplitude and duration of the signals makes it easier to separate neutrons from EM signals, while the time between the 2 signals, caused by the thermalisation of the neutron, can be used as a parameter to distinguish IBD events from background events.

All cubes are individually wrapped in DuPont Tyvek paper to optically isolate them from each other, so that the energy loss of a particle inside the cube will only create light in that particular cube and light leakage is reduced to a minimum. The light is then transported to the readout system by use of wavelength shifting (WLS) fibres. These fibres are placed in the grooves machined in the PVT cubes in both the horizontal and vertical direction. This 2D readout grid ensures that a signal can be traced back to its cube of origin. SoLid is therefore able to achieve a position precision of 5 cm in each direction. Figure 2.4 shows a SoLid composite detection unit: the PVT cube with grooves for the WLS fibres, the ${}^6\text{LiF:ZnS(Ag)}$ screen and the Tyvek wrapping.

2.3 Detectors

Several detectors have been built by the SoLid collaboration, using the technique explained in the previous section 2.2.2. The first prototype detector, called NEMENIX, served as a proof of principle for the SoLid detection technique. It showed the feasibility of neutron discrimination based on the pulse shape and was able to make a prompt-delayed signal selection. NEMENIX

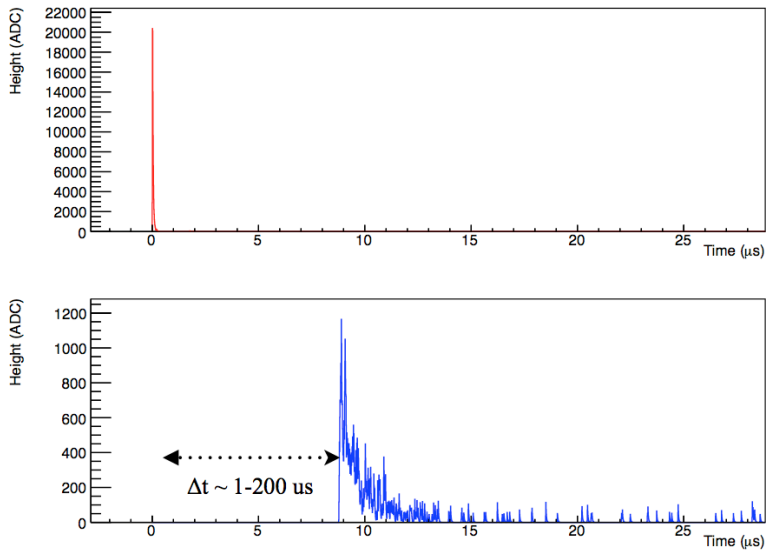


Figure 2.3: Signal due to the positron (top) and neutron (bottom) capture [65].

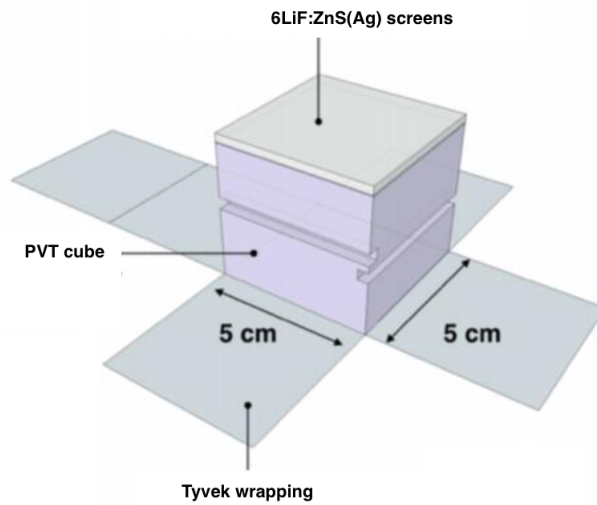


Figure 2.4: SoLid composite scintillator detection unit.

also made a first background measurement at the SoLid location in the BR2 building, giving an indication of the expected rates for future detectors. The NEMENIX prototype was constructed with 64 cubes in a $4 \times 4 \times 4$ grid, see figure 2.5 for a partly assembled prototype. Each cube was equipped with 1 ^6Li screen of $225 \mu\text{m}$ thickness and wrapped in 75 gr/m^2 Tyvek paper. Every cube was read out with 1 horizontal and 1 vertical fibre, thus totalling 32 read out channels for the whole detector. The detector was shielded with around 20 cm of High Density Polyethylene (HDPE) and was equipped with 4 external muon detectors, of which 2 are visible in figure 2.6. The NEMENIX prototype took data at a distance of 5.5 m from the BR2 reactor core, in front of port R1, from August 2013 until spring 2014.

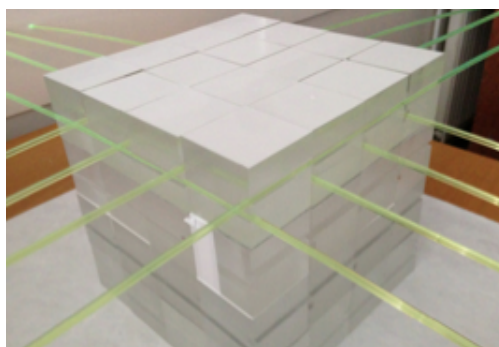


Figure 2.5: Partly assembled NEMENIX prototype detector.

To demonstrate the large-scale use of the SoLid technology the SM1 (Sub-Module 1) prototype was built. This 288 kg module was constructed in the summer of 2014 and had a data-taking period from February 2015 until August 2015. Building this prototype taught where the construction procedures could be improved and the analysis results also indicated that some changes needed to be made on the detector design. All these changes were eventually incorporated in the Phase 1 detector, the full SoLid detector. The construction and parts of the analysis of both the SM1 and Phase 1 detector are the subject of this thesis and will therefore be discussed in the following chapters.



Figure 2.6: NEMENIX inside HDPE shielding placed in front of the BR2 reactor. 2 muon detectors wrapped in black plastic are visible below and on top of the shielding.

2.4 Conclusion

Equation 2.1 shows that the number of detected antineutrinos coming from a reactor core depends on many parameters. Several are dependent on the reactor and it is therefore very important to perform an oscillation search at a suitable site. The BR2 reactor ticks all the required boxes and was therefore chosen as the location for the SoLid experiment. Nonetheless, a detector in a reactor environment will always suffer from high backgrounds. To provide a way to handle these backgrounds, a novel technology was developed: a composite solid scintillation detector. This technology was discussed in section 2.2.2, while section 2.3 considers the different detectors built with the SoLid design. Chapters 3 and 5 will provide a more in-dept discussion on the SM1 prototype and the full Phase-1 detector.

The SM1 prototype

3

Chapter 2 explained the novel SoLid technology and the several detectors built within the collaboration. It was mentioned that the SubModule 1 (SM1) detector was built as a prototype with as goal to test the feasibility of the composite scintillator technology on a large scale. This chapter will provide more detailed information on the SM1 prototype.

Formula 2.1 showed the key factors in determining the expected antineutrino spectrum. This indicates that it is extremely important to know the proton content of the detector to a very high precision. This implies that construction protocols have to be developed to gather this information. These protocols are also necessary to make sure contamination of the scintillating materials is kept to a minimum, as even small amounts of dirt or grease on these surfaces might diminish the light yield. Furthermore, rigorous protocols ensure a detailed database with information on different detector parts. The latter is necessary to explain or solve issues found in the detector commissioning, as well as in the later stages of data taking.

The construction of the large-scale prototype SM1 has been a large part of the work for this thesis. The construction and subsequent commissioning period took place at the labs of Ghent University.

During the construction of the SM1 detector, over the summer of 2014, I was responsible for the training and supervision of 2 students to “wrap” cubes. After the wrapping of the cubes I constructed almost all 9 frames myself and also equipped them with electronics. During the commissioning of the prototype, from September until November 2014, I took shifts to monitor the data taking. The construction and corresponding protocols of SM1 will be explained in detail in section 3.2.

3.1 SM1 properties

As SM1's main purpose was to test the SoLid technology on a large scale, the detector was designed to be around $1/5^{th}$ of the full-scale detector and to use the same materials. In total, SM1 has 2304 PVT cubes, of $5 \times 5 \times 5$ cm³, divided in a 9 times 16×16 array. These arrays are called "frames" or "planes". Figure 3.1 shows a sketch of the SM1 detector, an exploded view of a frame, the fibre connection and an unfolded cube. This section will discuss all those detector parts.

The cubes used for SM1 have similar properties as the NEMENIX cubes: wrapped in 75 g/m² Tyvek paper and equipped with a single 225 μ m thick ⁶LiF:ZnS(Ag) neutron-sensitive screen. The Li screen is added on a side with no fibre grooves which would in the final array be perpendicular to the reactor-detector baseline, the z-direction shown in figure 3.1, and facing the reactor. Each cube has 2 perpendicular grooves to allow passage of the BCF-91A WLS fibres from St. Gobain [66]. These fibres consist of a single cladded core. With a cross-section of 3×3 mm², the fibres fit easily inside of the 5×5 mm² grooves. Figure 3.2 shows an SM1 cube in an open Tyvek wrapping and a closed cube with fibres passing through.

The frames holding the cubes are constructed of 4 hollow 2017a¹ aluminium bars which contain the electronic cables. Every 5 cm a hole is drilled in each of the bars, so that the wavelength shifting fibres inserted into the grooves of the cubes can exit. The holes are just large enough so that connectors that hold the multi-pixel photon counter (MPPC) from Hamamatsu, type S12572-050P [68], fit snugly inside. Each MPPC is a 3×3 mm² array of 3600 pixels. Each pixel is an avalanche photo diode, and all pixels are connected in parallel. The signal of a discharge of a single pixel is called a pixel avalanche (PA) and is a measure of intensity of the incoming light pulse. The MPPC is optically coupled to the WLS fibre by optical grease, type BC630 from Saint-Gobain. An aluminium mirror tape is applied at the other end of the fibre so that light transported in this direction can be reflected back towards the MPPC. To obtain a more uniform light yield, the MPPC and mirror positions alternate along the sides of the frame, as shown in figure 3.3.

The sides of the aluminium frame are closed with cover plates out of the same material. The plates have 1 hole through which the cabling is fed. The hole is made light-tight with the use of rubber band and black tape. On the inside of the covers some foam is attached to provide extra support for the

¹2017a aluminium is an alloy with as main additive copper. 2017a is the Aluminium Association designation for this material [67].

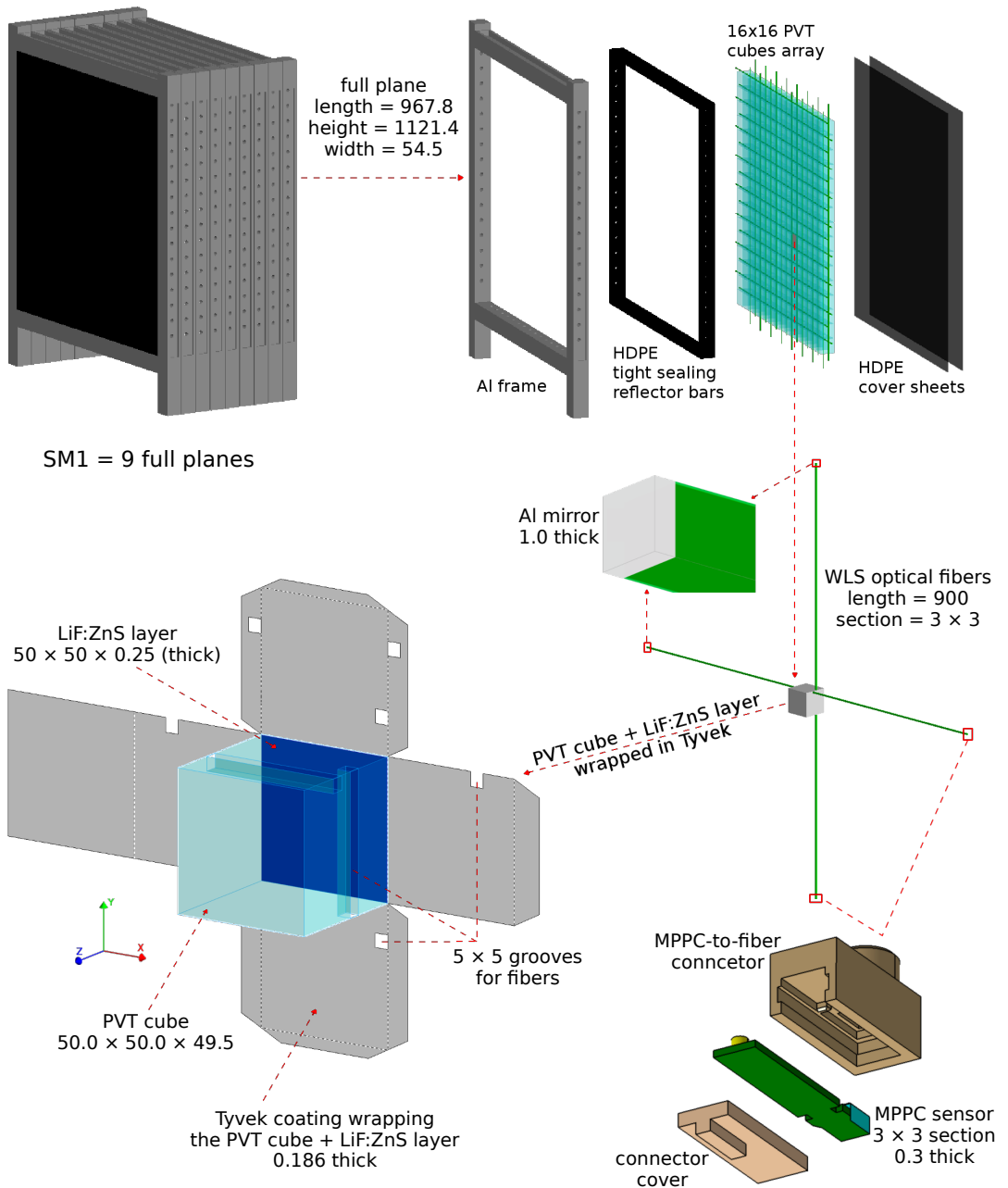


Figure 3.1: Diagram of the prototype detector, exploded frame, fibre readout and cube assembly. All sizes in mm. (Thanks to I. Pinera-Hernandez)

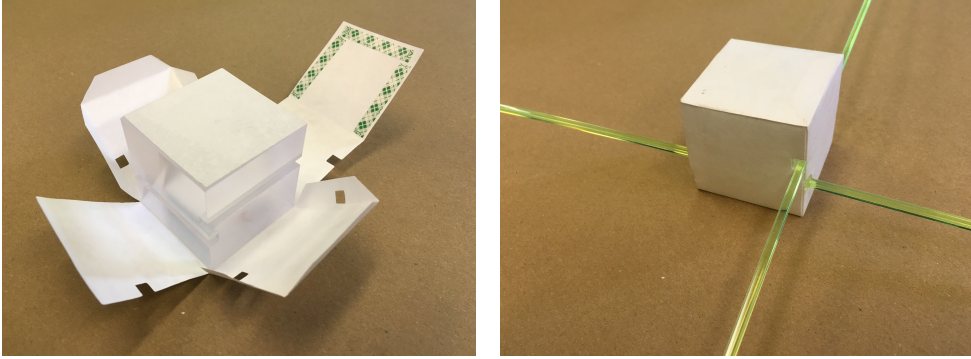


Figure 3.2: A SM1 cube in an open Tyvek wrapper with ^6Li screen on top (left) and a wrapped SM1 cube with 2 perpendicular fibres (right).

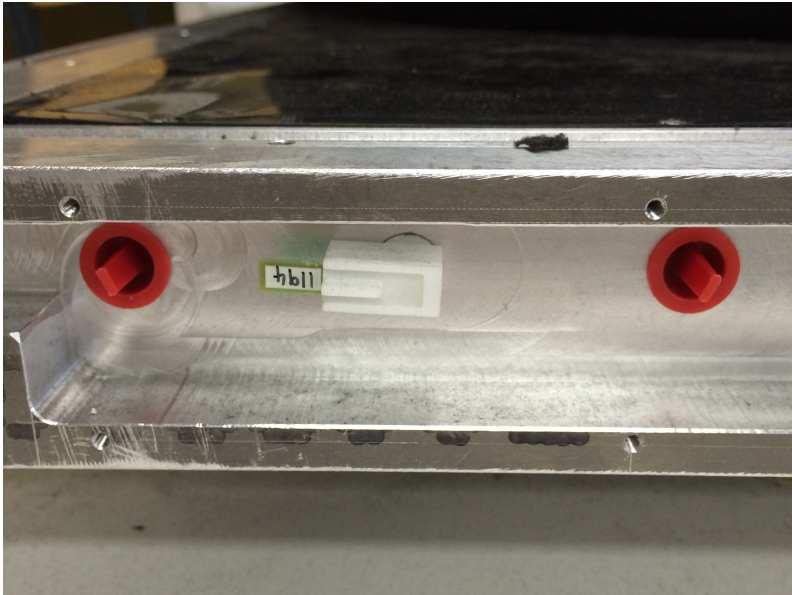


Figure 3.3: Picture of the side of an SM1 frame. 2 red closing caps are visible where mirror connectors are installed and in between, an MPPC connector with installed MPPC can be seen. Note that the MPPC is not yet cabled.

connectors holding the photon counters.

Between the array of cubes and the Al frame, 2 cm thick high density polyethylene (HDPE500) bars are placed. These bars provide moderation material for neutrons and are also used as reflection for neutrons created in the edge cubes of the detector. 2.2 mm thick HDPE cover sheets on the back

and front of the Al frames are added to provide extra support for the cubes before the separate frames are put together in 1 module.

A module is formed by connecting 9 planes together in an aluminium support frame. A 9 cm HDPE shielding surrounds the module. This shielding consists out of 3 layers of 3 cm connected to each other. To make sure that the middle of the detector aligns with the centre line of the reactor, the module is positioned on top of a steel plate that can be adjusted in height. Figure 3.4 shows the transport of the SM1 detector with part of the shielding and the steel plate attached.



Figure 3.4: The SM1 prototype with the bottom and back side of the shielding and the steel plate attached.

The electronics used for the SM1 prototype were custom developed at Oxford University. Their discussion is beyond the scope of this thesis. More information can be found in the detailed paper on SM1 construction and results [69].

3.2 Construction and protocols

The scintillating cubes used for SM1 were machined from large PVT slabs at the University of Antwerp, where each cube was also provided with 1 “hori-

zontal" and 1 "vertical" groove. After the processing, the cubes were sent to Ghent University. Here they were individually washed with detergent and rinsed with water to remove grease or dirt residues. After the washing procedure they were left to dry to the air. Starting from the washing procedures, the cubes were only touched with vinyl, powderless gloves. The cubes were stored in such a way that cubes from the same PVT slab were traceable.

The Tyvek wrappers were folded and double-sided tape was applied to the inside of the closing flap.

The ${}^6\text{LiF:ZnS(Ag)}$ screens were cut by hand from large sheets by the technical staff at Ghent University and were always handled with gloves.

The assembly procedure of a cube started by weighing a bare cube with a scalar with tolerance 0.01 g. Then the Li screen was weighed and its thickness was measured with a precision of 1 μm . The cube and neutron screen were then wrapped in a Tyvek wrapper. At that moment a sticker was also applied to the outside of the Tyvek wrapping. This sticker contained a code which referred to the PVT slab of the cube, and the frame and location where the cube would be placed inside the detector. At this point, the wrapped cube was weighed again and all the measurements were stored in the database along with the corresponding sticker code. The wrapped cubes were then stored in batches of 256, 1 batch for each frame.

According to a numbering scheme, all cubes were ranked in the Al frame on the basis of their sticker code. This allowed for a very detailed overview of mass and Li-content distribution across the whole detector.

The frames were built row by row while keeping an eye on the alignment of the cube grooves and the holes in the Al bars. To compensate for small differences in cube sizes, which could cause misalignment, the HDPE bars on the sides could be adjusted up to 3 mm. Once a frame was filled with cubes, the fibres were inserted. Due to the non-symmetrical nature of the grooves in the cube, this provided a good test to check the orientation of the cubes inside the frame. Once all fibres were inserted, the frame was closed with the HDPE plate and the electronic sensors and cables were installed. Figure 3.5 shows the process of filling a plane with cubes.

3.3 Proton content

To achieve a detailed knowledge of the detector proton content, one needs to know the weight of the H-rich materials and their hydrogen content. The latter is usually provided by the manufacturers.

Section 3.2 showed how the mass of every SM1 cube was determined to a high precision, down to the per-mille level. Because these cubes are the bulk



Figure 3.5: SM1 frame partly filled with 4 fibres inserted with black HDPE backing visible (left), filled SM1 frame with black HDPE side bars clearly visible (right).

of the detector material, they represent also the largest H content.

Tyvek is $> 98\%$ polyethylene (C_nH_{2n}) and will therefore have a non-negligible part in the total detector proton content. The wrappers were not weighed individually, but in stacks of 100. This was done because the scale reaches its best accuracy for weights around 200 g.

The HDPE bars on the sides between the Al frame and the cubes, and the HDPE sheets that close the frames on both sides, also need to be taken into account. These parts were not weighed individually during construction, but a sample batch was measured and used to determine an average weight.

Combining all these results leads to the component proton contents shown in table 3.1, which gives a total H content of $18.54 \cdot 10^{27}$ H with an error of $0.03 \cdot 10^{27}$ H and a relative error of 0.16 % for the full SM1 detector. The values and errors shown in this table were calculated by M. Labare [70].

Table 3.1: Masses and hydrogen content of detector components.

Component	Mass (g)	H content ($\times 10^{27}$)
PVT cubes	286561.8 ± 0.50	14.4822 ± 0.0280
Tyvek wrappers	3154.2 ± 2.40	0.2712 ± 0.0055
HDPE500	44055.0 ± 73.5	3.787 ± 0.0070
Total	333771.0 ± 73.5	18.5404 ± 0.0293

3.4 Frame commissioning

After the construction of the SM1 frames, each plane underwent individual commissioning. The goal of these tests was to ensure that all optical and electronic connections were correct and to get a first indication of the light attenuation along the WLS fibres.

The commissioning was performed with the use of a ^{60}Co source with an activity of 167 kBq and with cosmic muons. Figure 3.6 shows a frame during the commissioning process. The frame was placed horizontally on a table and with the help of a paper overlay the radioactive source was positioned on specific cubes along the edge of the detector. At every position of the source, random triggered data was collected. So, if the trigger map would show a hot spot on a location different than the source position, this would indicate a fault in the electronic cabling. In a similar way it would be possible to discover a broken fibre or a bad MPPC-to-fibre connection in case the hot spot would be at the correct position but less clearly pronounced than expected.

With the random trigger source data an analysis was performed to determine the attenuation along the fibre. This was explained in an internal note [71] and the details are outside the scope of this thesis. It is, however, interesting to mention that the study showed a reduced light yield in the channels at the sides of a frame. It shows that the black HDPE bars reflect less light than is the case for cubes surrounded by other cubes wrapped in white Tyvek. A feature that needed to be improved for the Phase 1 detector.

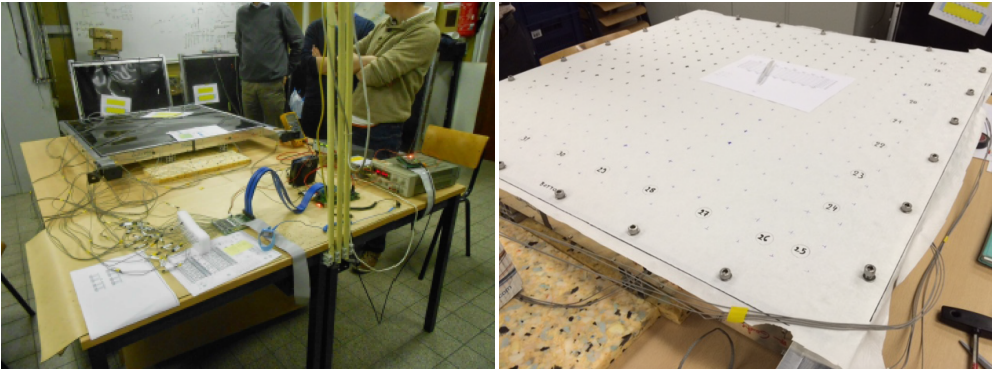


Figure 3.6: Pictures illustrating the SM1 plane commissioning set-up.

Some frames were also commissioned by performing overnight runs without radioactive source, but with cosmic muons. The hit maps obtained with these runs were uniform, as expected, and would otherwise have been an

indication of a bad connection or incomplete readout chain.

After the commissioning, the frames were inserted in the aluminium support frame to form the complete SM1 detector.

3.5 Data taking and analyses

After the construction and plane commissioning at Ghent University, the SM1 detector was moved to SCK•CEN on the 27th of November 2014. Figure 3.7 shows the detector installed in the BR2 building in front of reactor port R1.

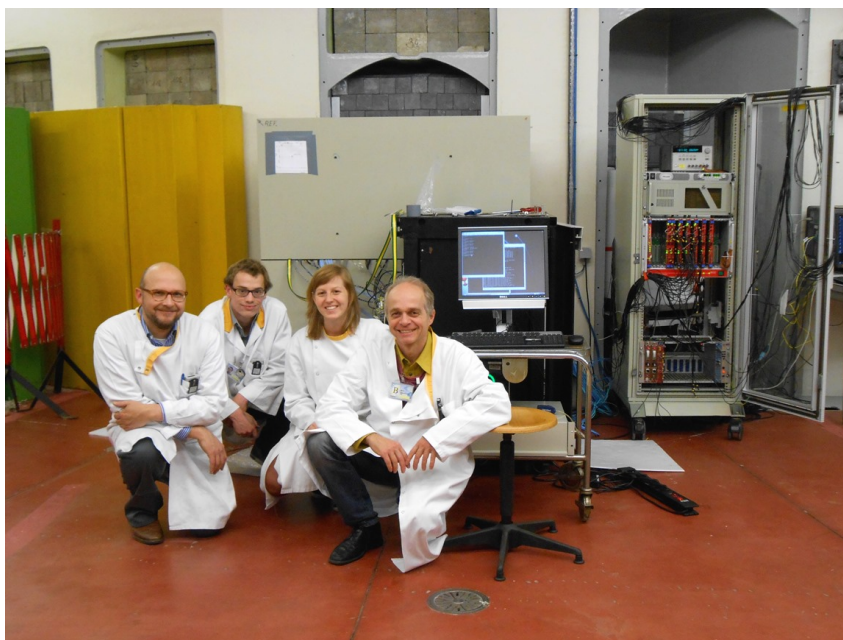


Figure 3.7: The SM1 prototype within its shielding installed in front of the R1 port of the BR2 reactor.

Due to the planned overhaul of the reactor, foreseen to start at the end of February 2015, there was a lot of pressure to start data taking as soon as possible. In fact, it already had impact on some of the decisions in ordering detector materials and on the electronics development. For example, single-cladded WLS fibres were ordered since the double-cladded fibres were not in stock. Similarly, there was not enough time to have a full electronics commissioning and the detector was thus equipped with a sub-optimal readout.

The full detector commissioning at the BR2 reactor finished just in time before the reactor shutdown and it was possible to take 3 days of reactor-on

data. This was followed by collecting reactor-off data until mid-April 2015. At the end of April several runs were taken with radioactive sources to perform detector calibrations. The sources used were ^{60}Co , a gamma source, and $^{241}\text{Am}^9\text{Be}$, a neutron source. Two data sets were collected with the second source, both with the source at a different positions with respect to the detector and with part of the detector shielding removed, shown in figure 3.8. Table 3.2 shows a summary of all data collected with the SM1 detector.

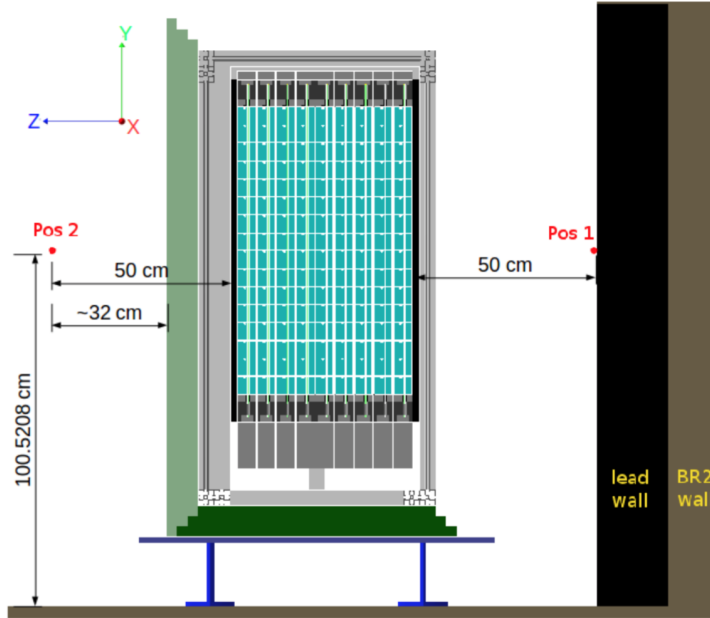


Figure 3.8: Sketch of the two positions of the $^{241}\text{Am}^9\text{Be}$ source. Thanks to I. Pinera.

Several analyses were performed by the SoLid collaboration on the SM1 data. The most important ones are described in the dedicated SM1 paper [69] and are shortly summarised here.

Starting from a low-level analysis, it was clear that the recorded signals suffered from issues with the electronics. Periodic noise, digital irregularities and an undershoot in the amplitude of signals were found in the readout data. Although most of these problems could be mitigated at least partly, these issues resulted in a lower neutron detection efficiency and showed the need for electronics upgrades in the Phase 1 detector and are described in section 5.1. Figure 3.9 shows examples of the periodic noise and digital spikes before and after offline correction. The periodic noise issue was mitigated

Table 3.2: Summary of data taken with SM1.

Dataset type	Dates	Live time (hrs)
Reactor-on	00:00 21 Feb - 08:00 24 Feb	50.9
Reactor-off	08:00 24 Feb - 00:00 12 Mar and 00:00 27 Mar - 12:00 11 Apr	577.8
Co calibration	14:00 22 Apr - 14:00 24 Apr	48.0
AmBe calibration Pos. 1	15:42 28 Apr - 24:00 30 Apr	65.0
AmBe calibration Pos. 2	17:00 4 May - 18:00 4 May	1.0

with the application of a fast Fourier transform (FFT).

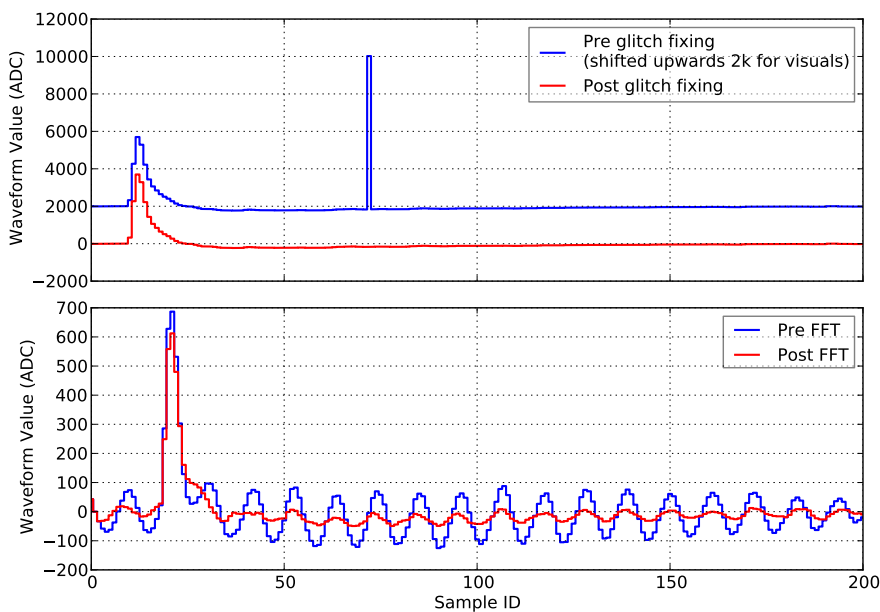


Figure 3.9: Examples of the digital irregularities (above) and periodic noise (below) found in the data. Before correction in blue and after correction in red. Thanks to D. Saunders.

The neutron detection efficiency was also reduced by the low light-yield in SM1. Using 2 different approaches, the light yield was found to be 12 PA/MeV per fibre. Several upgrades are therefore included in the Phase 1 design to improve the light yield.

After the low-level waveform analysis, the basic particle objects, such as neutrons, muons, and lower energy electromagnetic (EM) signals were reconstructed. Figure 3.10 shows an identified EM and neutron signal. The reconstructed muon tracks could be used for energy calibration, but also to validate the SoLid simulation package and the timing and stability of the detector. The latter items will be discussed in chapter 4.

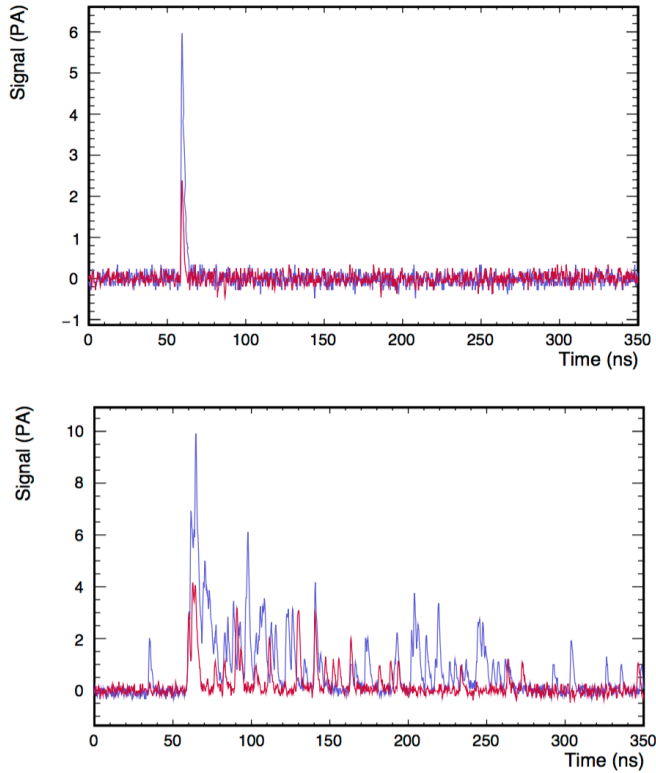


Figure 3.10: A charged particle signal (top) and a neutron signal waveform (bottom). The blue and red curves represent the waveforms detected by MPPC's connected to the two perpendicular optical fibres crossing a cube [63].

The neutron and EM objects were used in the search for antineutrinos. Unfortunately, the combination of the limited reactor-on time and a low neutron detection efficiency made it impossible to detect antineutrinos with the SM1 detector. Nonetheless, the data proved to be very useful in the study of backgrounds and showed that experimental uncertainties on the antineutrino signal were dominated by fast neutron induced backgrounds.² This result in-

²Fast neutrons are created by high-energy muons in the process of nuclear spallation in the

licated that the full Phase 1 detector needed more shielding to reduce these backgrounds.

3.6 Conclusion

The SM1 prototype detector was built to prove the feasibility of the SoLid technology on a large scale. With its 2304 cubes and the need for a precise proton count, several construction procedures were developed in the scope of this thesis. These were discussed in section 3.2. With the rigorous application of these procedures it was possible to determine the proton content of the detector down to per-mille level.

The construction took place in summer 2014 until October 2014, during which time I was full-time occupied with the supervision of 2 job students and the construction of SM1 detector frames. During the frame commissioning in November, described in section 3.4, I took shifts and performed a first study of the light-yield [71].

At the end of November the prototype was moved to the BR2 reactor. After an intensive commissioning of the complete detector, a limited data set was collected during the reactor-on period. After the BR2 shutdown for maintenance, several months of reactor-off data and a few calibration runs with radioactive sources were taken.

Due to the limited reactor-on data and a sub-optimal electronics system, it was impossible to observe neutrinos in the data set. However, it was shown that neutrons can be distinguished from other particles based on their pulse shape, see figure 3.10. Several studies indicate that the high spatial resolution of the detector provides, as expected, a very efficient way to reduce backgrounds [72]. The SM1 results were published in a dedicated paper [69].

A detailed study of the cosmic backgrounds in SM1 was performed during this thesis and will be discussed further in chapter 4. It will be shown that these results lead to a good understanding of the detector, trust in the stability and timing of SM1 and a verification of the cosmic simulation package.

In general, the results from the SM1 prototype lead to several design changes for the Phase 1 detector. These changes will be specified in section 5.1. Most of the upgrades are meant to increase the light-yield or enhance the electronics performance with as goal to improve the IBD detection efficiency.

material surrounding the detector.

Simulation of cosmic ray induced backgrounds 4

So-called primary cosmic rays, mostly protons, are generated mainly outside our solar system. Upon entering the earth's atmosphere these primary rays interact with molecules and atoms, thereby generating secondary cosmic rays. Many different particles can be created in this way, such as neutrons, electrons, pions, kaons and muons. The last category of particles do not interact strongly with matter and can thus easily reach the ground and even penetrate it up to a certain depth depending on their energy. Because of the high rate of cosmic muons, most neutrino experiments take place below ground, in deep mines or under mountains, to minimise the related backgrounds. Unfortunately, SoLid is located at the BR2 reactor site at a height of 10 m above ground level and with very little overburden (30 meters of water equivalent caused by the concrete roof).

SoLid will thus suffer from high cosmic backgrounds, coming from both muon and neutron secondary cosmic rays, as well as the fast neutrons that are generated by interactions of the cosmic muons in the material surrounding the detector. Due to the sensitive nature of the measurement that SoLid attempts to make, it is extremely important to understand all the different backgrounds and to be able to distinguish them from the IBD signal.

Luckily, muons are not only a nuisance, their interaction in the SoLid detector also provides a useful tool to study the stability and timing of the detector, as will be shown in section 4.3.

To understand all cosmic backgrounds, a dedicated simulation package "CosmicGen" was developed in the scope of this thesis. The goal of this package is to generate cosmic input files for the SoLid Geant4 [73] simulation package, which will be discussed shortly in section 4.1.3. This chapter will provide detailed information on CosmicGen and its validation with SM1 data (see section 4.2).

4.1 CosmicGen

CosmicGen is a software package developed to create output files that contain all the information on secondary muon or neutron particles from cosmic rays. These files can then be used as an input to the SoLid Geant4 code, which then propagates the particles through the BR2 building and the detector.

CosmicGen generates neutrons and muons according to generators found in literature. As most cosmic particle generators have limitations in energy range, location on earth, ... it was opted to investigate several generators for both muons and neutrons to be able to compare the results. For the muons there are 3 different generators available within CosmicGen: CRY [74], Reyna [75] and Guang [76], while there are 2 for the neutrons, CRY and Gordon [77].

CRY is a software library that generates cosmic shower distributions at 3 different altitudes (sea level, 2100 m, 11300 m) and over a wide energy range. The particles from these cosmic showers are generated from data tables. Primary protons are followed from the top of the atmosphere and CRY keeps track of all required secondary particles until they reach the required elevation (sea level is selected for SoLid). Alpha- and heavier particles are a minor component of primary cosmic rays and they are therefore not taken into account in CRY. This causes a slight underestimation of the secondary particle rates as will be discussed in the following sections. CRY has an option to select the correct latitude (51.19 N in case of the BR2 building in Mol, Belgium) and to select an area, of which the size goes up to 300 m by 300 m, in which the secondary showers are generated. Overburdens can't be simulated, but this is not necessary in the case of SoLid as the overburden is nearly negligible and does not have a big impact on the detected muon rate. The influence of the shielding provided by the reactor building and the external layers of the detector on the muon rate are simulated in the Geant4 package.

All other generators are based on cosmic muon or neutron momentum distributions $I(E, \theta)$, quoted in the corresponding papers, which are valid at sea level and have been compared with data. Only the Gordon neutron generator has a latitude and altitude dependent distribution, with parameter values quoted for different locations in the USA. Here, the values for NYC (elevation 167 m, latitude 40.43 N) were used as this location is most similar to Mol (elevation around 40 m, latitude 51.19 N). The azimuthal angle distribution of the secondary particles is by all generators assumed to be flat.

In the CosmicGen package it is possible to set a bounding box (BB) by specifying its length, width and height. In this way, only secondary particles that reach the box are stored in the output file. This allows for a significant

reduction of the output size. Moreover, using the reduced file as an input for the SoLid Geant4 package saves a huge amount of computing time. The bounding box can for example be chosen as a small volume around the detector, or as large as the complete BR2 building. The optimal size of the box depends on which interactions of the secondary particles with the materials of the BR2 building are important. To get a good idea of the influence of interactions in the reactor walls and BR2 ceilings, a bigger box is desirable. The size chosen for the SM1 simulation will be discussed further on in section 4.1.3. The bounding box is always symmetrically positioned around the centre of the detector, which is defined as the origin in CosmicGen ¹.

Aside from the bounding box, also the length L of the square generation surface can be chosen. If used in combination with a bounding box, a too large generation surface causes excessive run times, while a too small generation surface alters the angular and energy distributions of the secondary particles. It must therefore be checked that the generation surface is set large enough so that the distributions and rates of cosmic particles are not altered significantly by further increasing the surface. The height of the generation surface above the bounding box d can also be chosen. In figure 4.1 a sketch of the setup can be seen. Figure 4.2 shows the SM1 coordinate system and the definition of the zenith (θ) and azimuthal (ϕ) angle.

4.1.1 CosmicGen muon files

As mentioned in the previous section, 3 generators are available for generating cosmic muon files. The muon rates obtained with the Reyna ($[138 \pm 1]$ Hz/m²), Guang ($[130 \pm 1]$ Hz/m²) and CRY ($[115 \pm 1]$ Hz/m²) generators are compared. It can be seen that the CRY rate is lower than the rates of the other 2 generators, this is due to the fact that only primary protons are considered in this generator.

Aside from the rate, also the energy distribution of the muons is compared. Figure 4.3 shows that the spectrum matches closely for the 3 generators and the mean energies are compatible (Reyna: $[6.438 \pm 0.002]$ GeV, Guang: $[6.167 \pm 0.002]$ GeV and CRY: $[6.179 \pm 0.002]$ GeV). The CRY spectrum shows a step-wise feature, but this is a known artefact and was already mentioned in other studies performed with this generator. The 3 generators differ slightly at the low energy range, but this does not affect muon studies performed with the SM1 data.

¹For the Phase 1 cosmics simulation the bounding box was further improved upon by not requiring a symmetrical volume around the detector so that the volume could be chosen to be more optimal.

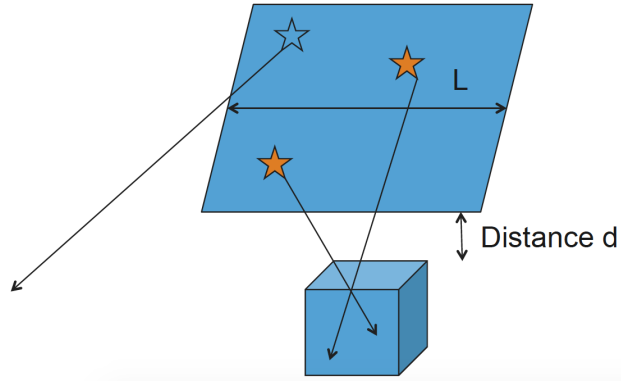


Figure 4.1: Sketch of the bounding box and generation surface with length L . When the bounding box option is selected, only the particles that cross the bounding box (orange stars) are stored in the output file.

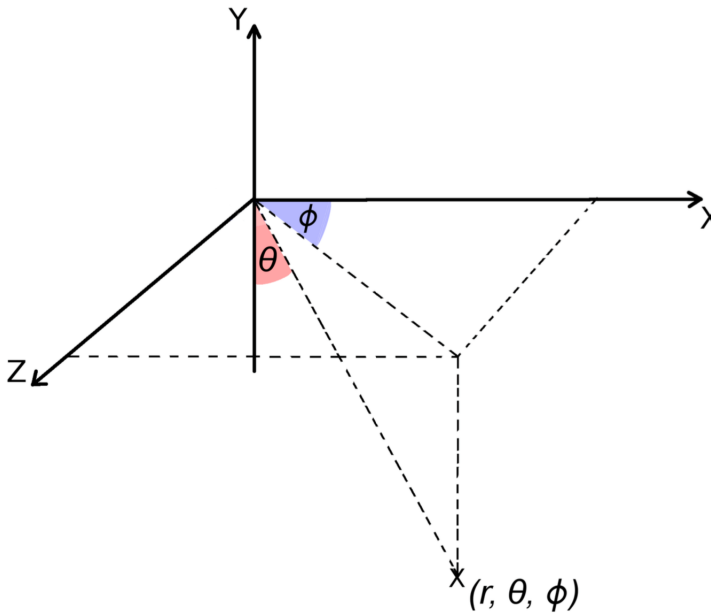


Figure 4.2: The SM1 coordinate system and definition of the zenith (θ) and azimuthal (ϕ) angle. The origin of the system is located in the middle of the detector plane closest to the reactor, which is located at negative z -values.

By saving only particles that hit a bounding box of SM1 size ($0.8 \text{ m} \times 0.8 \text{ m} \times 0.45 \text{ m}$) with a generation surface of $100 \text{ m} \times 100 \text{ m}$ located 3 m above the box, the energy distribution is slightly altered as seen in figure 4.4. The mean energy of muons is raised for the 3 generators (Reyna: $[7.18 \pm 0.05] \text{ GeV}$, Guang: $[7.28 \pm 0.04] \text{ GeV}$ and CRY: $[7.58 \pm 0.05] \text{ GeV}$). The reason why the energy is influenced by the bounding box is that the generators are based on momentum distributions $I(E, \theta)$, and a change in θ will thus also result in a change in energy.

Table 4.1: Comparison of the muon rate and energy for the 3 cosmic muon generators.

	Reyna	Guang	CRY
Muon rate (Hz/m^2)	138 ± 1	130 ± 1	115 ± 1
Mean energy (GeV)	6.438 ± 0.002	6.167 ± 0.002	6.179 ± 0.002
Mean energy with BB (GeV)	7.18 ± 0.05	7.28 ± 0.04	7.58 ± 0.05

The angular distributions of the cosmic muons with the 3 generators are compared as well. The zenith angle distribution can be seen in figures 4.5 and 4.6, without and with the SM1 size bounding box respectively. It can be seen that the 3 generators match very well and that there is again a small influence of the bounding box to be seen. The same can be noted for the azimuthal angle distribution in figures 4.7 and 4.8, which is flat at first (former figure) but shows some structure when a bounding box (latter figure) is implied. The position of the spikes matches with what is expected from the box orientation.

It can be concluded that the 3 muon generators match very well, so that either one of the 3 generators is suitable for further simulation through Geant4. It was opted to continue with Guang and Reyna, as the generation of these files does not take as much time as generating CRY files. The CosmicGen muon files produced with Guang and Reyna were compared again by Ibrahim Pinera after processing them with Geant4. No significant differences were observed. Further analysis, such as presented in section 4.3, is therefore, arbitrarily chosen, only performed on Guang files.

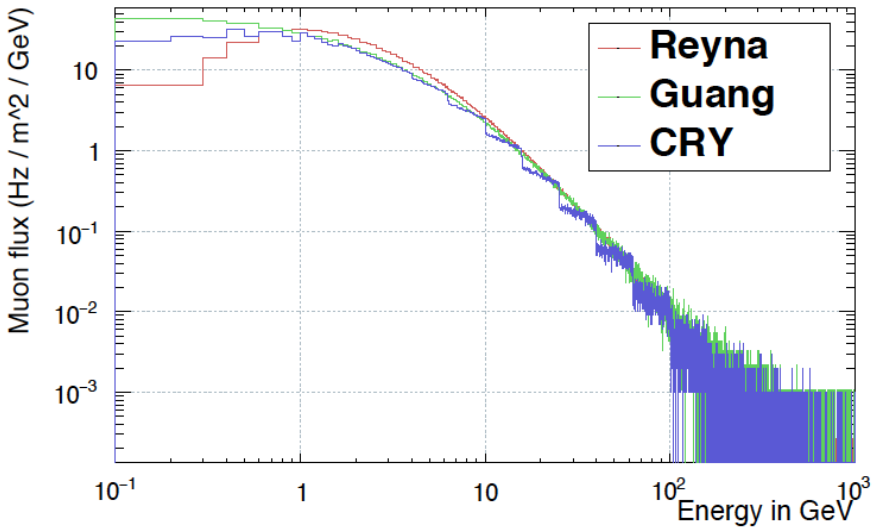


Figure 4.3: Energy distribution of cosmic muons simulated with 3 different generators, without a bounding box.

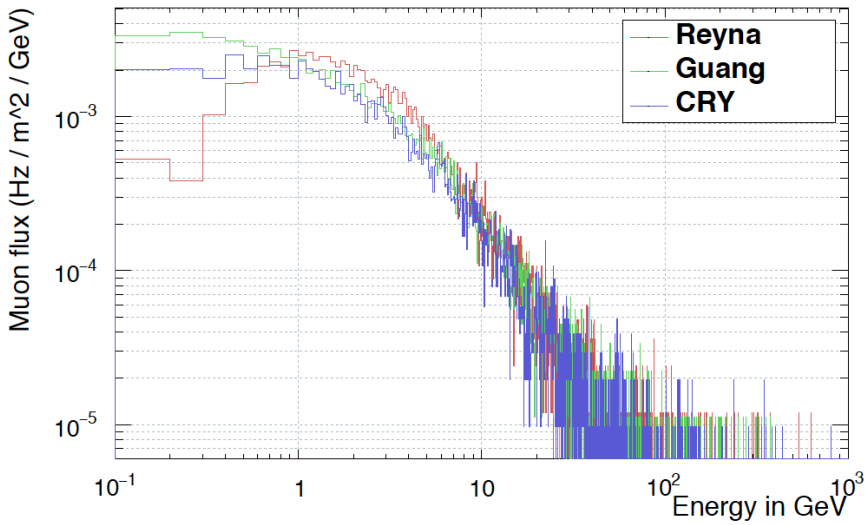


Figure 4.4: Energy distribution of cosmic muons simulated with 3 different generators, with a bounding box of SM1 size.

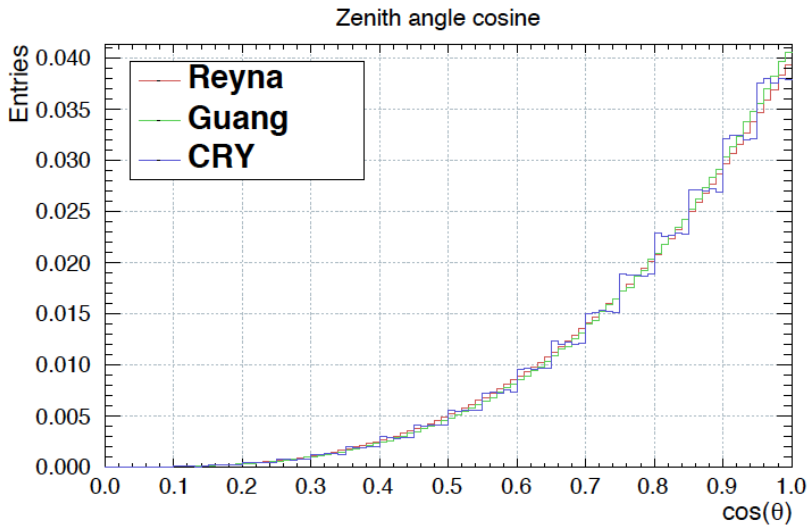


Figure 4.5: Zenith angle distribution of cosmic muons simulated with 3 different generators, without bounding box.

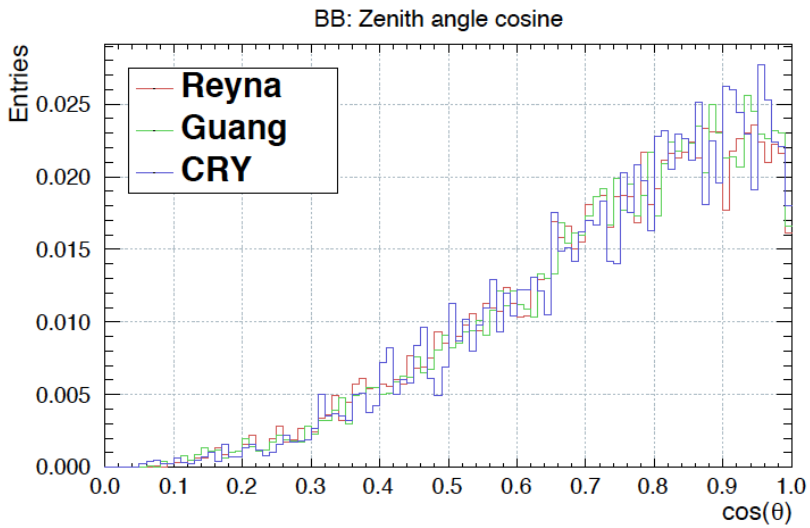


Figure 4.6: Zenith angle distribution of cosmic muons simulated with 3 different generators, with bounding box of SM1 size.

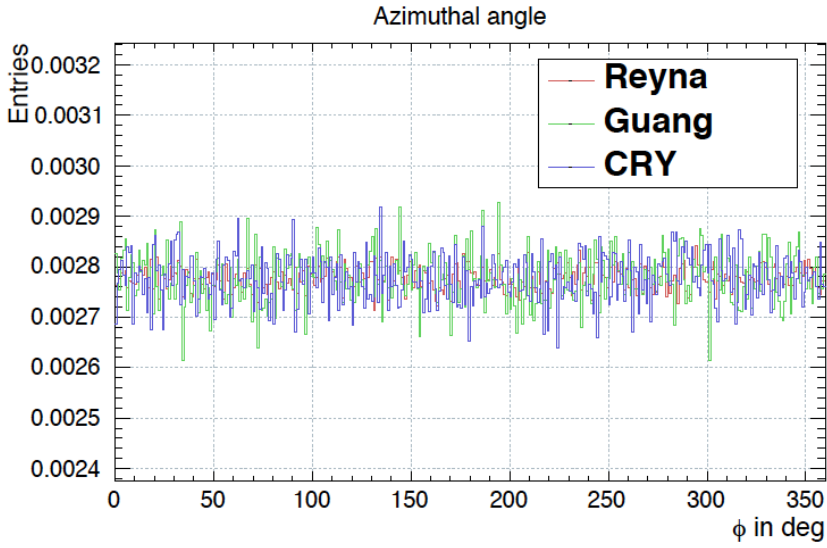


Figure 4.7: Azimuthal angle distribution of cosmic muons simulated with 3 different generators, without bounding box.

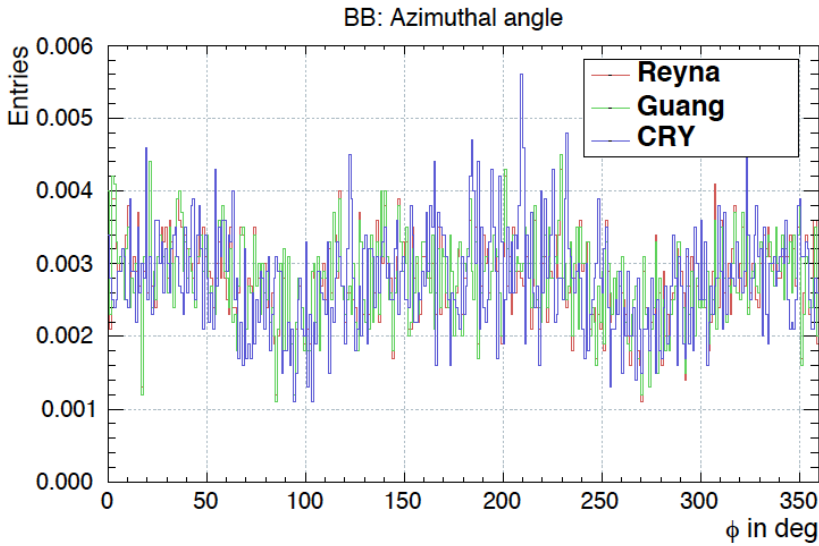


Figure 4.8: Azimuthal angle distribution of cosmic muons simulated with 3 different generators, with bounding box of SM1 size.

4.1.2 CosmicGen neutron files

CosmicGen neutron files can be produced with the CRY or Gordon generator. When comparing the neutron rate of both generators, CRY: $[28 \pm 0.09] \text{ Hz/m}^2$ and Gordon: $[55 \pm 0.18] \text{ Hz/m}^2$, it is clear that they do not agree as well as the results obtained with the 3 muon generators. There are several possible explanations for this discrepancy.

It was already noted in section 4.1 that the CRY generator is expected to give a lower rate as only primary protons are taken into account. However, this can not explain such a large neutron rate difference. Another difference between the 2 generators is that CRY allows to set the correct latitude, while the Gordon generator only provides parameter values for certain locations in the USA. The BR2 site has an elevation of around 40 m and is located at latitude 51.19 N. The closest match that the Gordon generator provides, is an elevation of 167 m and a latitude of 40.43 N. The latitude difference would, however, not be capable of explaining the factor 2 between the two rates as increasing the latitude in the Gordon generator would only increase the rate of neutrons even more, thereby increasing the difference between the 2 generators.

As CRY only allows for 3 different altitudes, the elevation is underestimated by choosing the sea level option and this would result in a slight underestimation of the rate.

Taking into account the 3 mentioned differences between the 2 generators, it is very hard to decide which generator is most correct or suited for the SoLid location. It was investigated whether the much more extensive simulation package Corsika [78] was able to show which of the rates was more reliable, but unfortunately there was no overlap in energy range as Corsika can only simulate neutrons down to 10 GeV.

When comparing the neutron energy spectrum generated with the 2 different generators, the shape is comparable although some differences can be seen in figure 4.9. The mean energies are also quite different (Gordon: $[119.3 \pm 0.1] \text{ MeV}$ and CRY: $[161.0 \pm 0.1] \text{ MeV}$). Using a bounding box of SM1 size brings the 2 values closer together (Gordon: $[122.4 \pm 0.3] \text{ MeV}$ and CRY: $[125.7 \pm 0.1] \text{ MeV}$), see figure 4.10.

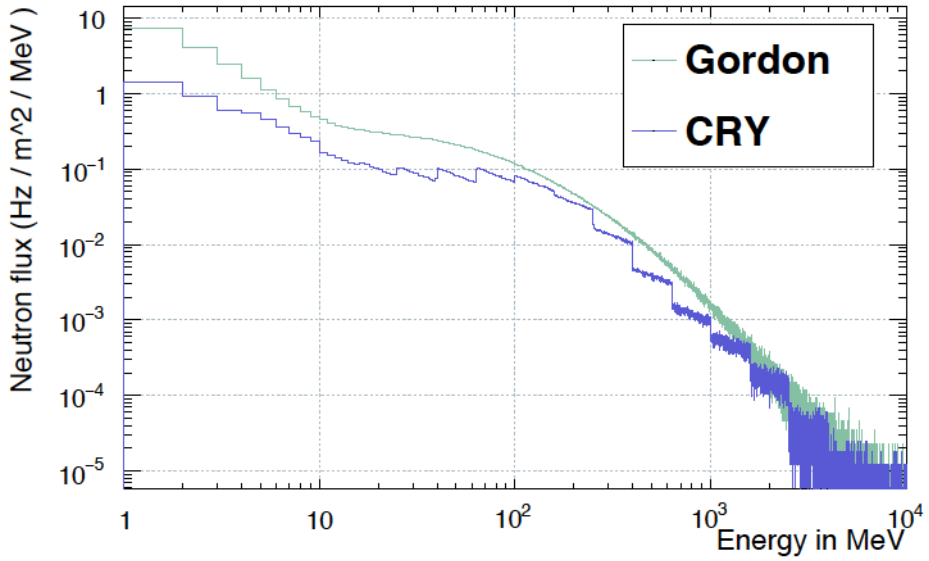


Figure 4.9: Energy distribution of cosmic neutrons simulated with 2 different generators.

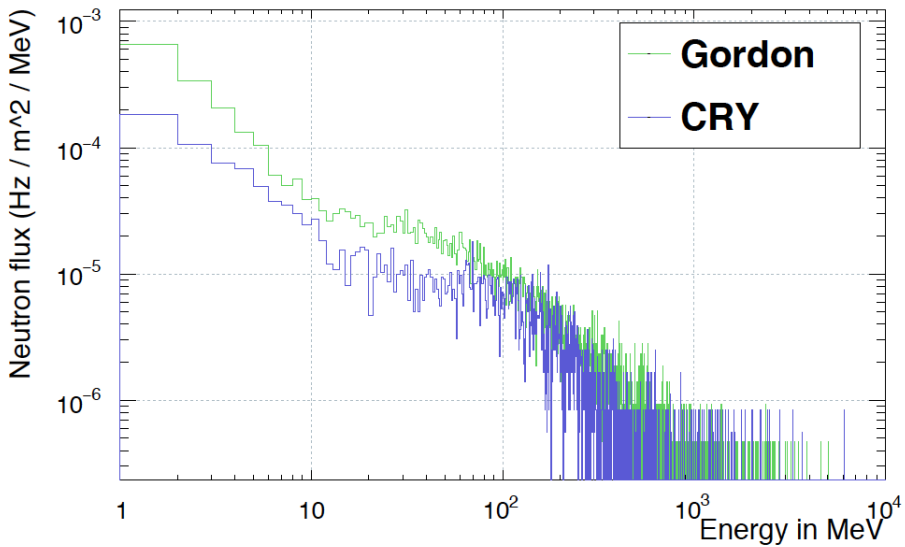


Figure 4.10: Energy distribution of cosmic neutrons simulated with 2 different generators with a bounding box of SM1 size.

Table 4.2: Comparison of the neutron rate and energy for the 2 cosmic neutron generators.

	CRY	Gordon
Neutron rate (Hz/m ²)	28 ± 0.09	55 ± 0.18
Mean energy (MeV)	119.3 ± 0.1	161.0 ± 0.1
Mean energy with BB (MeV)	122.4 ± 0.3	125.7 ± 0.1

Differences are also found in the zenith angle distribution with and without bounding box for the 2 generators, see figures 4.11 and 4.12. The azimuthal angle distribution is flat for both generators and changes similarly to the muon azimuthal angle distribution when imposing a SM1 size box, see figures 4.13 and 4.14.

It can be concluded that the neutron generators do not match as well as the muon generators do. There is a significant difference in the neutron rates and small variations in energy and zenith angle distributions. As explained, there are several known features in the 2 generators that could at least partially explain the discrepancies. However, it is not possible to claim which one of the generators is more correct. Therefore, CosmicGen neutron files from both generators are available for further processing with Geant4. To avoid underestimation, the Gordon neutron files were used for the shielding studies performed by Ibrahim Pinera as this generator predicts the highest neutron rate.

4.1.3 Settings for the CosmicGen files used in Geant4

Geant4 is a Monte Carlo (MC) simulation toolkit for the propagation of particles through matter. Most physics processes are available in Geant4, as well as most materials and particles. Particle energies range from 250 eV up till the TeV range. Ibrahim Pinera developed a dedicated SoLid Geant4 geometry which includes the complete BR2 building and the SM1 and Phase1 detectors. Figure 4.15 shows the Geant4 simulated SM1 detector, with HDPE shielding in green, the steel plate table in blue, wrapped cubes in white and external muon detectors in black and pink. Depending on the Geant4 input particles and the selected physics processes, one can create simulations of IBD interactions, fast neutrons, cosmic muons, and so on, in the required SoLid detector. A Geant4 output file contains, amongst other information, the deposited energy of the required particles within the detector.

To be able to compare the simulation results with data, as will be done in section 4.2, the Geant4 output files need to be processed by the ReadOut (RO)

simulation. The RO simulation converts the Geant4 output, the deposited energy of a particle, into the electronic signal that would be detected in case of a real energy deposit of that magnitude, taking into account the light yield, electronics amplification etc. This conversion of deposited energy to number of photons was tuned by using muons [79].

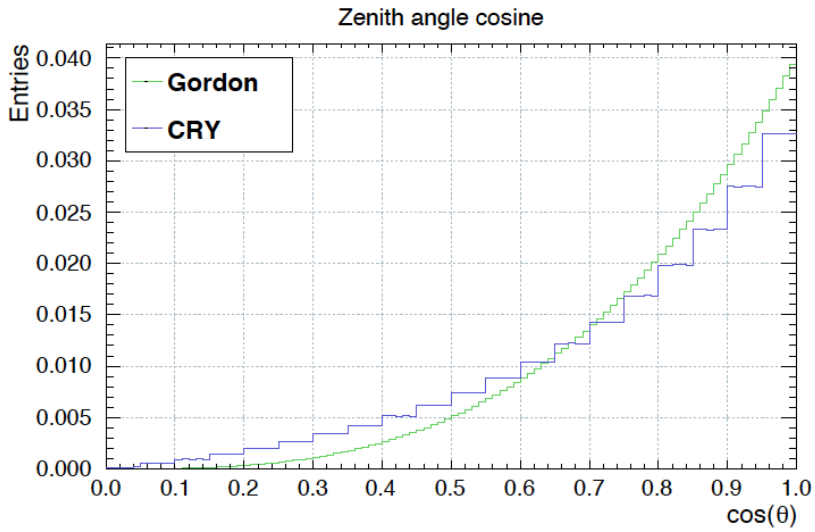


Figure 4.11: Zenith angle distribution of cosmic neutrons simulated with 2 different generators, without bounding box.

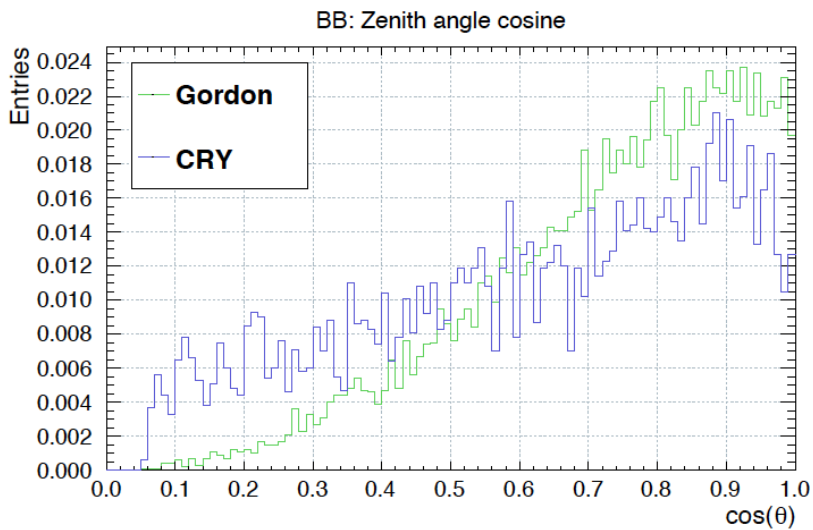


Figure 4.12: Zenith angle distribution of cosmic neutrons simulated with 2 different generators, with bounding box of SM1 size.

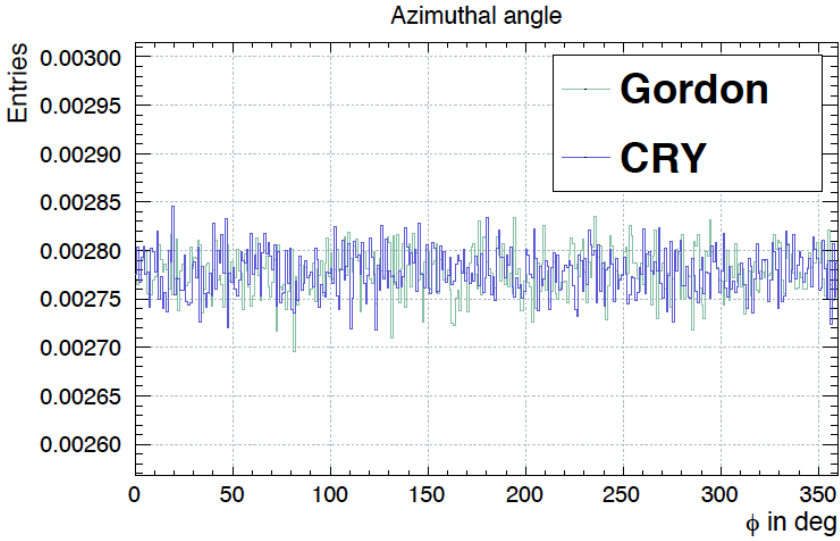


Figure 4.13: Azimuthal angle distribution of cosmic neutrons simulated with 2 different generators, without bounding box.

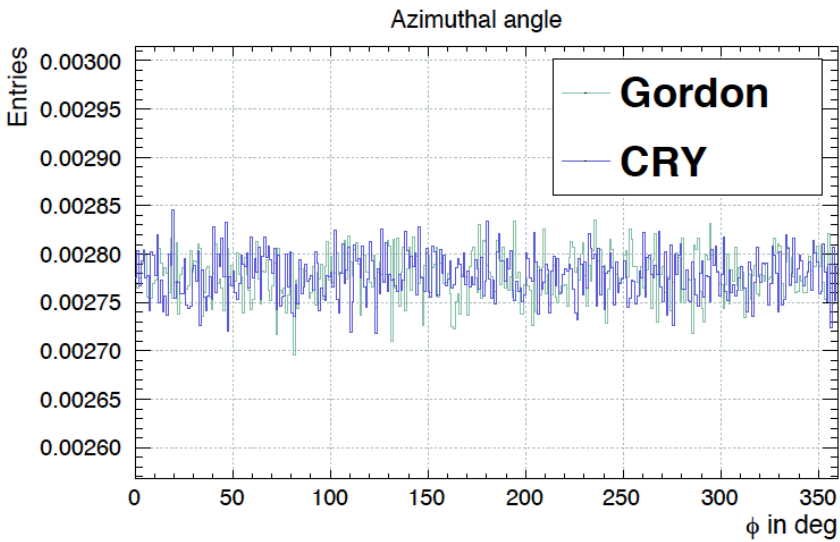


Figure 4.14: Azimuthal angle distribution of cosmic neutrons simulated with 2 different generators, with bounding box of SM1 size.

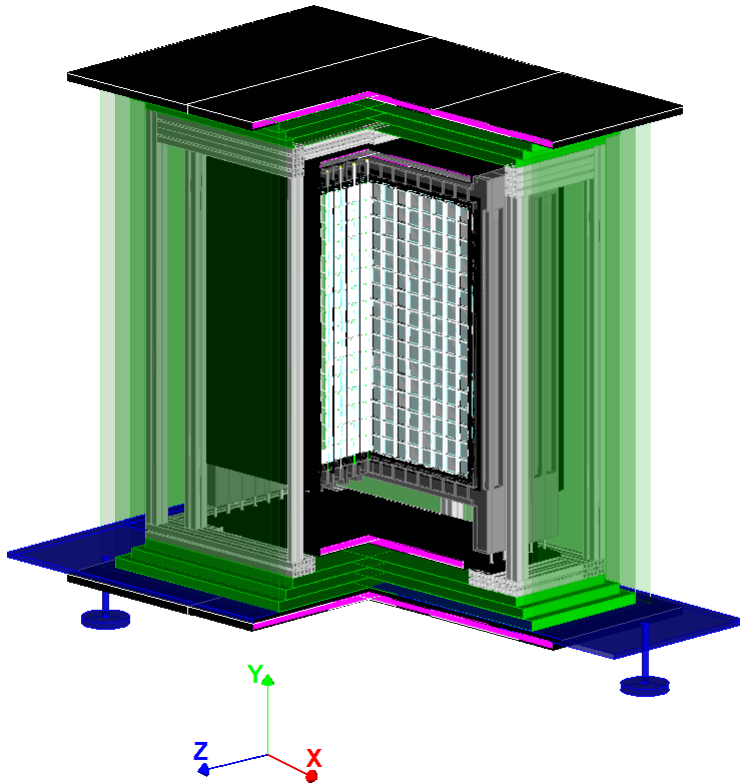


Figure 4.15: Geant4 simulation of the SM1 detector, with an indication of the SoLid coordinate system.

The bounding box used in sections 4.1.1 and 4.1.2 was chosen to be of SM1 size. This was set arbitrarily since the only point was to compare distributions between several generators. However, if the distributions themselves are of interest, than the settings should be optimised as to not alter the distributions by using a certain bounding box setting. To verify which bounding box and generation surface settings should be used for the CosmicGen generators in the SM1 simulation, Geant4 files are generated with 3 CosmicGen input files that each have a different bounding box setting: a box surrounding just SM1, a box surrounding the whole building and a size in between, see figure 4.16. Figure 4.17 shows the 3 different bounding boxes and the generation surface of $350 \text{ m} \times 350 \text{ m}$ above the BR2 building.

It turns out that interactions in the surroundings of the detector, especially in the wall of the reactor vessel, have an important influence on the signals

seen in the detector. It is therefore necessary to use a bounding box (40.8 m, 60.8 m, 60.45 m) that surrounds the whole building. After choosing the bounding box size, the ideal generation surface positioned 31 m above the detector centre (and thus 0.6 m above the bounding box) is also determined. The smallest size that does not alter the angular distributions significantly was found to be 350 m \times 350 m. Note that for CRY a surface of 300 m \times 300 m was chosen as this is the maximum size for that generator package. This could cause minor disturbances in the CRY output spectra. However, it was already decided, see section 4.1.1, that CRY will not be used as a generator for SoLid cosmic simulations due to the large amount of computational time it requires.

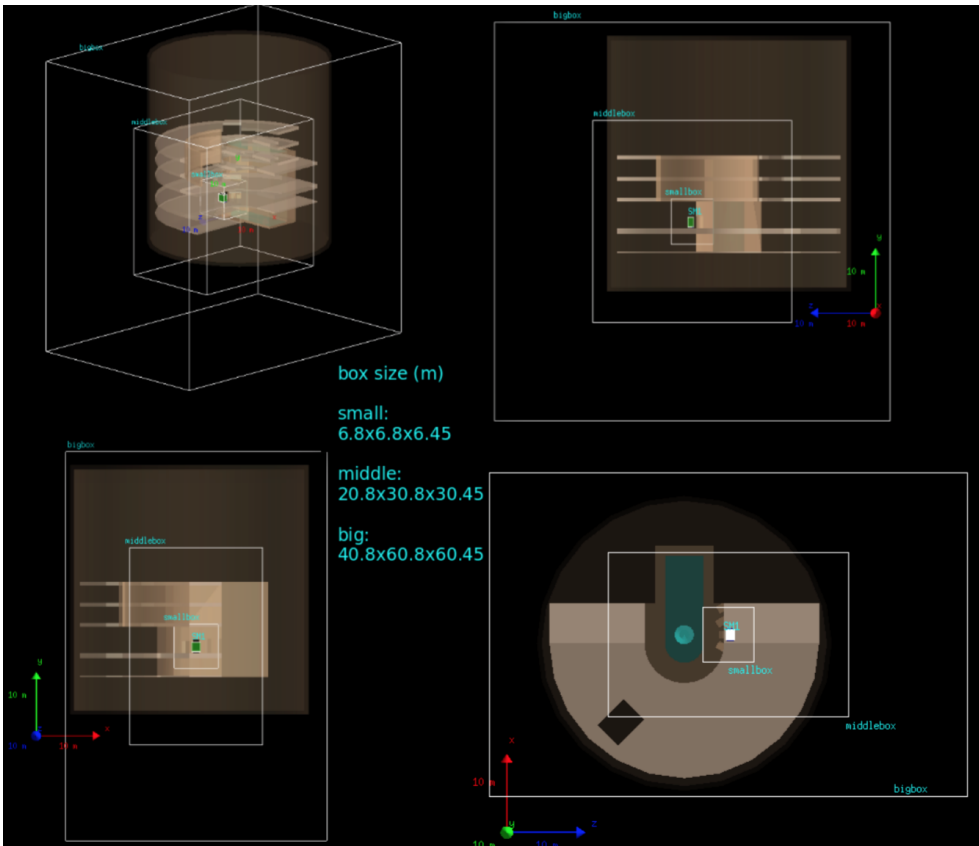


Figure 4.16: Sketches of the 3 different bounding boxes imposed on the Geant4 simulation model of the BR2 building. Thanks to Ibrahim Pinera.

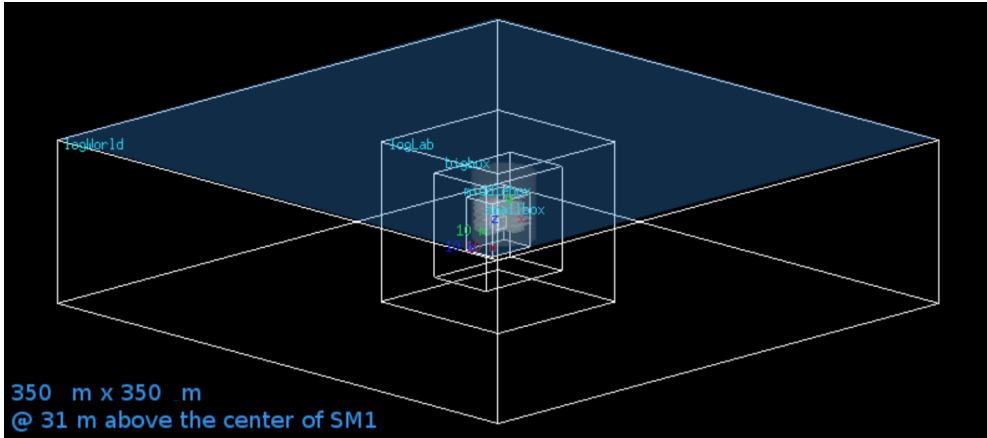


Figure 4.17: Sketches of the 3 different bounding boxes imposed on the Geant4 simulation model of the BR2 building, plus the $350\text{ m} \times 350\text{ m}$ generation surface (the top of logWorld). Thanks to Ibrahim Pinera.

4.2 SM1 data and simulation comparison for muons

After propagating the CosmicGen files through Geant4 and the RO simulation, the simulation files can be analysed. The basic analysis steps, peak identification, energy calibration, particle tagging, and so on, happen in the SoLid Analysis Framework called Saffron. A detailed outline of Saffron can be found in [72].

The event selection in Saffron is based on the time coincidence of signals occurring on multiple detector channels. These Saffron events contain interactions that cause signals in several channels, such as muons, positrons and neutrons. To reconstruct these types of events, one needs to apply certain cuts.

To identify muons, it is required that the event has a minimum energy of 8 MeV and a muon track needs at least 1 peak on 2 distinct horizontal (x-direction) and 2 distinct vertical (y-direction) channels. Muons that do not survive the last cut are referred to as a “muon cube” instead of a “muon track”.

As for data files, the RO simulation output can be processed by Saffron, generating what is called “output tuples”. These simulation tuples, further referred to as MC tuples, can then be compared to data tuples². A compar-

²The data tuples used are the S5 SM1 data set. This data set is dedicated to muon studies since the data in these files are centred around muons. A 3 ms window before and after a

tive study was performed for the cosmic muon files and is presented here.

Comparing the rate of muon tracks in the detector identified by Saffron shows reasonable agreement between data ($[50.35 \pm 0.07 \text{ (stat)} \pm 0.33 \text{ (syst)}]$ Hz) and simulation (based on Guang generator files, $[53.2 \pm 0.1 \text{ (stat)}]$ Hz). The data rate is determined by fitting the time between consecutive muons, as is done in figure 4.21 for both tracks and muon cubes. This method eliminates issues with dead-time which are present when using the absolute count of muons in a data file divided by the run time represented by the file. The systematic error is hereby obtained by repeating the fit, while excluding the first 4 bins, and taking the rate difference as a 1σ error. The simulation rate is obtained by using the absolute count of detected, simulated muons divided by the simulated time since dead-time issues are not present in simulation.

The zenith angle distributions also show good agreement between simulation and data (see figure 4.18), as do the distributions of the azimuthal angle (see figure 4.19). For the azimuthal angle distribution it can be seen that the distributions show some large spikes that were not visible in the output of CosmicGen, see figure 4.8. These spikes are thus caused by the reconstruction in Saffron. This is to be expected since the reconstruction precision in Saffron is limited by the 5 cm position accuracy in SM1.

As a last check, the energy of the muon cube objects obtained with simulation and with data is compared, shown in figure 4.20. The two distributions match well, but this is no surprise as this energy spectrum was used to fine-tune the readout simulation, as was mentioned in section 4.1.3.

The good agreement between data and simulation shows that the simulation chain concerning cosmic muons is working properly. Similar studies, performed by Ibrahim Pinera, showed the same behaviour for the cosmic neutron simulations. This allows the use of the cosmic simulation to study several shielding options for the full-scale Phase 1 detector. The most important result was that a 30 cm water wall around SM1 would have been able to eliminate 97% of the thermal neutrons and 92% of the fast neutron interactions inside the detector [80]. This led to the decision to place such a water wall around the Phase 1 detector.

4.3 Muons and “after-muon” events in SM1

After the muon identification in the SM1 data, explained in section 4.2, several studies can be performed with these objects. The work presented in this section uses a subset of reactor-on (from 21/02/2015 till 23/02/2015) and

muon is stored, plus a 100 ms shifted off-time window.

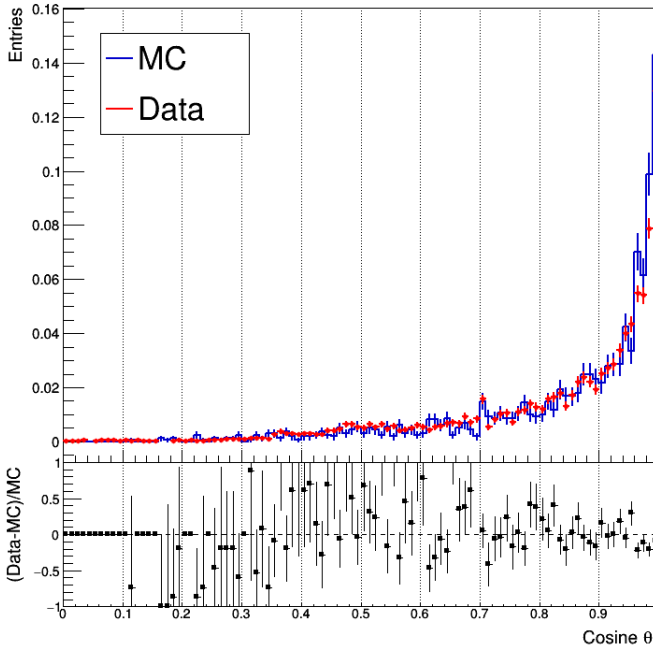


Figure 4.18: Comparison of the cosine θ distribution of muon tracks for the Guang based Monte Carlo tuples and data tuples.

reactor-off (from 01/03/2015 till 07/03/2015) data. It will be shown that muons are not only a background for SoLid but can provide very useful insights in the working of the detector.

By plotting the time difference between the occurrence of 2 consecutive muons and fitting this distribution with an exponential, the muon rate is obtained. Figure 4.21 shows the muon rate determination for muon tracks and muon cube objects combined. A rate of $R_\mu = [69.18 \pm 0.02 \text{ (stat)} \pm 0.93 \text{ (syst)}]$ Hz is found. The systematic error is obtained by repeating the fit, while excluding the first 4 bins, and taking the difference in R_μ as a 1σ systematic error.

Muons can undergo several reactions in the detector, thereby creating different particles. These so-called “after-muon” events can be studied with the use of an on-time and off-time window approach. The particles following shortly after the muon are stored (this is the on-time window) and similarly particles found in a window of the same length, but occurring some time later (this is the off-time window) are stored. The off-time window can then

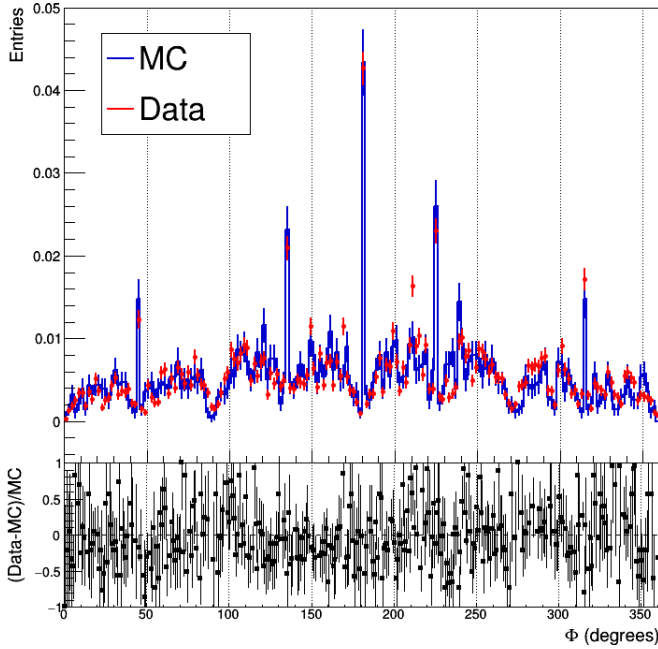


Figure 4.19: Comparison of the azimuthal angle distribution of muon tracks for the Guang based Monte Carlo tuples and data tuples.

be used to evaluate the backgrounds of the process under investigation.

Figure 4.22 shows a schematic representation of the on-time and off-time window used in the study of Michel electrons. Michel electrons are electrons created in the decay at rest of a muon. The study of the time between the passage of the muon and the following Michel electron, allows for the determination of the muon decay time. The on-time window starts $1 \mu\text{s}$ after the muon passage to avoid spurious electronics triggers which can happen after the occurrence of a muon, which causes high intensities recorded by the MPPCs. To avoid matching the muon with a low energy photon or other unrelated signals and due to the known high energy spectrum of the Michel electrons [81], a minimum visible energy of 1 MeV is required. The same criteria are used for the off-time window, which is shifted over 1 ms.

It is found that 2.97 % of the muons leaving a signal in the detector decay and produce a Michel electron. The total rate of Michel electrons therefore is $[2.06 \pm 0.19] \text{ Hz}$.

Using the on-time and off-time window approach, there are 2 comple-

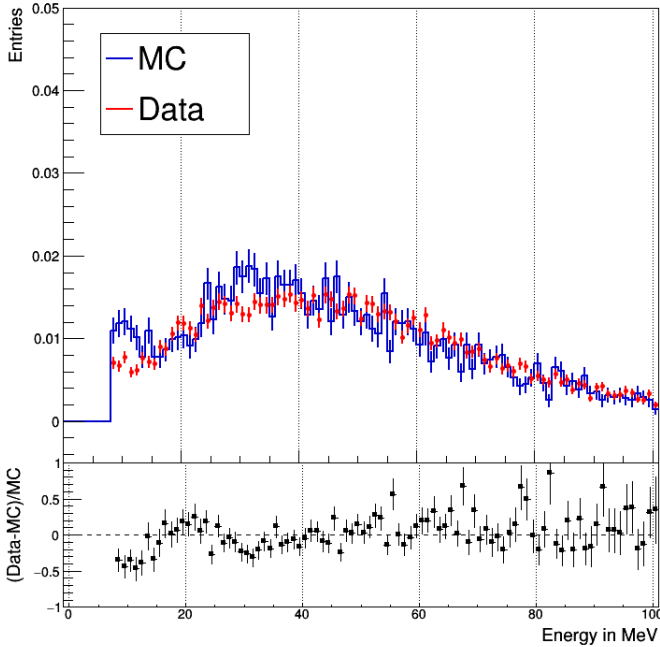


Figure 4.20: Comparison of the energy distribution of muon cubes for the Guang based Monte Carlo tuples and data tuples.

mentary methods to obtain the muon decay time. The first method does not use the off-time window and fits an exponential plus a constant to the time difference distribution, assuming a flat background. The decay time found with the fit in figure 4.23 is $\tau_\mu = [2.272 \pm 0.005(\text{stat}) \pm 0.082(\text{syst})] \mu\text{s}$, to be compared with the value quoted in literature of $[2.1969811 \pm 0.0000022] \mu\text{s}$ [82]. The off-time window is also plotted in this figure to show that the flat-background approximation is valid.

The second approach to determine the muon decay time, is to subtract the off-time window from the on-time window and to fit the subtracted distribution with a simple exponential. The fit is shown in figure 4.24 and gives a value of $\tau_\mu = [2.279 \pm 0.003(\text{stat}) \pm 0.034(\text{syst})] \mu\text{s}$.

The systematic error on the muon decay, for both methods, is obtained by repeating the fit, while excluding the first bin, and taking the difference in τ_μ as a 1σ systematic error.

Both values obtained for the muon decay time are in agreement with each other within 1σ and with the value quoted in the PDG within 2σ . This result

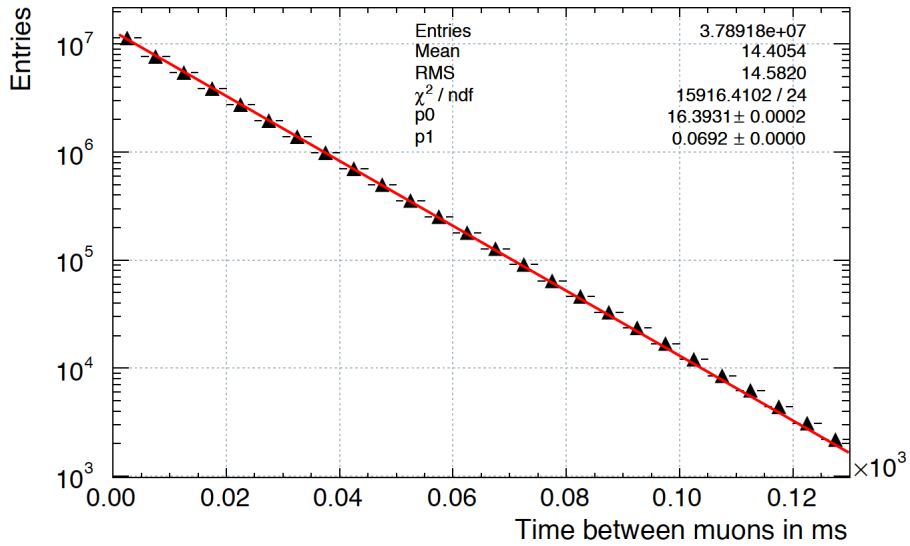


Figure 4.21: Determination of the muon track and cube rate in the SM1 detector. The fit gives a rate of $R_\mu = [69.18 \pm 0.02 \text{ (stat)} \pm 0.93 \text{ (syst)}] \text{ Hz}$.

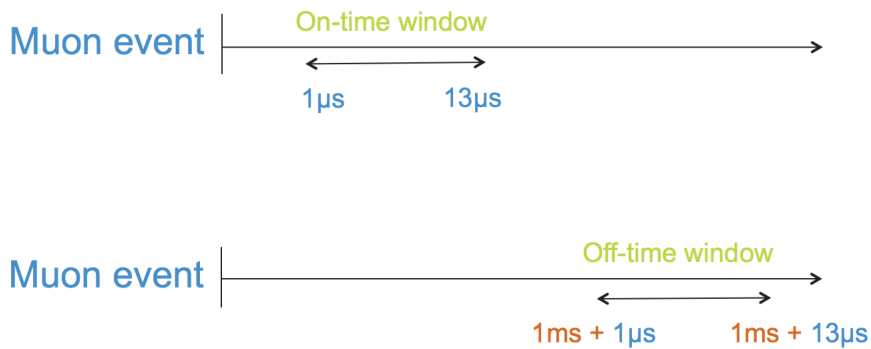


Figure 4.22: Schematic representation of the on-time and off-time window approach used for the study of Michel electrons.

strengthens the trust in the understanding of the timing of the readout and in the identification of basic objects in the data of the SM1 detector. Moreover, the study of Michel electrons is similar to the study of IBD events, in the way that a prompt signal (in this case the muon) is followed by a delayed signal (the Michel electron), and it shows that the SM1 detector is capable of

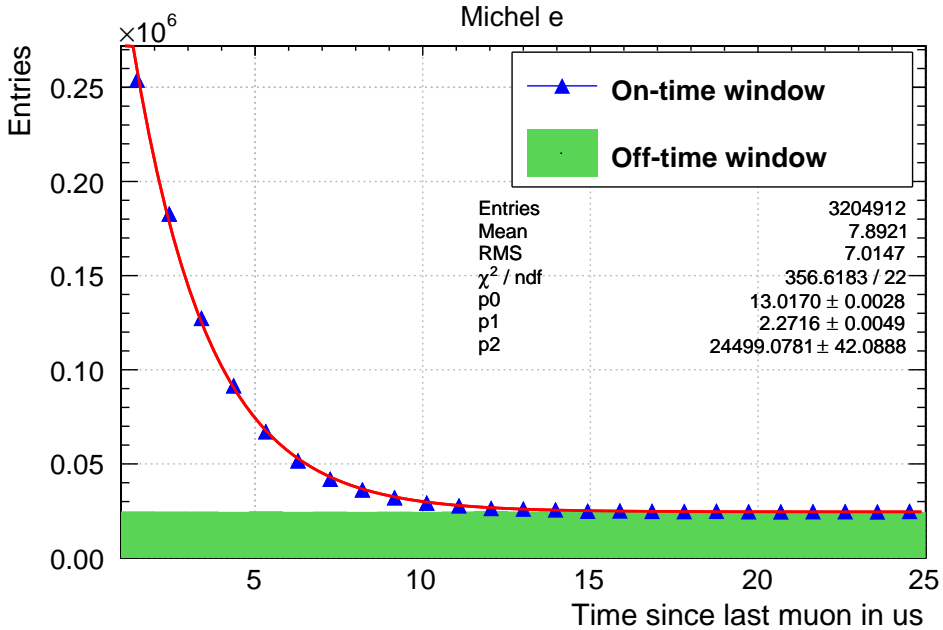


Figure 4.23: Determination of the muon decay time by fitting an exponential plus a constant to the on-time window. A decay time of $\tau_\mu = [2.272 \pm 0.005(\text{stat}) \pm 0.082(\text{syst})] \mu\text{s}$ is obtained. The off-time window is plotted in green.

correctly identifying these types of events.

To get more information about the muon decay and Michel electrons in the SM1 detector, several parameters can be investigated. Figure 4.25 shows the shortest distance between the Michel electron and the muon track in the on-time and off-time window. Figure 4.26 shows the on-time window with subtraction of the off-time window. It is clear that the Michel electron is detected close to the muon track, mostly located within 2 cubes distance ($\Delta R < 10 \text{ cm}$).

Figure 4.27 shows the energy of the Michel electron for the on- and off-time window. Figure 4.28 shows the Michel electron energy where the off-time window is subtracted from the on-time window. A clear increase from 3 to 20 MeV can be seen in the on-time window. However, the energy distribution of Michel electrons is expected to peak at higher values, around 50 MeV [81]. This is an indication that the energy of tagged electron signals is not well reconstructed. The most likely cause is that the energy of the Michel electrons is deposited over multiple cubes, or that light leaked, thereby reducing the

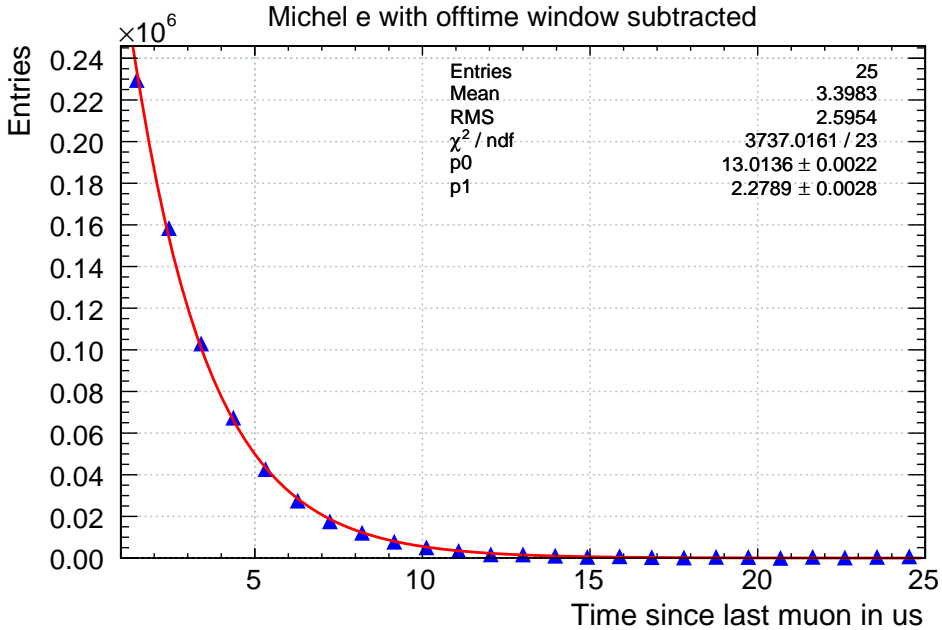


Figure 4.24: Determination of the muon decay time by fitting an exponential to the off-time subtracted time distribution. A decay time of $\tau_\mu = [2.279 \pm 0.003(\text{stat}) \pm 0.034(\text{syst})] \mu\text{s}$ is obtained.

reconstructed energy. It will be taken into account for Phase 1 that the energy of several cubes can be added together to determine the energy deposition made by a certain particle.

Aside from Michel electrons, one can also look for spallation neutrons following the detection of a muon. Spallation neutrons are created by energetic muons breaking up heavy nuclei in the detector or materials in the vicinity. The neutrons thermalise and can be captured by the ${}^6\text{Li}$ screens. From the time between the passage of the muon and the neutron signal, one can determine the neutron capture time. This is a useful parameter in the search for IBD signals. The note [83] by L. Kalousis discusses this study, together with a study of the Michel electrons. A value of $\tau_n = 89.81 \pm 2.63(\text{stat}) \mu\text{s}$ is found for the neutron capture time. The results on Michel electrons in this note match closely with the values that are shown in this section.

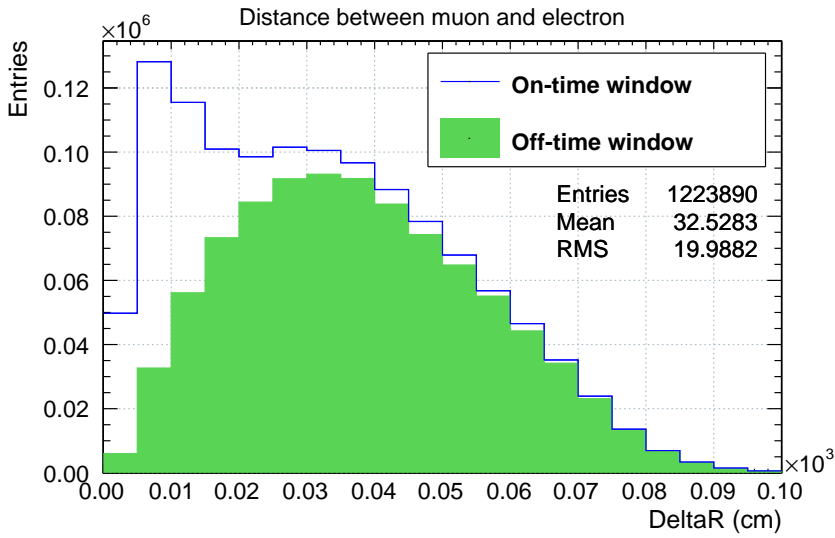


Figure 4.25: The shortest distance between the muon track and the Michel electron for the on-time and off-time window.

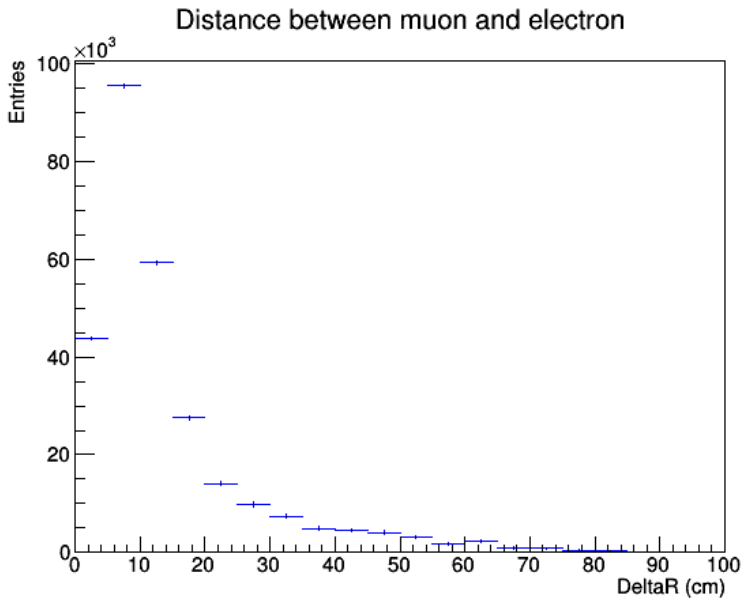


Figure 4.26: The shortest distance between the muon track and the Michel electron, off-time window subtracted.

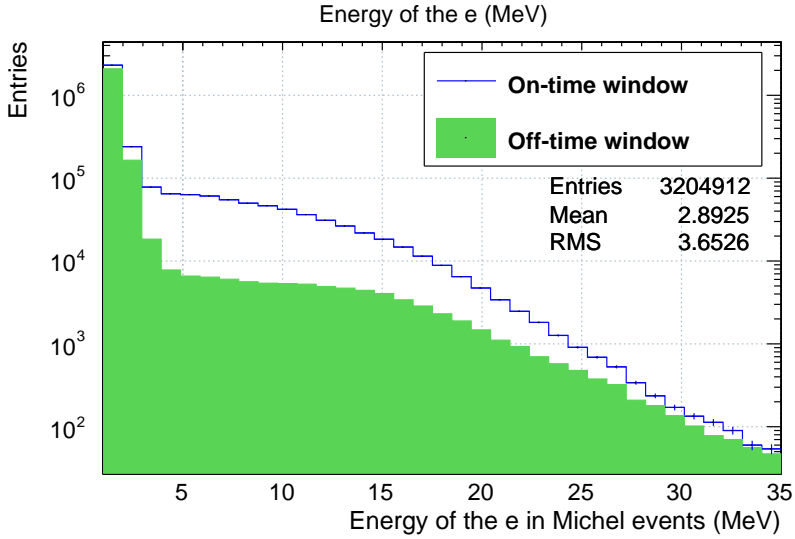


Figure 4.27: The energy of the Michel electrons for the on-time and off-time window.

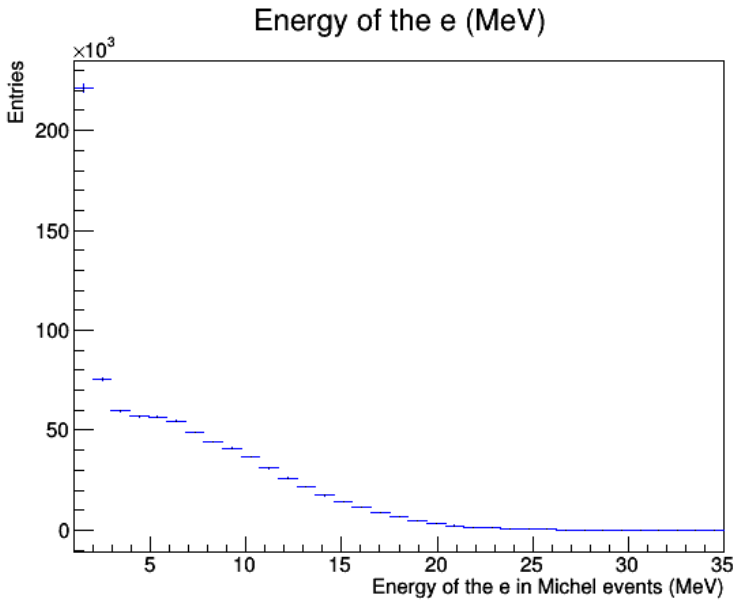


Figure 4.28: The energy of the Michel electrons, off-time window subtracted.

4.4 Conclusion

In this chapter the CosmicGen software package was discussed. The package contains 2 neutron generators and 3 muon generators. It was found that the muon generators (Guang, Reyna and CRY) match very well in terms of rate, energy and angular spectra. It was chosen not to proceed with CRY as this generator takes most computational time to create output files. Arbitrarily the Guang generator was chosen from the remaining two as the basis for further analysis.

The agreement between the neutron generators, Gordon and CRY, was less good than in the muon case. Especially the factor 2 between the rates makes it very hard to draw conclusions about which generator to use for further studies. Energy and angular spectra follow roughly the same shape but some discrepancies can be seen. For further studies it is therefore recommended to perform the study on both generator files.

Comparing muon simulation tuples with data tuples showed very good agreement between the rates of muon tracks, their angular distributions and the energy distributions of muon veto cubes. This strengthens our trust that the muon simulation chain is trustworthy.

Section 4.3 shows a dedicated study of muons and muon decay events in the SM1 detector. A muon rate of $R_\mu = [69.18 \pm 0.02 \text{ (stat)} \pm 0.93 \text{ (syst)}] \text{ Hz}$ is found in the prototype.

A study of the Michel electrons with the use of an on- and off-time window provides the muon decay time in two distinct ways; by a combined fit in the on-time window ($\tau_\mu = [2.272 \pm 0.005 \text{ (stat)} \pm 0.082 \text{ (syst)}] \mu\text{s}$) and a simple exponential fit in the off-time subtracted window ($\tau_\mu = [2.279 \pm 0.003 \text{ (stat)} \pm 0.034 \text{ (syst)}] \mu\text{s}$). These values fall within 2σ from the value quoted in literature ($[2.1969811 \pm 0.0000022] \mu\text{s}$). These results show that it is possible to study prompt-delayed signals with the SM1 prototype, as is the goal when searching for IBD signals.

5

Phase 1 detector

A combination of a sub-optimal readout system, low light-yield and a limited reactor-on data period made it impossible to detect IBD signals with the SM1 prototype detector, as was mentioned in section 3.6. However, the goal of SM1 was to test the feasibility of the large-scale use of the technology and therefore it provided valuable lessons for the full detector, as will be discussed in section 5.1. Section 5.2 will provide an overview of the upgraded Phase 1 properties.

The construction of the Phase 1 detector took place at the labs of Ghent University. I was therefore, as with SM1, very involved in the procurement of materials, planning, training of manpower and construction itself. Section 5.3 will provide details on the protocols dedicated to the Phase 1 construction. Like for SM1, it is of extreme importance to keep track of several parameters to be able to determine the proton content of the detector; precise protocols are thus needed.

LPC CAEN developed an automated system to commission the Phase 1 frames with radioactive sources. The Calipso (Calibration per plane for SoLid) system will be discussed in section 5.4. I took care of the on-site commissioning planning and the fixes performed on frames showing issues during initial commissioning.

On October 20, 2017, 4 out of 5 Phase 1 modules were completely commissioned and transported to the SCK•CEN. The 5th module was transported later in February due to slight delays in the electronics manufacturing.

5.1 Lessons learned from SM1

The dedicated SM1 paper [69] describes how there are two areas where large improvements should be made to get a sensitive Phase 1 detector.

A major issue for SM1 was the lack of time for electronics development

and testing. This caused several flaws in the system that reduced the neutron detection efficiency and the pulse-shape discrimination power significantly. For Phase 1 there was more manpower and time to establish a stable read-out chain and to commission the electronics system. The Phase 1 read-out system is discussed in [84]. Aside from the system upgrades themselves, a major improvement for Phase 1 is the cooling of the complete detector, which reduces the electronics noise significantly.

A second way to improve Phase 1 performance is to tackle the low light-yield measured with the SM1 prototype. The upgrades consist of:

- Using double cladded read-out fibres
- Doubling the number of read-out fibres
- Using mirrors with better reflectivity to cover 1 end of the fibres
- Using white HDPE bars on the side of the frames
- Smoother polished cubes
- Thicker Tyvek wrappers around the cubes

Studies indicate that the light-yield upgrades improve the energy resolution from 20% to 14% for electrons or positrons depositing 1 MeV in a single cube [63].

At last, to improve the neutron capture efficiency compared to SM1, the amount of ^6Li screens is doubled and a polyester backing of $200\ \mu\text{m}$ is added to the screens.

5.2 Phase 1 properties

The Phase 1 detector is about 5 times the SM1 prototype size. It consists of 5 modules, which each have 10 planes of 16 by 16 cubes, a total of 12800 cubes. The PVT cubes have the same dimensions as in the SM1 case. Most of them are now equipped with two $225\ \mu\text{m}$ (+ $200\ \mu\text{m}$ polyester backing) thick LiF:ZnS(Ag) screens and wrapped in $105\ \text{g/m}^2$ Tyvek paper. Leftover Li screens from the SM1 construction period were used to equip cubes located at the edge of the frames. These cubes will be referred to as “old” cubes, in contrast to the “new” cubes.

One of the 2 screens added to the cubes is placed on a side with no fibre grooves and which is perpendicular to the reactor-detector baseline. The other screen is placed parallel to the baseline and is therefore located on a surface with grooves. This screen therefore also has holes matching the grooves so that the double cladded WLS fibres can pass through. It is therefore referred to as the “punched” Li screen (opposed to the “plain” screen). Like

for SM1, the fibres have a $3 \times 3 \text{ mm}^2$ cross-section and fit in the $5 \times 5 \text{ mm}^2$ grooves.

The frames themselves are made from 2017a hollow aluminium bars which house the electronics cables. In contrast to SM1, the bars have been sent to a company to get a chrome passivation treatment to eliminate Al oxidation.

Every 2.5 cm, a hole is drilled in the Al bars to accommodate the readout fibres. The holes are also used to hold the MPPC connectors. The MPPCs, type S12572-050P from Hamamatsu, are optically coupled to the WLS fibres by optical grease as was done for SM1. On the other end of the fibre, there is now no aluminium tape, but a mirror connector with improved reflectivity¹. MPPC and mirror positions still alternate along the sides of the frame. Because of the doubling of fibres, this means that a cube is read out by 2 MPPCs in each direction, on opposite sides of the frame.

The electronics cables used for Phase 1 are “flat” cables and the system was designed so that all cables exit at the right-hand² side of the frame and are thus fed through the corners of the hollow bars. The cables end in a connector which is attached to the closing plate on the right-hand side. These connectors in turn couple to the electronics box (EB). Every frame thus has its own electronics box. The electronics themselves will not be discussed in this thesis as they were not part of the construction efforts made in Ghent. More information can be found in the dedicated paper [84].

As for SM1, HDPE bars are placed between the edge of the Al frame and the cubes, although they are now white to increase reflectivity at the edge. To further increase reflectivity the cubes are now covered, on either side of the frame, by a large white Tyvek sheet. These sheets do not provide the same rigidity as the HDPE cover sheets in the SM1 detector. Before attaching the frames into modules, they are therefore held together by wooden plates.

Ten frames form a module and are attached on their left side to a support structure. The structure itself consists of 2 parts: the part at which the frames are attached, and a lower half on wheels to be able to transport the modules easily. Figure 5.1 shows one of the modules in a test set-up. The electronics boxes are attached and at the front the white Tyvek sheet covering the cubes of the last frame is visible.

The complete Phase 1 detector is housed within an isolated container. In this way it is possible to cool the entire system, thereby reducing the electronic noise significantly. The electronic boxes on the side of the frames are also

¹The mirrors were cut from a $70 \mu\text{m}$ thick Mylar foil with an aluminium deposition of 200 nm.

²Right and left are defined from the point of view of facing the detector with the reactor behind it.



Figure 5.1: Picture of a Phase 1 module with electronics boxes attached in a test set-up at the Ghent University lab.

equipped with fans to circulate the cool air efficiently. Figure 5.2 shows 1 module inserted in the container with its electronics boxes attached to the right side. On top of the boxes, the cooling fans can be seen. In the picture I am attaching the service box which supplies the high voltage (HV) to the electronics and ensures data transfer to the outside of the container.

To reduce the impact of fast neutrons, a HDPE plate of 3 cm is placed at the beginning and at the end of the 5 modules. After the transport to BR2, more shielding is installed outside the container. More HDPE plates are arranged on top of and below the container. As an extra neutron shielding, cadmium plates are hung from the back of the container and are also placed on top of and below the container at the position of the sensitive detector volume. As a result from the cosmic studies with the SM1 detector (see section 4.2) it was decided to place a 50 cm thick water wall around the whole container to reduce the impact of spallation neutrons significantly. Figure 5.3 shows the HDPE shielding on top of the container and the water wall from the side of the detector.

The container is equipped with an automated calibration system CROSS (Calibration On Site SoLid) to perform regular calibration campaigns with radioactive sources. Actuators are foreseen inside the container to move the



Figure 5.2: Picture of 1 module inserted in the container. Electronics boxes, fans and service box are visible.



Figure 5.3: The left figure shows the HDPE plates on top of the container. The right figure shows the closed water wall from the side. The cooling system and the electronics rack are also visible.

different modules away from each other so that a source can be inserted, with the aid of the CROSS robot, into the gap between modules. A window is foreseen in the container door and water wall to be able to manually insert the required radioactive source with a pair of tongs. For more information about CROSS, see [85].

The initial installation of the Phase 1 detector took place with 4 modules. With this set-up, the initial commissioning was performed and a first data set was collected during reactor-on and -off periods. The “proto” set-up of 4 modules is shown in figure 5.4. The CROSS calibration system is also visible on the top left. It is important to note that the back of the water shielding, at the door of the container, was not yet installed during the data taking with 4 modules. It is therefore expected that this data-set will suffer from slightly higher backgrounds.



Figure 5.4: Picture of 4 modules inserted in the container, plus 2 HDPE plates, one at the front and 1 at the back of the container. All electronics boxes and service boxes are cabled and the cooling system is attached. In the bottom right, part of the cooling system that is foreseen for module 5 is already available. In this picture the reactor is situated at the back, behind the container.

5.3 Construction and protocols

Construction of the Phase 1 detector started in December 2016 and took just under 1 year to complete. This effort involved a huge amount of manpower and time. To make sure the construction was carried out in an efficient and consistent manner everybody was trained by experts at Ghent University. Aside from these trainings, detailed protocols needed to be followed. These

protocols have undergone many iterations taking into account precision, efficiency, cleanliness and database storage of specific parameters. With a special thanks to P. Van Mulders for an extensive overhaul of the Li screen protocol (see section 5.3.1) and to L. Manzanillas, V. Pestel and M. Labare for the frame filling protocol (see section 5.3.3). The following sections will provide an in-depth overview of the construction protocols for future reference.

5.3.1 $^6\text{LiF:ZnS}$ screens protocol

To avoid any contamination of the Li screens, it was very important to clean all working surfaces and tools properly at the start of each day. For the same reason the LiF:ZnS was only to be touched with fabric gloves, while other materials were handled with rubber gloves, such as the packaging of the sheets.

In case any dirt was found on the Li sheets or screens during one of the processing stages, it was brushed off with a finger (in fabric glove), or cleaned with a microfiber towel and distilled water and left to dry afterwards. After identification of the origin of the dirt, the contaminated surfaces or tools were re-cleaned.

For every LiF:ZnS sheet, of size 503 mm \times 200 mm, a paper tag was prepared with the appropriate bar-code, batch number and Li type (old or new), shown in figure 5.5 on the left. To cut the sheets in half, an A4-paper was placed atop and below the LiF:ZnS sheet and placed as a whole under a (cleaned) cutting machine. The set-up is shown in figure 5.5 on the right.

To equip the sides of the cubes where no fibres pass through, one half of the sheet was cut into 20 square, "plain" screens. The thickness of 4 randomly selected squares was measured and written down before they were stored in a plastic box with the paper tag. The other half of the Li sheet was punched with the dedicated (wooden) punching tool and a press shown in figure 5.6, resulting in the "punched" screens. These were stored together with the plain screens from the same sheet.

5.3.2 Cube construction protocol

Preparation of the cubes

The Phase 1 cubes and their grooves were machined by Coenen Plastics N.V. [86] and transported to Ghent University in plastic crates. During the machining, the cubes were cooled with grease. Therefore, it was necessary to remove the grease and other dirt before the cubes could be wrapped. The cubes were handled with plastic gloves to eliminate further grease contamination.

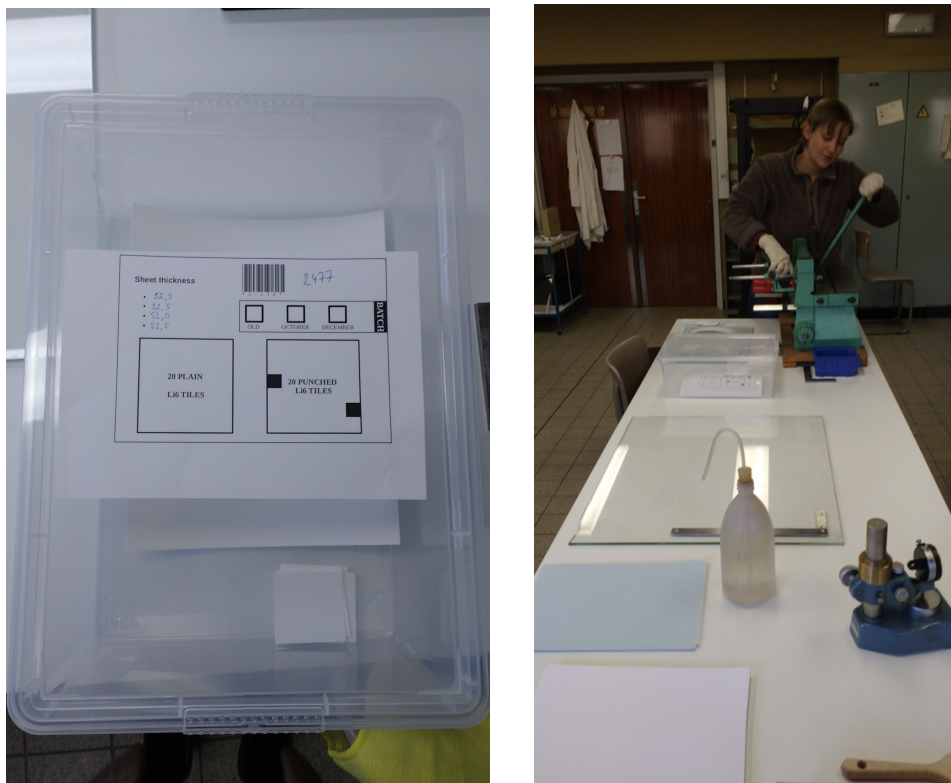


Figure 5.5: Picture showing the storage box for a cut batch of Li with a paper documenting the necessary information (left). The set-up used in the cutting process of the plain Li screens is shown on the right.

The crates that held the cubes were labelled with the information about the original PVT slab. In this way it was possible to keep cubes that originated from the same PVT slab together.

The cubes were placed in a basket to easily transfer them from the washing to the rinsing bath, as shown in figure 5.7. In the first position they were rubbed by hand in de-ionised water with dish-washing detergent. At the latter they were rinsed clean. The cubes were left to dry on microfiber towels. At all times a tag was placed with the cubes to indicate the batch ID and bar-code. This bar-code allowed to track the original PVT slab information. Care was taken to limit the time that cubes were exposed to sunlight. They were therefore rapidly used in the cube wrapping process.



Figure 5.6: Pictures of the wooden tool (left) and the press (right) used to cut the punched Li screens.



Figure 5.7: Pictures showing the washing, rinsing (left) and drying (right) of cubes.

Assembly of the cubes

At the start of cube assembly, Tyvek sheets were prepared by removing loose threads and applying a tag with a bar-code on the closing flap.

The assembly of cubes was always performed by a pair of persons to avoid mistakes: 1 person was referred to as the “database” person, the other as the “wrapping” person.

The database person wore fabric gloves and he/she was the only one touching LiF:Zns screens. The database workstation is shown in figure 5.8

on the left. A dedicated “wrapping” program was available on the desktop to guide the database person through the measurements that needed to be performed. A scale and a bar-code scanner were connected to the program, so that weights and bar-codes were automatically saved to the database.

At the start of each cube procedure, the database person collected a Tyvek wrapping with bar-code, a cube, a punched and a plain Li screen on the transfer tray, as shown in figure 5.8 on the right.



Figure 5.8: Pictures showing the database workstation (left) and the transfer tray plus cube materials (right).

The bar-code of the Tyvek was scanned and served as the main ID of the wrapped cube. Following this, the bar-code of the cube batch was scanned and the cube was weighed. Then the bar-code of the Li batch was scanned and the plain and punched screens were weighed individually. The database person placed the LiF:Zns squares in the correct position on the Tyvek, so the wrapping person did not need to touch them, and transferred the tray to the wrapping table.

The wrapping person wore rubber gloves and never touched the LiF:ZnS. A metal template, shown on the left in figure 5.9, helped to correctly place the cube in the Tyvek wrapper so that the holes in the Tyvek and the grooves in the cube aligned. Once the cube was correctly positioned, the Tyvek wrapper was closed by applying single-sided tape on the 3 closing flaps. The alignment of the holes was checked before transferring the wrapped cube back to the database person.

At this stage the cube was weighed again and the cube information was stored in the database. The cubes were stored in light-tight boxes, shown in figure 5.9 on the right, until they were needed for frame construction.



Figure 5.9: Pictures showing the metal template used to position the cube correctly within the Tyvek (left) and the cube storage box (right).

5.3.3 Frame construction protocol

Preparing the frame

Every new aluminium frame was first installed on a wooden panel for rigidity. The correct orientation of the frame was then identified: the larger side, hosting the electronic box, corresponded to the right-hand side of the frame. The top side of the frame was identified by the configuration of the holes on the right-hand side: these had to be so that the rows were slightly shifted towards the bottom of the gutter, as is indicated in figure 5.10.

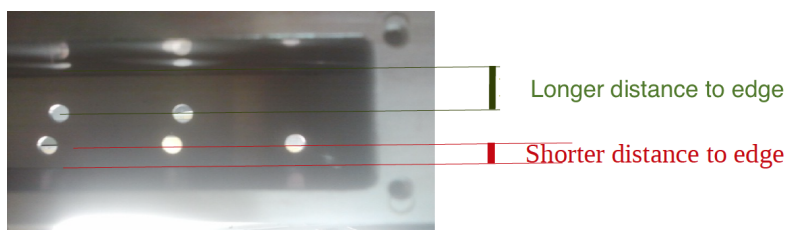


Figure 5.10: Picture showing the correct orientation of the frame for construction based on the position of the holes.

TOP – LEFT – RIGHT – BOTTOM markers were written on the frame to clearly identify the corresponding sides and a red sticker with the frame number was applied on the right side of the frame. The frame was flipped upside down (such that the written labels were not visible) and a large sheet of Tyvek was installed, see figure 5.11, and fixed with black rivets and a strip of single-sided tape covering the edges.



Figure 5.11: Picture showing the back of an aluminium frame equipped with a big Tyvek sheet.

Filling the frame

An A3 summary sheet was used to keep track of the construction date, name of the frame and frame number. This sheet was also be used to keep track of possible remarks during the construction.

After the frame was flipped back into its original position, the white HDPE bars were installed according to their label and hole position. The cleanliness (no machining residuals) and the perfect alignment (Al/HDPE) of each hole was checked. Figure 5.12 shows a corner of a frame where the HDPE bars meet in a step like manner.

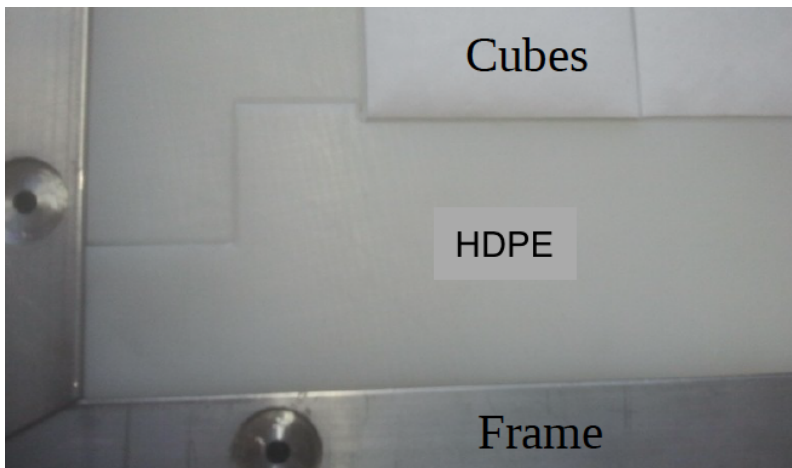


Figure 5.12: Picture of a corner of an Al frame. The HDPE bars and the corner cubes are visible.

There were two types of cubes used in Phase 1, that were almost impossible to differentiate by eye. The outer layer of the detector was equipped with 60 old cubes (SM1 Li sheets), while the central part was made up of 196 new cubes equipped with 2 sheets of new Li. During the filling stage, it was therefore necessary to switch between the two types of cubes.

The program "FillFrame" on a computer guided the user through the procedure of scanning the cubes and saved information on cube positions in the database. Filling the frame started from the bottom-left and ran row after row to the upper-right position. The program gave an error message in case one tried to insert an old cube into a new cube position, or vice versa. The orientation of the cube was checked carefully when positioning it in the frame:

- The bar code had to be visible as in figure 5.13.
- All 4 holes had to be aligned.



Figure 5.13: Picture of the corner cube and how the bar-code was orientated.

Once one row of cubes was filled, it was checked whether one could see through the grooves in all 16 cubes. Any misalignment was investigated and adjusted. The most probable issue was a mis-orientation of the cube, which could easily be fixed by putting the cube into the correct position. Another issue could be that the cube was wrongly wrapped, which could be solved by re-wrapping the cube.

Installation of the cables

Each frame was equipped with 4 sets of cables: 2 long and 2 short. First, the 2 long cables from the electronics box side to their final position were installed. One of the cables connected the upper half of the left side plus the left half of the top side. The other long cable connected the bottom half of the left side plus the left half of the bottom side. Following this, the 2 short cables were installed. One connected the upper half of the right side plus the right half of the top side, the other connected the bottom half of the right side plus the right half of the bottom side.

Installation of the fibres

Fibres were handled with gloves at all times to keep contamination with grease and dirt to a minimum. Fibres were cleaned individually with de-ionised water and a microfiber cloth. The fibre was rubbed softly over its entire length to remove traces of dust and to detect imperfections. Obviously damaged fibres were discarded.

A fibre was then installed in each of the grooves and it was checked whether the shiny edges of the fibre were still clean after installation.

Preparation of the MPPCs

The MPPCs were pre-installed on PCBs (printed circuit boards) that allowed for the connection to the flat cables.

The PCB sheet (1.9u in figure 5.14) was identified by two numbers and a letter (u or l) manually written on each PCB. A PCB was identified by its position on the sheet with one letter (from A to G) and a number (from 00 to 12), printed on each PCB (C 07 in figure 5.14). These identifiers were written in the reference table on the A3 sheet when installing each MPPC on a cable socket (identified by the pair of colours of the flat cable). To avoid mistakes, the colour code and position were strictly followed and checked.

Preparation of the connectors

There were two types of connectors (see figure 5.15) that had the double aim of collecting as much light as possible and fixing the fibre tight to the frame without putting too much mechanical constraint. The MPPC-connector was composed of two separate pieces, the connector and the lid, to ensure perfect contact between the fibre and the MPPC. This was installed at one end of the fibre, indicated on the A3-sheet. A mirror connector was installed at the other end of the fibre, to reflect light back towards the MPPC.

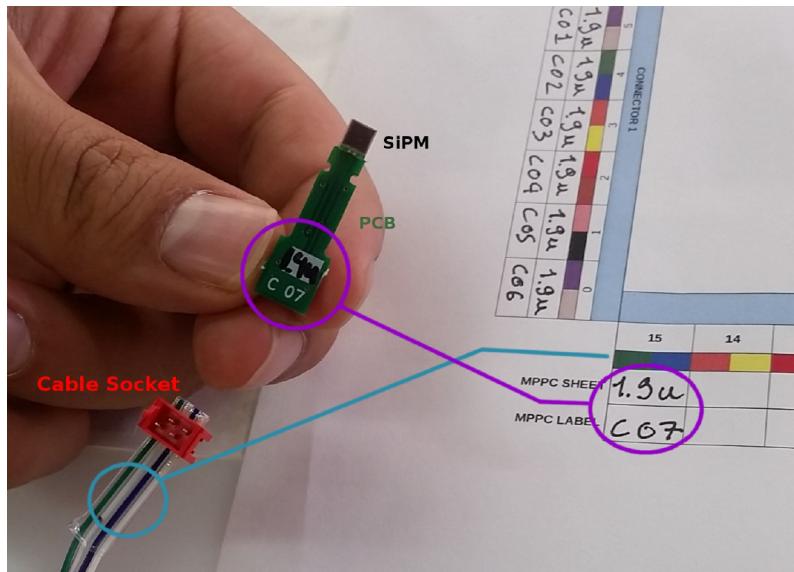


Figure 5.14: Picture of the MPPC on the PCB. An A3 reference sheet was used to keep track of all information about the MPPCs installed on a given frame.

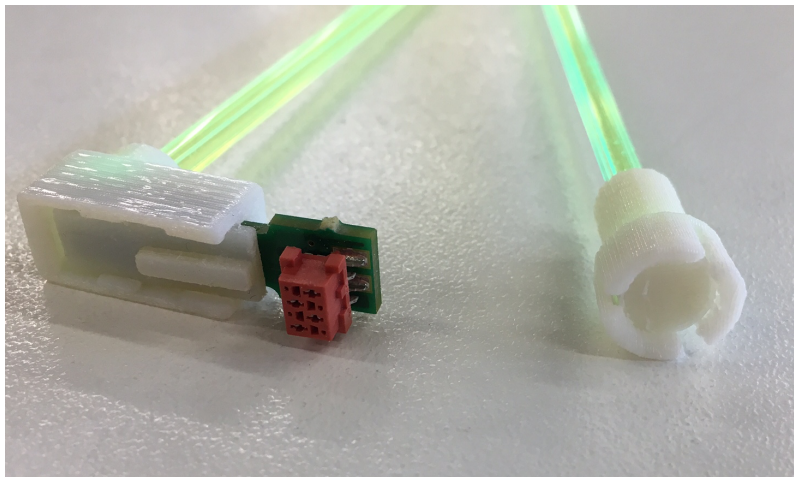


Figure 5.15: Picture of the 2 types of connectors with a fibre inserted. The MPPC connector with MPPC is visible on the left and the mirror connector on the right.

64 MPPC connectors and mirror-connectors were needed per frame. Since the connectors were 3D printed, the size differences could be larger than the tolerances. They were therefore selected and tested before final installation.

The aim of these tests was to discard connectors that did not fit firmly into the frame. For both types:

- A test was performed with an empty frame to ensure the connector roughly fit into the hole. If the connector could be inserted without pressure into the hole, it was discarded.
- The selected connector was checked with a test-fibre to make sure that the fibre could pass through the hole and to remove possible plastic residuals from the inside of the connector.

Once selected, the connectors were placed on the frame in the proximity of their final location.

Installation of the MPPCs

Each MPPC was installed in a connector and it was made sure it fit tightly in the nook. The connector was closed with the lid.

The frame was equipped one side at a time. A tiny drop of optical grease³ was applied in the MPPC connectors with the help of a syringe. The fibre was then inserted in the connector until it touched the MPPC. The grease ensured optimal connection between the MPPC and the fibre. The connector+fibre were pushed back into the frame. A dedicated tool, see figure 5.16, could be used to make a little rotation movement to insert the connector completely into the frame.

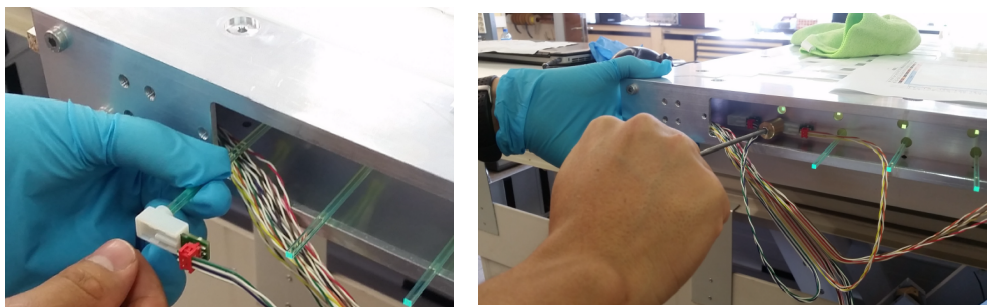


Figure 5.16: Pictures showing the connection between MPPC and fibre (left) and the installation of the connector in the frame with help of the dedicated tool (right).

³BC630 silicon optical grease from Saint-Gobain [87].

Installation of the mirror connectors

The mirror connectors were prepared by adding a little drop of optical grease inside. Figure 5.17 shows the procedure of adding grease to both types of connectors.



Figure 5.17: Application of optical grease with the help of a syringe for the MPPC connector (left) and the mirror connector (right).

The mirror connector was pushed carefully into the frame until a person on the other side of the frame could feel a little push on the opposite MPPC connector. The fibre couldn't be pushed too hard since it was directly in contact with the MPPC.

This procedure was repeated to complete the installation of all connectors at the 4 sides of the frame. At the end, a side of the frame would look like figure 5.18. Acrylic glue was used to secure the position of each connector. A tiny drop was applied with a syringe at the contact between the connector and the frame. A drop was also applied on each MPPC-connector lid to avoid it to slide open.

Completion of the frame

After the installation of all sensors and mirrors, a second Tyvek sheet was installed on the second side of the frame. The sides of the aluminium frame were closed with the appropriate aluminium plates. A second wooden panel was placed on top of the frame and the 2 plates were fastened around the frame with straps. The frame was left flat on a table for at least 1 hour to give the glue time to harden. The frame was then ready for commissioning.

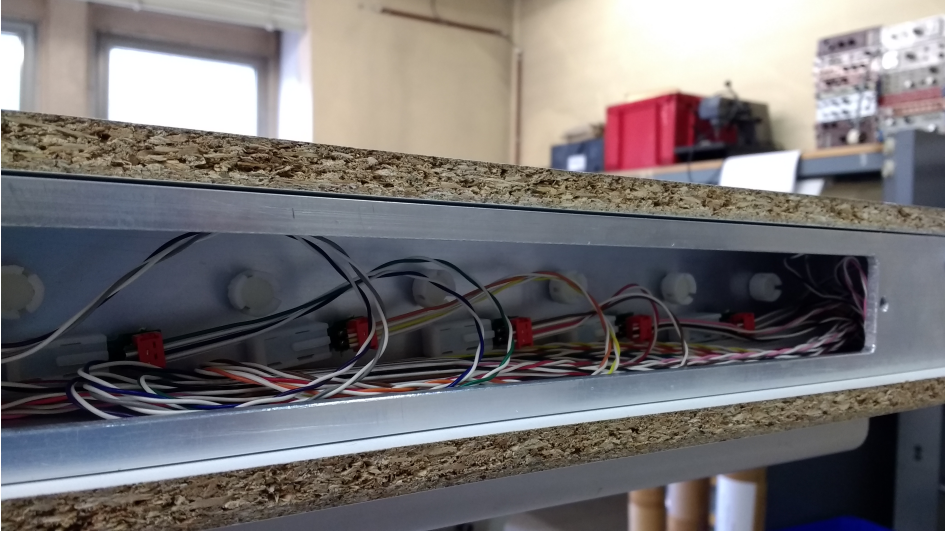


Figure 5.18: Picture showing the top side of a frame with both MPPC and mirror connectors installed.

5.4 Frame commissioning with Calipso

Before the finished frames were inserted in modules, they underwent detailed commissioning in Calipso. This system consists of a robot holding a radioactive source and which is automated to scan the frame in horizontal and vertical directions. By scanning all cubes of a frame with a given source, several checks of the homogeneity and correct MPPC operation could be performed.

Each frame was scanned with at least 2 sources: 1 neutron source and 1 electromagnetic source. When taking data with the EM source, ^{22}Na , the source was positioned in a small box containing a scintillator cube equipped with a small readout fibre and 2 MPPCs. ^{22}Na emits a 1.27 MeV gamma and two 511 keV annihilation gammas. When 1 of these gammas was detected in the cube, it triggered the readout of the frame being commissioned. The set-up is shown in figure 5.19 and allowed to measure the light-yield of each cube. Possible issues such as bad MPPC-fibre contact, loose mirror, swapped cables, and so forth, could be detected by performing an EM source scan.

When taking data with the neutron source, ^{252}Cf , the source was positioned in a special collimator/reflector to increase the neutron interactions in the frame by a factor 4. A further increase was obtained by thermalising the neutrons leaving the source with extra HDPE plates positioned around the

frame. The neutron source set-up can be seen in figure 5.20.



Figure 5.19: Calipso set-up for the EM source measurements. The black box positioned at the middle of the frame holds the EM source.

Performing a neutron scan was particularly useful to investigate the Li screen's efficiency. For example, it was expected to see a lower absolute light-yield at the edges since these cubes were equipped with the "old" Li screens. In case one of the old cubes would, by accident, have been placed in the middle part of the frame, the neutron scan would have been able to identify this error. Figure 5.21 shows the ratio of light-yield for data versus Monte Carlo for a given frame. The left plot shows an obvious discrepancy for 1 of the cubes in the upper right corner. Investigation of the frame showed that this cube was wrapped with only 1 Li screen and it therefore explains the low light-yield. After replacement with a good cube, the new results indicated a uniform light-yield, see figure 5.21 on the right.

The Calipso commissioning of the frames allowed many problems to be identified and fixed. At the end, the light-yield and neutron efficiency of all 12800 cubes were validated and frame-to-frame variations were kept below 10 %. More information can be obtained by contacting L. Manzanillas or V. Pestel from LPC CAEN, who were in charge of the Calipso data and simulation analysis [85].



Figure 5.20: Calipso set-up for the neutron source measurements. The white HDPE moderating plates are visible around the frame. I am adjusting the collimator holding the ^{252}Cf source.

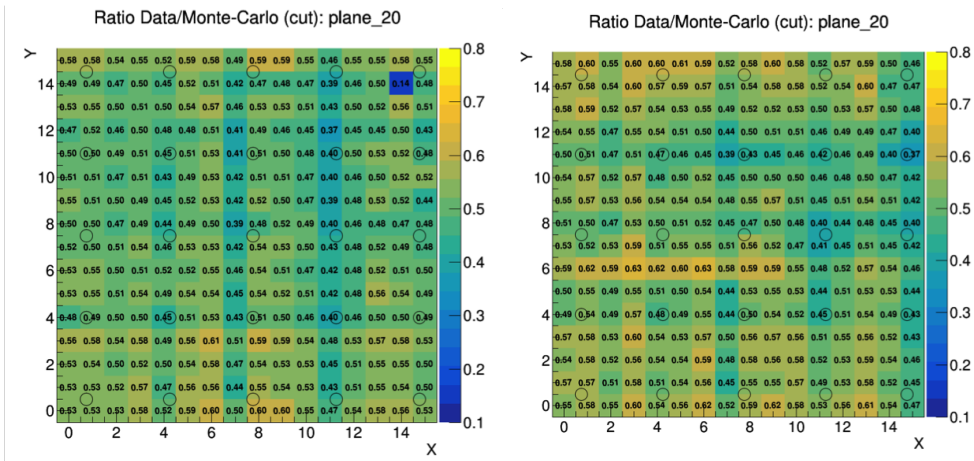


Figure 5.21: Light-yield ratio from data and Monte Carlo measured with the neutron source before (left) and after (right) fixing the frame. Thanks to V. Pestel.

5.5 Conclusion

Phase 1 is the full scale detector built by the SoLid collaboration. Relying on experience and results obtained with the SM1 prototype, several improvements were made. These upgrades included measures to improve the light-yield and to optimise electronics performance, as mentioned in section 5.1.

Due to the enormous amount of manpower and hours needed to build the complete detector, it was very important to ensure an efficient and, above all, consistent way of working. Training and guidance was provided by the Ghent team. Detailed protocols were drawn up for the Li preparation, the preparation and washing of the cubes and the filling of frames. These protocols are written down in section 5.3.

After the construction phase, each frame was individually commissioned with Calipso. This system is designed to move a radioactive source automatically from cube to cube. Thereby measuring the light-yield and neutron efficiency depending on the used source. Runs with a ^{22}Na and a ^{252}Cf source made it possible to identify and rectify many issues in the constructed frames. The errors were corrected by the Ghent team and a homogeneous complete detector was obtained in the end.

4 of the 5 modules were transported together with the container and the cooling system to the BR2 building in October 2017. The 5th module followed in February 2018. After an on-site commissioning period, the proto detector set-up, consisting of the first 4 modules, started stable data taking at the end of November 2017. A reactor-on period from 2 until 12 December and a reactor-off period from 14 until 25 December were recorded with the proto set-up. This data set is used in a commissioning study of the detector and an initial search for IBD signals, the so-called proto-IBD analysis.

Cosmic ray induced back- grounds in Phase 1

6

The initial installation and commissioning of the Phase 1 detector took place with 4 modules. During the data taking with this proto set-up, the back of the water wall, at the side of the container door, was not yet installed. After an on-site commissioning period, data was recorded during a reactor-on period from 2 until 12 December and a reactor-off period from 14 until 25 December. On the 13th of December, a calibration run with an AmBe radioactive neutron source was performed.

The reactor-on and -off data collected with the 4 modules in December are referred to as the proto-IBD data-set. This set is used as a burn sample to make an initial event reconstruction, object identification and to perform an IBD search. The main goal of these studies is the understanding of the Phase 1 detector by the use of rudimentary selections. Later analyses will refine these selections, thereby obtaining better efficiencies or purities depending on the type of analysis.

The work presented in this thesis focuses on muons from cosmic rays and “after-muon” events in the Phase 1 detector. The following sections on triggers, event selection and object identification, will provide the bridge between the waveforms detected by the MPPCs and the analysis performed with reconstructed objects.

The event selection and object identification (ID) is implemented in Saffron2, the SoLid analysis framework, based on Saffron used in the SM1 analyses. The muon ID and initiation of muon tracking in Saffron2 is part of the work in this thesis. Several options can be selected to run Saffron2 over a desired data-set. These options, defined in option files, include a selection of desired analysis algorithms. After Saffron2 processing, further analysis can be performed on the Saffron2 output files, also referred to as output tuples. For this thesis, several standalone C++ codes were written to investigate

“after-muon” events.

Once muons are properly identified they can be used to apply a veto time in IBD searches. Muons create many particles, such as spallation neutrons, which can form a background to the IBD signal. Applying a veto time after a muon, wherein IBD candidates are not reconstructed, is therefore a standard practise to eliminate muon-induced backgrounds. Studies performed within the proto-IBD analysis group use a veto time based on the muon objects reconstructed with the cuts presented in this thesis.

The following section 6.1 discusses the simulations used to compare with data throughout this chapter.

6.1 Cosmic simulations

The cosmic simulations used for the Phase 1 detector are heavily based on the simulations presented in chapter 4, which were used for the SM1 prototype, and follow the same simulation chain. They will therefore only be discussed shortly here.

The Geant4 input files for cosmic particles such as neutrons and muons are again produced with the CosmicGen package. The package has remained the same, only the bounding box properties were adjusted for Phase 1. As was discussed in section 4.1.3, the size of this box is a trade-off between accurate angular and energy distributions and computational time in case the box is chosen too large. The optimal Phase 1 settings were obtained in [88]. The size of the generation surface was chosen to be $300\text{ m} \times 300\text{ m}$ and it is located 30 m above the top of the Phase 1 detector. The bounding box of size $32\text{ m} \times 40\text{ m} \times 32\text{ m}$, is centred around position $(-2, 8, -6.3)$ shown as a red dot in figure 6.1. The origin of the system is located in the middle of the Phase 1 detector plane closest to the reactor.

The Geant4 Phase 1 geometry was developed by I. Pinera and Y. Abreu. To generate cosmic events, the CosmicGen files are used as Geant4 input. IBD events are generated directly in Geant4, so no independent input files are used for these simulations.

After the Geant4 processing, the events are further simulated by a dedicated Phase 1 Read-out simulation [89]. The RO simulation was based on the SM1 version, but in contrast to the SM1 case, the RO simulation for Phase 1 is incorporated in Saffron2. This made the simulation processing much more efficient and structured.

In the next sections some simulations will be used to compare to the proto-IBD data. Both IBD and cosmic muon simulations have been processed with the Geant4 4-module Phase 1 geometry [90]. The Geant4 output files are

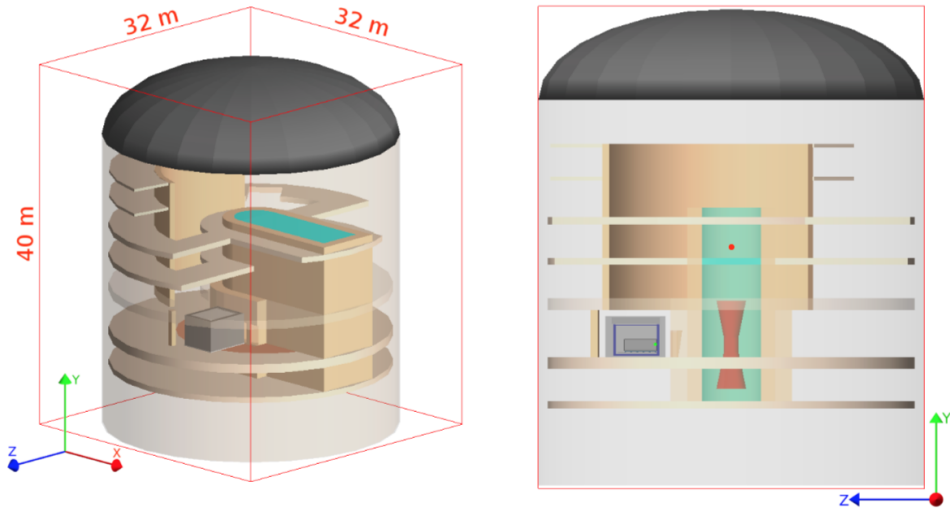


Figure 6.1: Sketches of the Geant4 geometry of the BR2 building and Phase 1 detector, plus the used bounding box. The centre of the box is indicated by a red dot, the origin of the system by a green dot [88].

available, as well as the RO processed versions. For some studies, for example the determination of the muon energy cut (section 6.3.3), it is chosen to propagate only some particles through the RO. An overview of the available simulations can be found in table 6.1, it is also indicated in which section(s) which simulation is used.

6.2 DAQ settings

The data acquisition (DAQ) settings used during data collection were kept constant from November 2017 until March 2018.

The data is collected in runs of 300 seconds at an over-voltage of 1.5 V¹ and only events that cause a trigger are stored. Two different triggers are used: a threshold trigger and a dedicated neutron trigger.

The threshold trigger fires when the waveform exceeds the value of 50 PA. This causes the read-out of 1 block, i.e. 256 waveform samples or 6.4 μs ², in

¹The same over-voltage is applied to all MPPCs on top of their individual breakdown-voltage to amplify the incoming light signals. At a setting of 1.5 V over-voltage, a mean amplification gain of 24 ADC per PA is obtained.

²One sample is thus 25 ns long.

Table 6.1: Available Geant4 and RO simulations. The third column indicates the particles propagated through the RO simulation. The fourth column shows which simulations are used in the following sections.

Type	Geometry	RO propagated	Section
Cosmic muons	4-modules Phase 1	Muons only	6.3.4, 6.4
Cosmic muons	4-modules Phase 1	All	\
Cosmic muons	5-modules Phase 1	All	\
Cosmic neutrons	5-modules Phase 1	All	\
IBD	5-modules Phase 1	IBD prompts only	6.3.4
IBD	5-modules Phase 1	All	6.5.2
BiPo	5-modules Phase 1	All	\

the channel where the peak occurred. This type of trigger is used to record, amongst others, muons and gamma's.

The neutron trigger requires 9 peaks, above a threshold of 1.5 PA, in one 256 samples-long window. This causes a read-out of the entire frame where the trigger occurred, plus, of 3 frames on both sides, from 4 blocks before the trigger up to 4 blocks after the trigger block. The larger position and time read-out make sure that a potential prompt signal associated with the neutron that caused the trigger is recorded as well. This trigger is therefore ideal to select the IBD signals.

Both triggers use a zero-suppression of 1.5 PA to reduce data size. This means that only waveform information above this value is stored and low-level noise is not read out.

The raw waveforms that are recorded by the above-mentioned triggers, are stored in ROOT [91] files which can be used for further analysis.

Figure 6.2 shows an example of a threshold trigger and a neutron trigger in the Phase 1 detector.

6.3 Object reconstruction

The main objects of interest for this thesis are neutrons, muons and other "electromagnetic" signals. To identify these in the recorded waveforms, features such as deposited energy and shape of the signal are used as selection criteria. Some criteria can be adjusted in the Saffron2 options file, so that the output tuples can be tuned according to the required analysis.

The neutron identification is performed on the raw waveforms directly and will be discussed in section 6.3.1. The muon ID, see section 6.3.3, is not

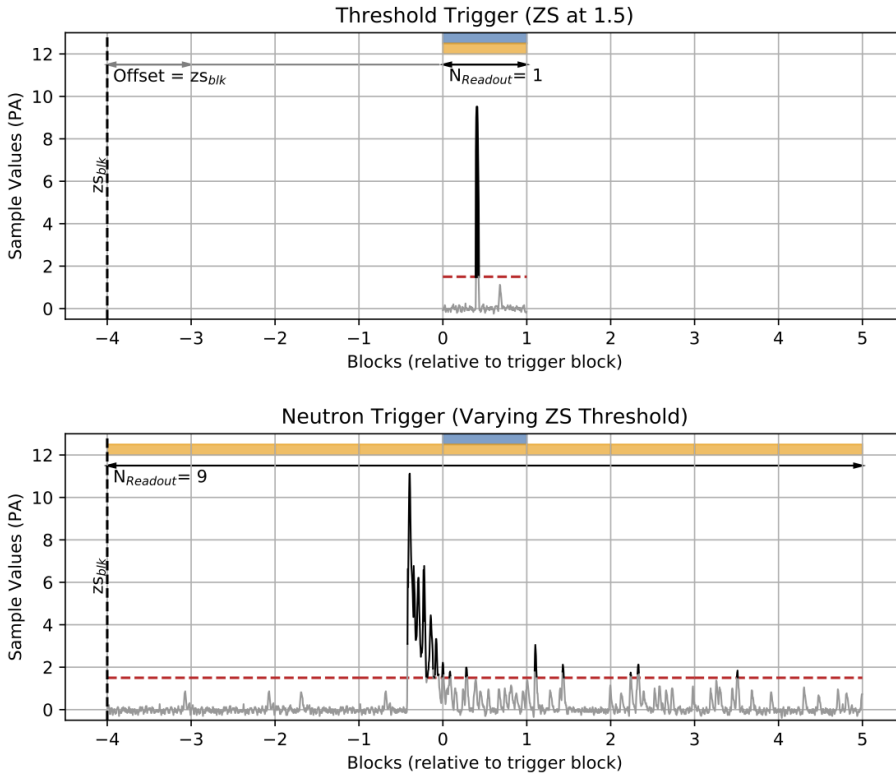


Figure 6.2: Diagram of the threshold trigger (above) and the neutron trigger (below). The blue block indicates the time block following the trigger. The orange blocks indicate the part of the waveform that is stored [92].

performed on raw waveforms but on reconstructed SEvents. These SEvents are time-based clusters of SPeaks found in waveforms. Section 6.3.2 will explain SPeaks and SEvents.

6.3.1 Neutron selection

To select a neutron, the neutron trigger is repeated offline in Saffron2. The so-called SNTrigEmul algorithm scans the raw waveforms and tags channels where 1 block contains more than 9 peaks over a threshold (PoT) of 1.5 PA.

As a neutron is a real physical particle, usually giving rise to a signal in a single cube, it is expected that the 4 channels reading out this cube give a similar signal. However, it is always possible that the neutron is not seen by some of the channels due to geometrical reasons, low energy or a broken channel. The neutron ID in Saffron2 requires at least 2 channels. To select the

cube in which the neutron interaction took place, all possible cubes are reconstructed with the channels containing peaks read out by the neutron trigger. The neutron cube is that one which is found to have the largest amount of peaks over threshold on all 4 channels of the cube combined, within a time window of 512 samples, or 12.8 μ s.

The cubes that are selected in this way, are processed with the SOnlineNeutronID algorithm. This algorithm calculates for each channel of the cube the amplitude, the height of the maximum peak, and integral, surface below the waveform within the range [-9;503] samples from the maximum peak position. The mean value of integral divided by amplitude for the channels forming a cube is called the IonA variable. It is clear from figure 6.3 that there are 2 populations of events present in the selected cubes. The entries with a high IonA value, but a low mean amplitude, are neutrons, while the entries with high amplitudes but low IonA values are electromagnetic signals. To remove the last population, a 2D cut is applied. A straight line with slope 0.005 and intercept 10 followed by a 1D cut at a mean amplitude of 10000 ADC. The entries that survive this cut are tagged as SNeutrons. They are stored in the output tuples with relevant information, such as amplitude, integral, timing and location.

6.3.2 SPeak and SEvent Finding

SPeaks are found by scanning the raw waveforms for samples with an amplitude higher than a pre-set SPeakThreshold. This value can be set in the Saffron2 options file. For the processed files used in the studies presented further on, the value is chosen to be 200 PA. When a sample's amplitude exceeds this threshold and is higher than its neighbouring samples, than it is stored as an SPeak.

After the identification of SPeaks with the SPeakFinder algorithm, these are clustered together in time. All SPeaks within a 80 ns window fall within a so-called SEvent. The SEventFinder algorithm also calculates and stores some specific SEvent parameters, such as the amplitude, which is the sum of all SPeak amplitudes within the event, the mean location based on all hit channels and the number of vertical and horizontal channels.

When SEvents are reconstructed, it is possible to identify actual cubes where physical interactions occurred, with the SCubeFinder algorithm. These cubes are found by requiring SPeaks in at least 3 channels from the cube in question. Studies [93] showed that this requirement alone would select many false "cubes", which do not contain any physical signal, but electronics noise or ambiguous reconstructions. It was found that selecting cubes with an

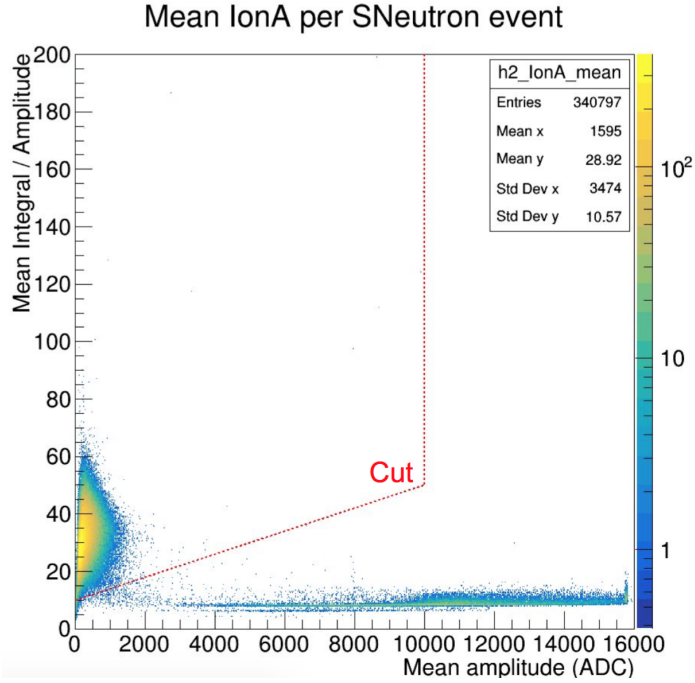


Figure 6.3: Mean amplitude versus mean IonA value for cubes processed by the SOnlineNeutronID algorithm. Both the neutron and EM population are visible. The latter is removed by the cut shown by the red dotted line. Thanks to V. Pestel.

energy asymmetry smaller than 0.7 gives a much purer sample of SCubes. The energy asymmetry, A , is calculated as follows:

$$A = \frac{E_{sum}(H) - E_{sum}(V)}{E_{sum}(H) + E_{sum}(V)} \quad (6.1)$$

where $E_{sum}(H)$ and $E_{sum}(V)$ are the summed amplitudes of all peaks on horizontal H and vertical V channels, respectively.

By applying several cuts to SEvents, it is possible to reconstruct muons³ or other particles that are contained in a certain SEvent. The reconstruction of muons, presented in section 6.3.3, tags certain SEvents as containing a muon and uses cuts based on the channel information of the SPeaks present in the SEvent. Instead of the SPeaks, the SCube information could also be used to identify muon selection criteria, but at the start of the analysis, the SCube

³A conservative study with cosmic muon simulation shows that even a muon that passes through the entire detector would still be confined to a single SEvent in time.

object was not yet mature enough.

6.3.3 Muon identification

The identification of muons interacting in the Phase 1 detector happens within Saffron2 and is based on SEvents. Following the structure of the SM1 analysis, it is chosen to distinguish two different muon objects: the muonCubes and the muonTracks. The latter muons are leaving large tracks through the detector and are easy to identify. They can be used for energy calibration, as will be discussed in section 6.4. This muon object is desired to have a high purity, but can have lower efficiency. The muonCube object on the other hand, is intended to “catch” all other muons and needs to have a higher efficiency. These muons are, for example, passing only through the edge of the detector, thereby only hitting a few channels. Since the muonCube object is much more limited in number of channels, the contamination by other signals, such as gamma’s, is expected to be larger than for the muonTrack object.

An SEvent is tagged as a muonTrack when it meets all of the following criteria:

- SPeaks on at least 8 horizontal channels
- SPeaks on at least 8 vertical channels
- SEvent total amplitude above 5000 ADC (~ 208 PA)

An SEvent can not be tagged as both a muonTrack and a muonCube, these objects are mutually exclusive. A muonCube is found when an SEvent meets the following requirements:

- Not yet identified as a muonTrack
- SPeaks on at least 2 horizontal channels
- SPeaks on at least 2 vertical channels
- SEvent total amplitude above 2000 ADC (~ 83 PA)
- At least 1 channel in the event is located on the edge of the detector

The last statement is met when a vertical channel is located at the outer x values (0 or 15), a horizontal channel is located at the outer y values (0 or 15) or, when either a horizontal or vertical channel is hit in one of the outer planes ($z=0$ or $z=39$).

Figures 6.4 and 6.5 show a muonTrack and a muonCube event, respectively, in the Phase 1 detector. The top row of plots indicates the peak intensity in ADC in the vertical channels, detected by the bottom and the top MPPCs, respectively in the left and right figure. The bottom row of plots

indicates the peaks in the horizontal channels, detected by the MPPCs on the left (left figure) and right (right figure) of the frames. Figure 6.4 shows a muonTrack entering the detector from above ($y=16, z=23, x=12$) and escaping the detector at the bottom ($y=0, z=35, x=12$) after leaving a visible track through the detector. Figure 6.5 shows a muonCube clipping the bottom part of the detector.

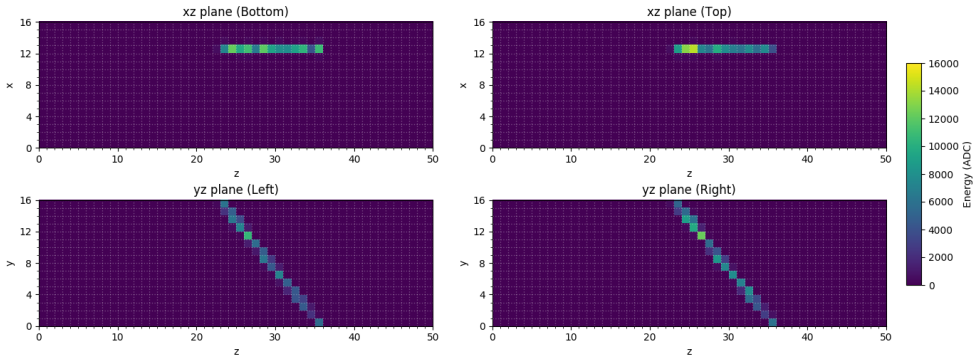


Figure 6.4: MuonTrack event in the Phase 1 detector.

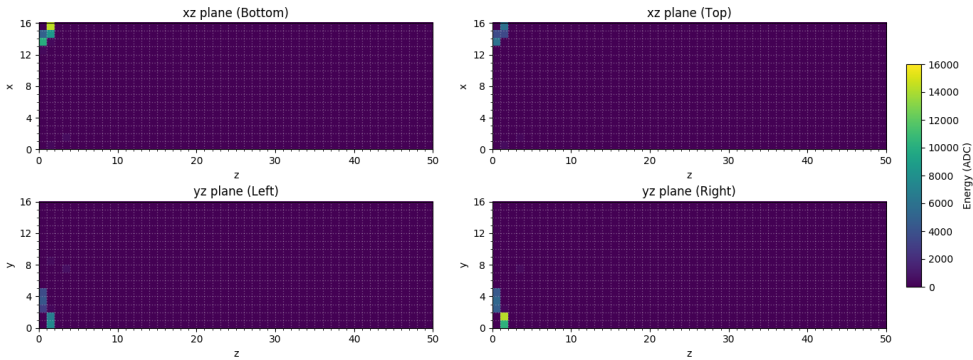


Figure 6.5: MuonCube event in the Phase 1 detector.

6.3.4 Muon efficiency

Processing cosmic muon simulation files with Saffron 2 makes it possible to know exactly how many simulated muons get tagged as a muonCube or muonTrack. It shows that the muon tagging efficiency is rather low at $[88.3 \pm 1.3] \%$. This implies that many muons are not tagged as such, which

makes the muon veto less effective as a tool to reject backgrounds. On the other hand, simulations of IBD prompts indicate that only $[0.36 \pm 0.04]$ % of the prompts gets tagged as a muon object. The contamination of the muon sample by IBD prompts is thus very low.

To improve the muon tagging efficiency, the simulated events that are not identified as a muonCube or a muonTrack are investigated. Figures 6.6 and 6.7 indicate the number of vertical and horizontal channels, respectively, that contain SPeaks within an un-tagged event as a function of the SEvent energy. It is clear that some high energy muons remain. Figure 6.8 shows the number of horizontal channels as a function of the amount of vertical channels for the un-tagged muons. This plot shows that some vertical muon tracks, with a high number of horizontal channels, escape the current muon selection. These tracks are not selected as a muonTrack since they do not meet the requirement of minimum 8 vertical channels. On the other hand, they are mainly not selected as a muonCube because they do not have a hit edge channel. This can be caused due to the high SPeakThreshold, of 200 ADC, used in the SPeak selection criteria. A muon will always enter by passing an edge channel, but if the deposited energy in this channel is rather low, the SPeak will not be reconstructed.

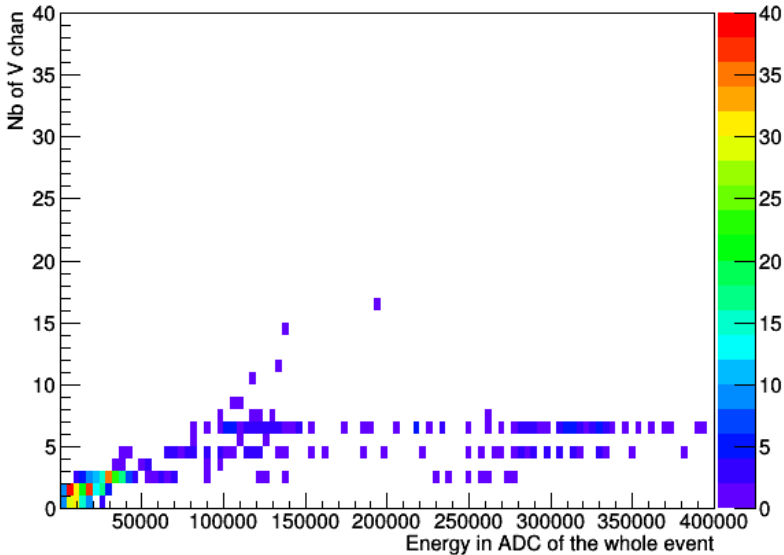


Figure 6.6: Number of vertical (V) channels as a function of the SEvent energy for simulated muons not tagged as muonCube or muonTrack.

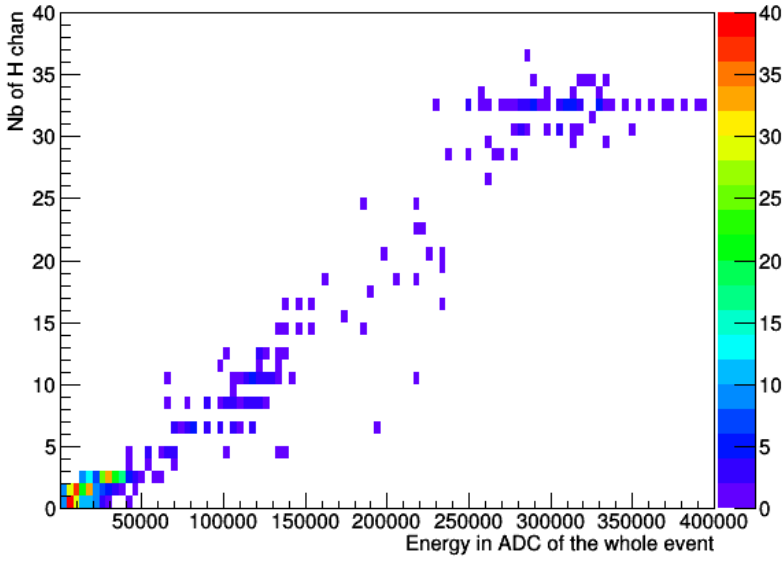


Figure 6.7: Number of horizontal (H) channels as a function of the SEvent energy for simulated muons not tagged as muonCube or muonTrack.

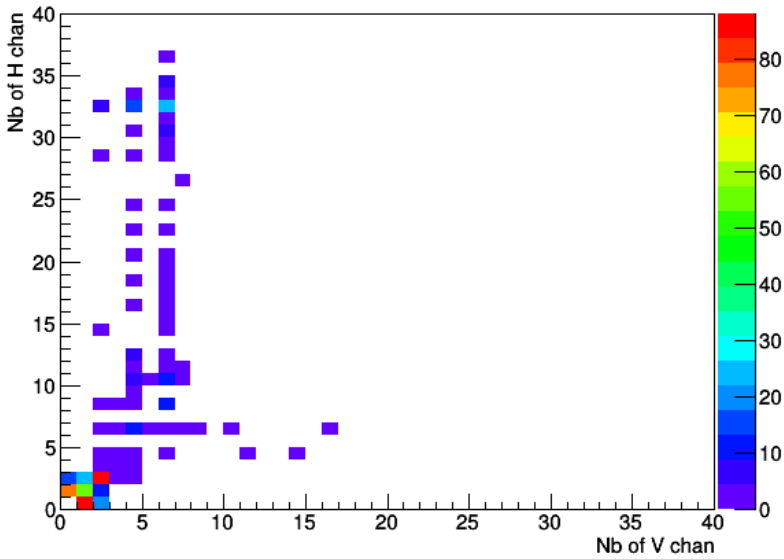


Figure 6.8: Number of horizontal (H) versus vertical (V) channels for simulated muons not tagged as muonCube or muonTrack.

At the time of this study, all December data files were already processed with the proto-IBD analysis framework. An improvement of the muon veto therefore needs to be applied offline as re-processing the data would be too time-consuming.

It was investigated that by tagging all SEvents with an SCube located at the edge and with that SCube energy above 4000 ADC as a muonExtra object, the muon tagging efficiency rises to $[95.4 \pm 1.4] \%$ ⁴. Figures 6.9 and 6.10 show the number of vertical and horizontal channels, respectively, that contain SPEaks as a function of the SEvent energy for simulated muons that are not tagged as a muonCube, a muonTrack or a muonExtra object. Figure 6.11 gives the number of horizontal channels as a function of the amount of vertical channels for the un-tagged simulated muons.

The figures indicate that all muons leaving a clear track in the Phase1 detector are now properly identified. From figure 6.11 it is clear that most remaining un-tagged muons only contain peaks in either only 1 horizontal or only 1 vertical channel. It is likely that this effect is caused again by the relatively high value of the SPEakThreshold. There are very few un-tagged events that still contain a full cube, with 2 horizontal and 2 vertical channels. In these cases, the cube is located in the inner volume of the detector and not on the edge. The deposited energy of the muon while entering via an edge cube, was in these cases too low to give reconstructed SPEaks in this cube.

The proto-IBD analysis by D. Boursette and S. Vercaemer uses a veto time of $750 \mu\text{s}$ ⁵ after a muon wherein no IBD candidates are reconstructed. A study by S. Vercaemer shows that this induces a dead-time of $[14.3 \pm 0.1] \%$ when using the muonTrack and muonCube reconstructed objects [94]. When adding the muonExtra object, the dead-time increases slightly to $[16.2 \pm 0.1] \%$, which is a good trade-off for a 7 % increase in efficiency. Further studies will focus on improving the muon tagging efficiency within Saffron2 and will explore the possibility to reduce the muon veto time to lower the dead-time.

6.3.5 Muon rates and environmental correlations

Investigating the muon rate is interesting to monitor the stability of the detector. As was done for SM1 (see section 4.3) the rate of muons is obtained by

⁴Simulation of IBD prompts indicates that the contamination of the muon sample by IBD prompts does not increase noticeably when adding the muonExtra object selection.

⁵This veto time is arbitrarily chosen to be approximately 10 times the value of the neutron capture time, which will be derived later in this chapter. The value will be optimised in future studies.

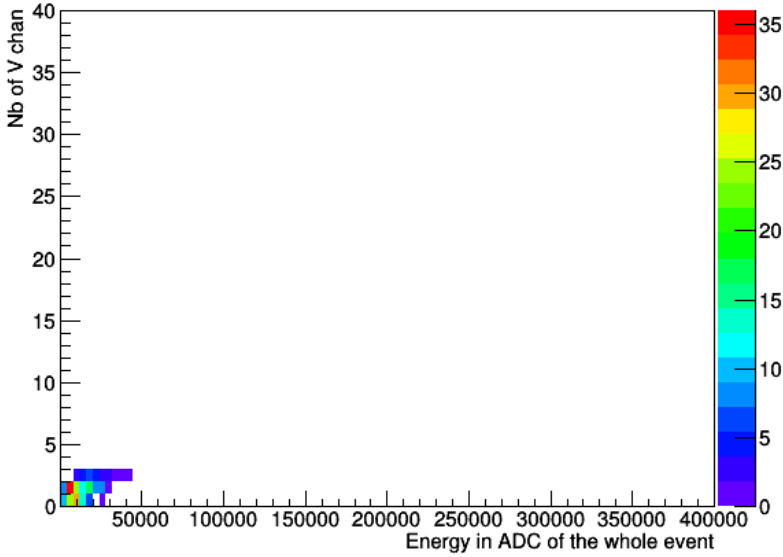


Figure 6.9: Number of vertical (V) channels as a function of the SEvent energy for simulated muons not tagged as muonCube, muonTrack or with the extra cut.

plotting the time difference between subsequent muons and fitting the distribution with an exponential. Figures 6.12 and 6.13 show the muonTrack and muonCube rate for the data collected on the 18th of December during reactor-off time. The rate of muonTrack objects is $[204.46 \pm 0.06 \text{ (stat)} \pm 2.38 \text{ (syst)}]$ Hz and the rate of muonCube objects is $[36.78 \pm 0.05 \text{ (stat)} \pm 0.54 \text{ (syst)}]$ Hz. Both systematic errors were obtained by repeating the fit while excluding the first bin, and taking the difference in rate as a 1σ systematic error.

From simulation, a total muon rate of $[213 \pm 3]$ Hz is expected, significantly lower than the $[241 \pm 3]$ Hz found in data, which is not corrected for the muon reconstruction efficiency. This can have several causes: a low purity of the muonTrack or muonCube object, or an issue in the simulated rate. Further on in this section it will be shown that the muonTrack and muonCube objects are expected to be quite pure. It is therefore suspected that the approximations made in CosmicGen, i.e. the settings of the bounding box, to reduce computational time, explained in section 6.1, alter slightly the simulated rate and that absolute rates should not be compared to simulation directly.

Analysing the distribution of muon interactions over the detector planes is an easy way to detect issues with the detector. Figure 6.14 shows a relatively

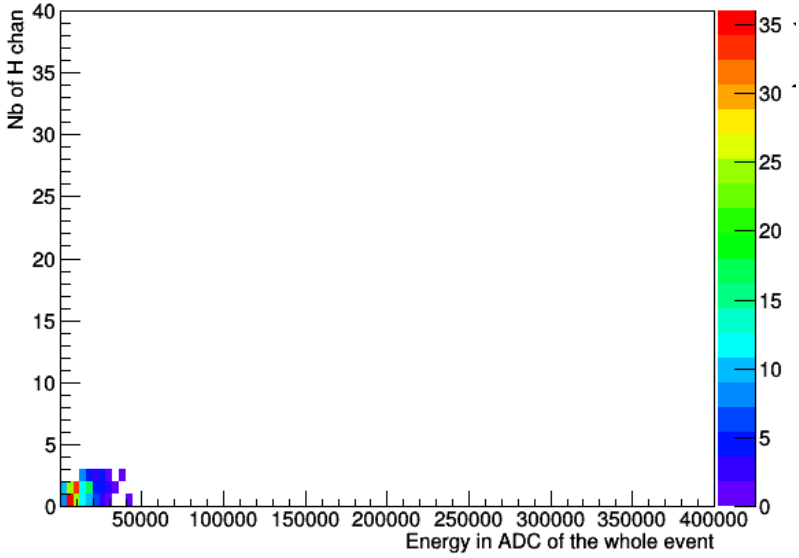


Figure 6.10: Number of horizontal (H) channels as a function of the SEvent energy for simulated muons not tagged as muonCube, muonTrack or with the extra cut.

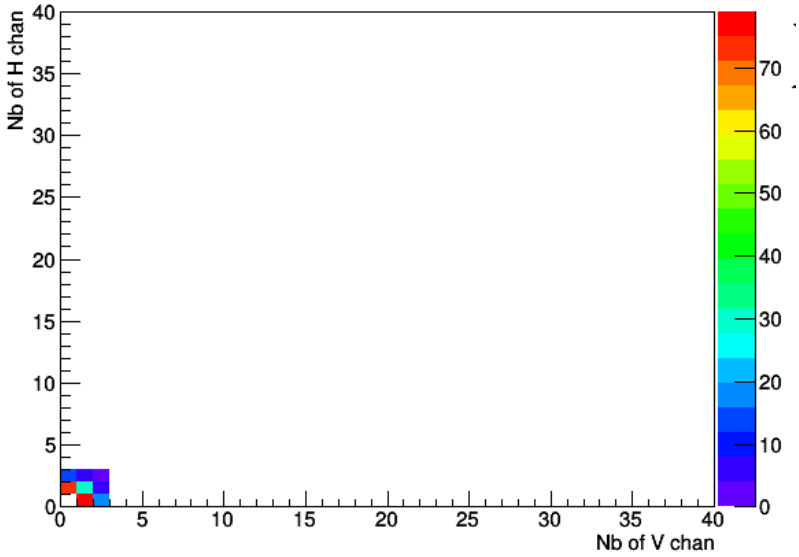


Figure 6.11: Number of horizontal (H) versus vertical (V) channels for simulated muons not tagged as muonCube, muonTrack or with the extra cut.

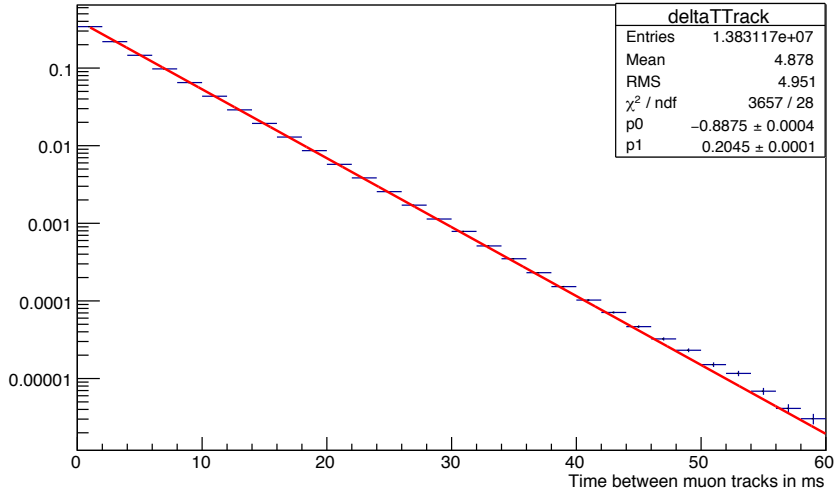


Figure 6.12: Determination of the muonTrack rate in Phase 1. The fit provides a value of $R_\mu = [204.46 \pm 0.06 \text{ (stat)} \pm 2.38 \text{ (syst)}]$ Hz.

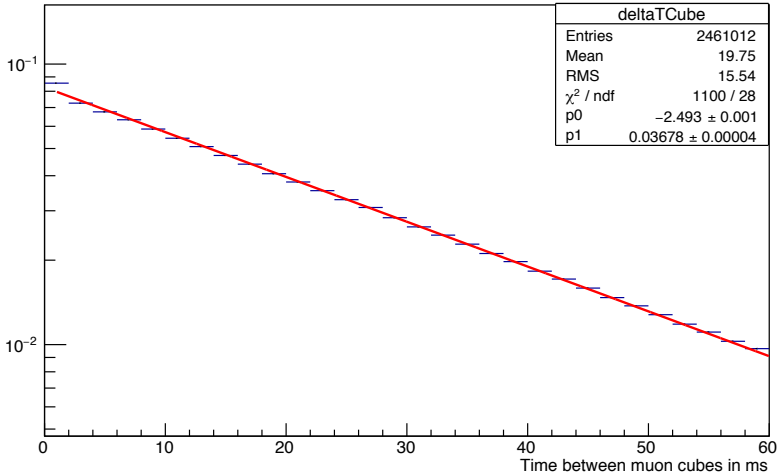


Figure 6.13: Determination of the muonCube rate in Phase 1. The fit provides a value of $R_\mu = [36.78 \pm 0.05 \text{ (stat)} \pm 0.54 \text{ (syst)}]$ Hz.

uniform distribution of muon interactions over the detector length, although some features can be seen. Plane 10 shows a dip in muon interactions; this is caused by several masked channels. An increasing trend towards higher z-values is observed due to the shielding from the reactor vessel. The edges of the detector observe fewer muons, which is expected due to geometrical reasons ⁶.

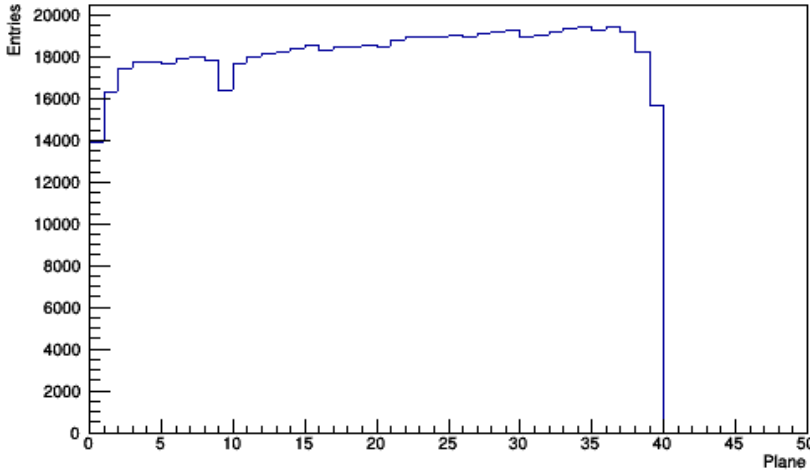


Figure 6.14: Distribution of muonCube and muonTrack interactions over the detector planes.

It is known that the rate of muons reaching the earth and interacting in the detector is inversely correlated to the atmospheric density at altitude. This can be understood as follows: the higher the density, the more muons will interact and lose energy. Therefore they are less likely to be able to reach the ground.

The atmospheric density is determined by both the temperature and pressure at altitude. As no information at altitude is available for the BR2 location, it is opted to investigate the correlations with ambient temperature and pressure at ground level. These data are available in the BIDASSE database of the BR2 reactor.

Figure 6.15 shows the correlation between the muon rate, from both muonCubes and muonTracks, and outside temperature (top left) and outside pressure (top right). No relation is determined between the temperature and the muon rate, as the temperature fluctuations on the ground do not follow the

⁶Muons that hit the detector at the edges are less likely to be reconstructed than tracks passing through the entire detector.

same trends as the temperature at altitude. The changes in pressure (P) on the other hand, do represent similar changes in the pressure at altitude and a clear inverse correlation can be seen with the muon rate. The relation can be parametrised by: $\text{rate (Hz)} = -0.31 [\pm 0.01] P \text{ (hPa)} + 564.67 [\pm 5.64]$. With this fit, the muon rate can be corrected for the pressure so that a constant muon rate is obtained. The corrected muon rate is indicated by the green dots in the lower plot. It can be seen that this shows, indeed, quite stable behaviour. Figures 6.16 and 6.17 show, respectively, the distribution of muon rates before and after correction to the mean pressure (1020 hPa). The RMS (root mean square) of the distribution is seen to drop from 5.22 Hz to 1.46 Hz and is therefore a good indication that the pressure corrected muon rate is stable.

By investigating the correlation between muon rate and pressure for reactor-off and reactor-on data separately, it is possible to obtain an indication of the muon object purity. The muon rate is not expected to change between reactor-on and reactor-off time, but other particle rates, for example gamma's, neutrons, prompts, etc will. Therefore, if a different correlation would be observed between reactor-on and -off, this would indicate a contamination of the muon objects.

The relation between muon rate and pressure for reactor-off data is: $\text{rate (Hz)} = -0.33 [\pm 0.01] P \text{ (hPa)} + 585.25 [\pm 65.12]$ and for reactor-on data: $\text{rate (Hz)} = -0.31 [\pm 0.01] P \text{ (hPa)} + 561.32 [\pm 55.89]$. The parametrisations are consistent with each other and therefore strengthen the trust in the purity of the muon objects.

6.4 Muon tracking

Muons are high energy particles and often leave distinct tracks in the detector as they loose energy proportional to the matter they pass. In SM1 the muonTrack objects were therefore used as a means to calibrate the prototype on a channel-to-channel basis [72]. The approach that is followed in such a calibration is the following:

- Identify muonTrack objects.
- Select a pure sample of muonTracks to which a straight line can be fitted.
- Select those muonTracks that at a certain row (/column) only hit 1 cube (in the following these cubes are referred to as "isolated"). In this way it is certain that the energy detected by vertical (/horizontal) channel comes from the energy deposit in that one cube. This energy is called

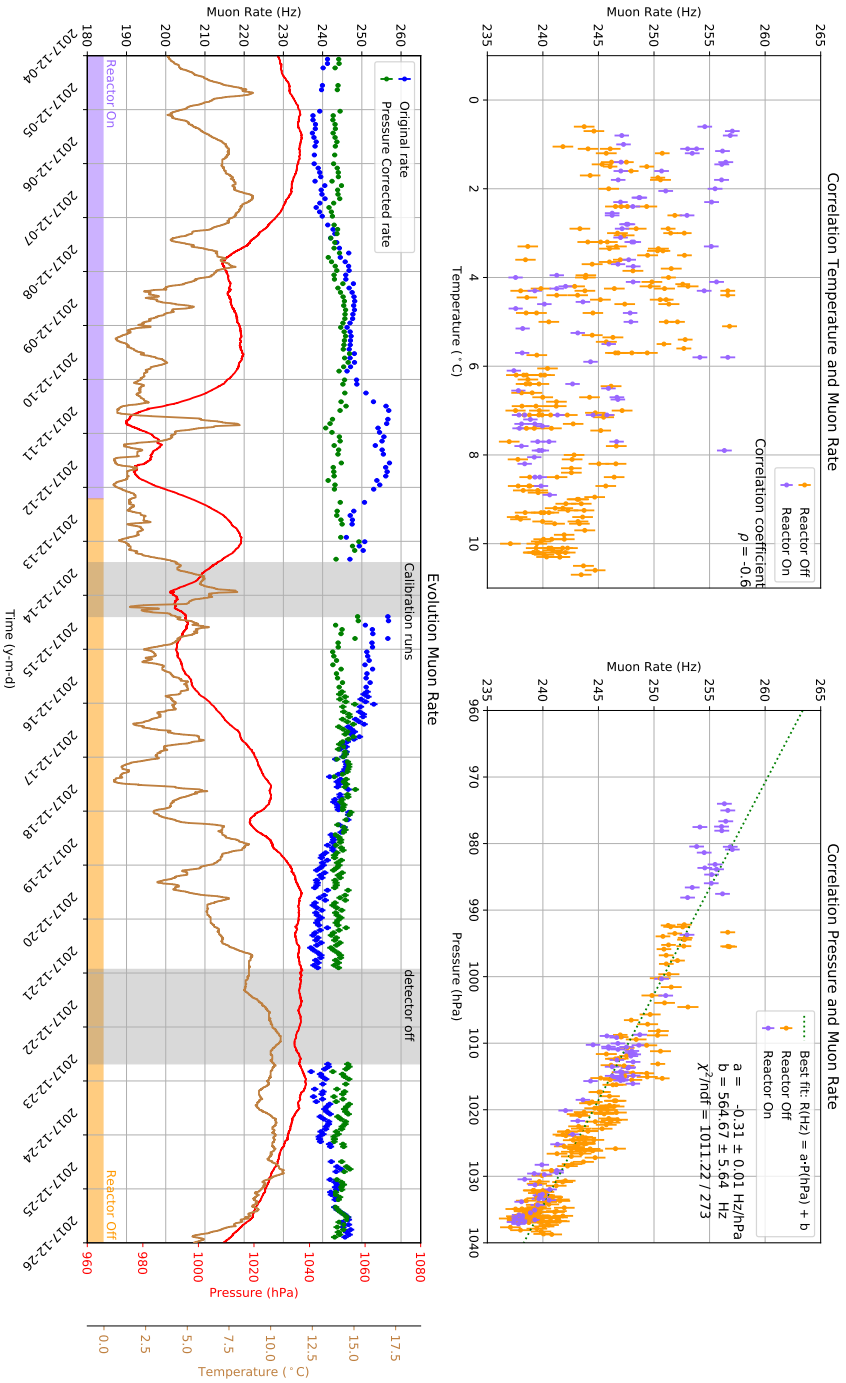


Figure 6.15: Correlation of environmental parameters, outside temperature on the top right and outside pressure on the top left, with the muon rate (muonCubes and muonTracks). The lower plot shows the muon rate over time in blue. The green dots show the muon rate corrected for outside pressure (shown in red) [95].

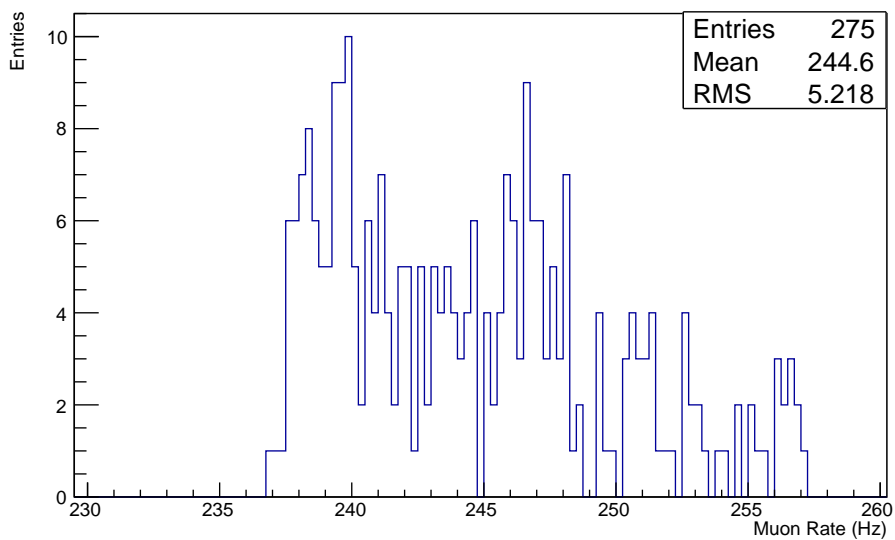


Figure 6.16: Muon rate distribution before pressure correction.

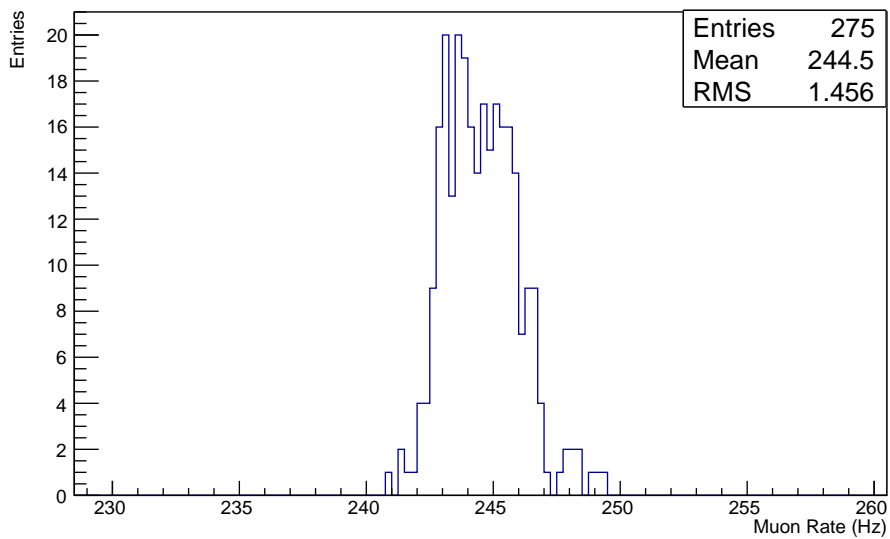


Figure 6.17: Muon rate distribution after pressure correction.

dE and is expressed in ADC.

- Calculate with the fitted line the pathlength, dx , of the muonTrack in the isolated cube.
- Now the value of dE/dx can be calculated, the deposited energy per unit pathlength.
- Simulation provides a dE/dx value for cosmic muons expressed in MeV per unit pathlength.
- Comparing simulation and data provides a conversion between MeV and ADC.

Section 6.3.3 discussed how the muonTrack objects are defined. The overall muonTrack requirements (at least 8 horizontal and at least 8 vertical channels) make sure that all tracks have enough channels to be able to fit the track.

The fit is performed within Saffron2 and independently for the vertical and for the horizontal channels in an SEvent tagged as muonTrack. No weight is given to the energy deposited in the channels. Figure 6.18 shows a fitted muon. Based on the fit, it is then possible to search for rows/columns with only 1 hit cube and to calculate the pathlength in that cube. The distribution of dE vs dx for data is shown in figure 6.19. It is clear that there is a linear behaviour, as expected. However, there is also a large spread.

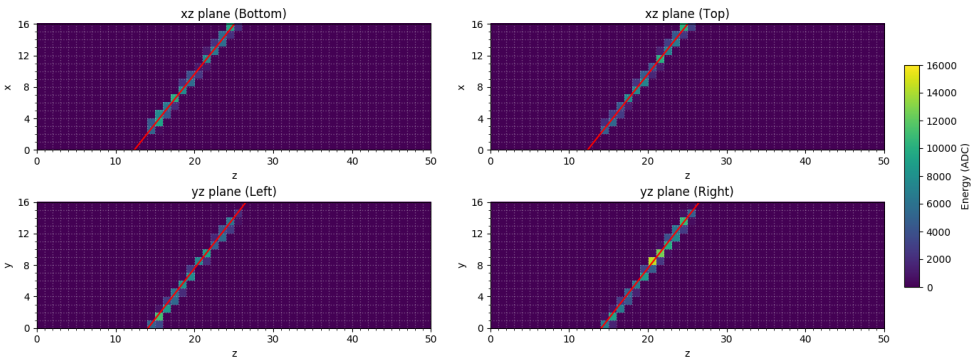


Figure 6.18: Fit to a muonTrack object for the horizontal channels (top) and vertical channels (bottom) separately.

Figure 6.20 shows the dE/dx distribution for values of dx between 5.5 cm and 6 cm. To obtain a value of dE/dx to compare with simulation, one could fit the distribution with a convolution of a Gaussian and a Landau distribution⁷. However, it will be shown further on that the tracking, and

⁷In the case of a perfectly reconstructed energy, the dE/dx distribution can be described

thus the pathlength calculation, needs to be improved before a precise value of dE/dx can be obtained. For the moment, 1060 ADC/cm, the mean of the distribution, can be used as a dE/dx estimation. A similar study with simulated muons provides a dE/dx value of 1.8 MeV/cm, thus leading to a conversion factor of around 588 ADC/MeV.

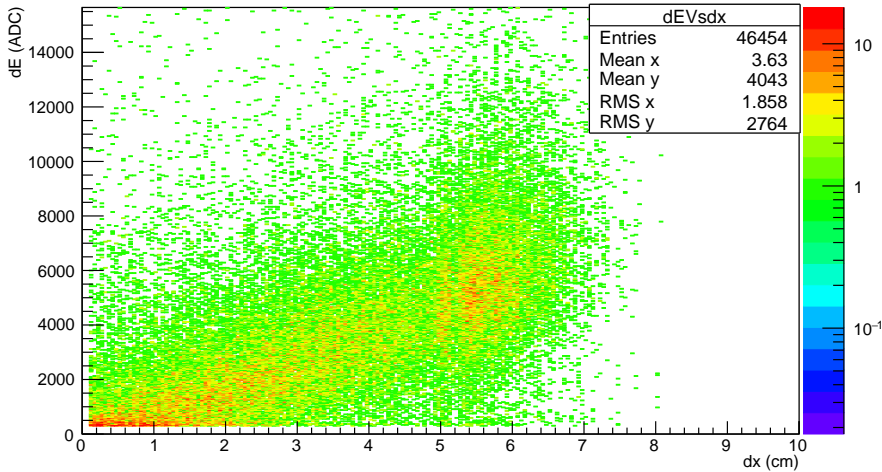


Figure 6.19: Distribution of dE versus dx for isolated cubes in a muonTrack object.

Comparison with simulation shows that often the pathlength is overestimated. This can be seen in figure 6.21, which shows the difference between the reconstructed pathlength obtained with the fit and the simulated pathlength. The reason for this overestimation is the naive way of fitting the track. It does not take into account a weighting according to energy deposited in a certain channel. Another issue occurs when an SEvent contains a noise peak as well as a muonTrack. In this case the noise will pull the fitted track away from the actual muon. An example is shown in figure 6.22.

In the future, the fit to the muonTrack will be improved by using a weight according to the energy and by removing peaks that are not part of the actual track. The properly fitted muonTracks can then be used to perform a detector calibration based on muons.

by a Landau distribution. However, the convolution with the Gaussian distribution is needed to take the energy smearing into account.

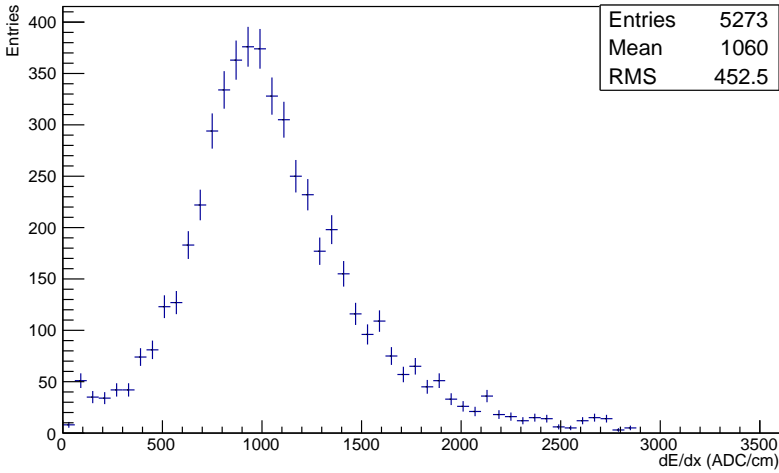


Figure 6.20: Distribution of dE/dx for values of dx between 5.5 and 6 cm.

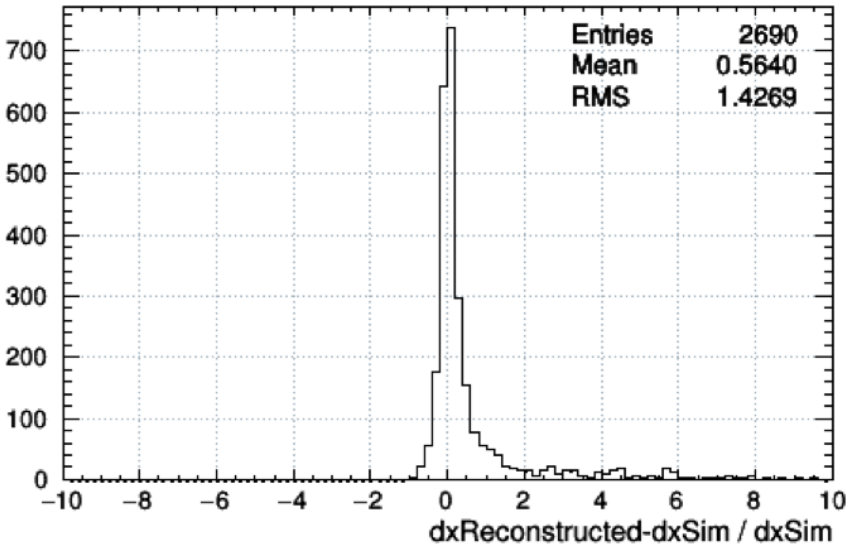


Figure 6.21: Distribution of the difference between the reconstructed pathlength obtained with the fit and the simulated pathlength.

6.5 “After-muon” events

After the identification of basic reconstructed objects, such as muons and neutrons, it is possible to investigate coincidences occurring between these

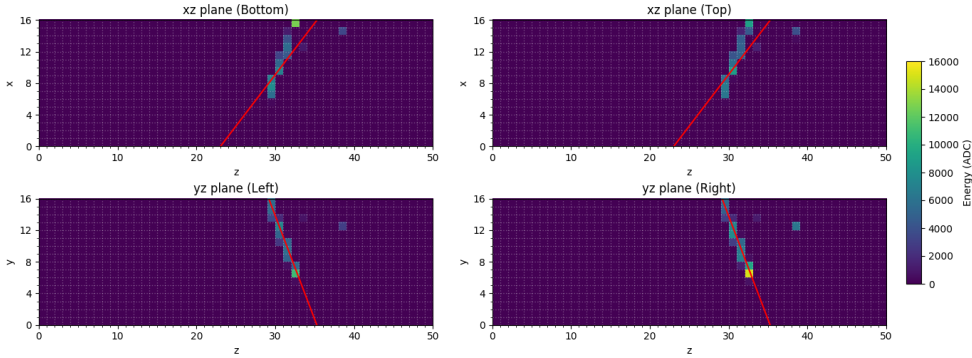


Figure 6.22: Fit to a muonTrack object for the horizontal channels (top) and vertical channels (bottom) separately. A noise peak in the SEvent pulls the fit to the horizontal channels away from the track.

objects in the Phase 1 detector. This is necessary to understand the basic behaviour of the detector. To this end, Saffron2 output tuples are generated with a time-sorted tree of SEvents, with muon tags, and neutron objects.

In this thesis two types of “after-muon” events are investigated, Michel electrons and spallation neutrons, with the on-time and off-time window approach explained in section 4.3. These studies will be discussed in the next sections. The other members of the proto-IBD analysis group investigated coincidences between neutrons and prompts in an initial IBD search.

6.5.1 Michel electrons

When a muon stops after losing its energy, it can decay, thereby creating a so-called Michel electron (ME) and two neutrinos. Identifying the decayed muon and the following ME in the Phase 1 detector allows to determine the muon decay time. As was done for SM1, the Michel electron study is performed with an on-time window, from $1 \mu\text{s}$ to $25 \mu\text{s}$, and an off-time window of the same length but shifted 1 ms later, as shown in figure 6.23.

In the proto-analysis, only muons and neutrons are reconstructed within Saffron2. An electron needs to be identified offline. To tag a Michel electron, an SEvent needs to meet the following conditions:

- The SEvent must be at least 3 blocks (1 block is 256 samples) later in time than the last neutron in the time-sorted tree. Otherwise the SEvent might contain part of the neutron tail.
- The SEvent must contain at least 4 channels.
- The total amplitude of the SEvent must be larger than 5000 ADC.



Figure 6.23: Schematic representation of the on-time and off-time window approach used for the study of Michel electrons.

No cut is applied to require that the muon stops inside the detector, since it is not straightforward to implement as long as the muon objects are not defined on an SCube basis. In any case, it is not necessary for the following since the analysis uses an on- and off-time window approach.

After the ID of Michel electron candidates, the on- and off-time window distributions of the time between the muon and ME can be filled. From these, the muon decay time can be obtained in 2 ways, as was the case in the SM1 analysis. The first method fits the on-time window with an exponential plus a constant, thereby assuming a flat background, as shown in figure 6.24. The decay time found with the fit is $\tau_\mu = [2.07 \pm 0.01 \text{ (stat)} \pm 0.07 \text{ (syst)}] \mu\text{s}$, to be compared with the value quoted in literature of $[2.1969811 \pm 0.0000022] \mu\text{s}$ [82]. The off-time window is also plotted in this figure to show that the flat-background approximation is valid.

The second approach to determine the muon decay time, is to subtract the off-time window from the on-time window and to fit the subtracted distribution with a simple exponential. The fit is shown in figure 6.25 and gives a value of $\tau_\mu = [2.13 \pm 0.01 \text{ (stat)} \pm 0.05 \text{ (syst)}] \mu\text{s}$. It can be seen that this fit has a relatively high χ^2 value. This is caused by the subtracted bins with a negative value, while the tail of the fit is forced to return to zero.

The systematic error on the muon decay, for both methods, is obtained by repeating the fit while excluding the first bin, and taking the difference in τ_μ as a 1σ systematic error.

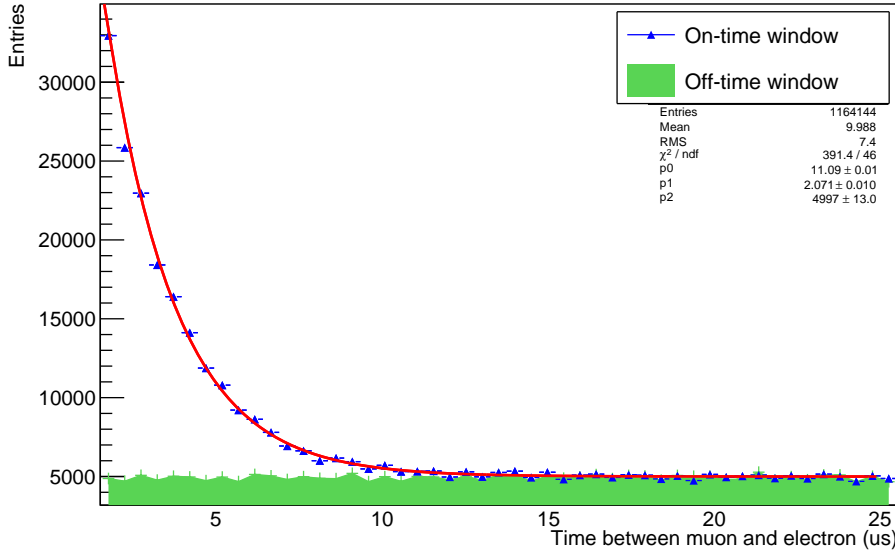


Figure 6.24: Determination of the muon decay time by fitting an exponential plus a constant to the on-time window. A decay time of $\tau_\mu = [2.07 \pm 0.01 \text{ (stat)} \pm 0.07 \text{ (syst)}] \mu\text{s}$ is obtained. The off-time window is plotted in green.

The values of the muon decay time obtained with both methods are compatible with the value quoted in the PDG within 2σ . This shows that the basic properties of our detector are well understood. Moreover, in parallel to what was mentioned in section 4.3, it also provides proof that the Phase 1 detector is capable of detecting prompt-delayed signals, as is the goal in IBD searches.

By subtracting the amount of entries in the on-time and off-time window, it is found that around $[1.705 \pm 0.006] \%$ of the muons decay inside the detector and produce a detected Michel electron. This corresponds to a rate of $[4.11 \pm 0.02] \text{ Hz}$ of observed Michel electrons in the Phase 1 detector.

Investigating several parameters can provide more insights into the muon decay. Figure 6.26 shows the closest distance between the muon and the ME for both the on-time and off-time window, while figure 6.27 shows the off-time subtracted distribution. The excess at small distances shows that the Michel electron will interact closely to the decay location of the muon. Figure 6.28 shows an example of a muon decay in the Phase 1 detector and the following interaction of the Michel electron close to the muon track.

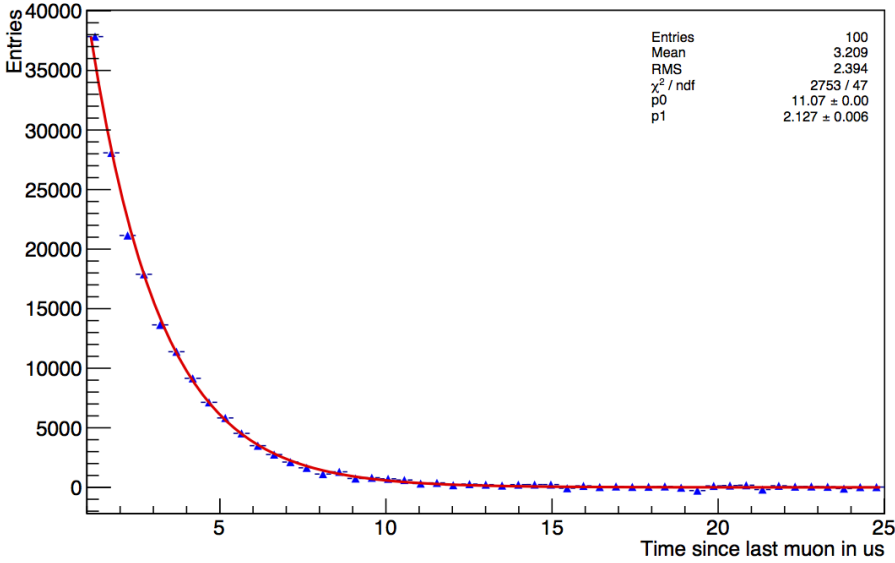


Figure 6.25: Determination of the muon decay time by fitting an exponential to the off-time subtracted time distribution. A decay time of $\tau_\mu = [2.13 \pm 0.01 \text{ (stat)} \pm 0.05 \text{ (syst)}] \mu\text{s}$ is obtained.

Figure 6.26 shows a clear increase at larger distances for the off-time window. This can not be explained by any physical effect, it is therefore expected that a scaling issue is causing the difference in distribution tails between the on- and off-time window. The linear behaviour between 80 and 190 cm in figure 6.27 provides proof that a scaling issue is indeed the reason of this discrepancy. Unfortunately this issue was not resolved within the time-frame of this thesis.

Figures 6.29 and 6.30 show, respectively, the energy of the ME for the on- and off-time window and the off-time subtracted energy distribution. In the first figure the same scaling issue is present as is discussed for the distance distribution. Figure 6.30 shows an increase around an SEvent amplitude of 20000 ADC. According to the preliminary conversion of 588 ADC/MeV, derived in section 6.4, this corresponds to a value of around 34 MeV. This is compatible with the Michel electron energy distribution quoted in literature [81] and the one measured by the MicroBooNE experiment, see figure 6.31 [96].

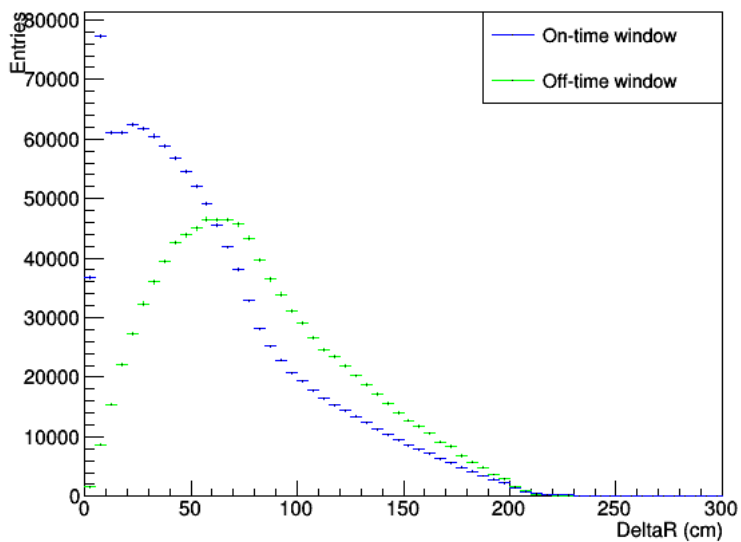


Figure 6.26: The shortest distance between the muon track and the Michel electron for the on-time and off-time window.

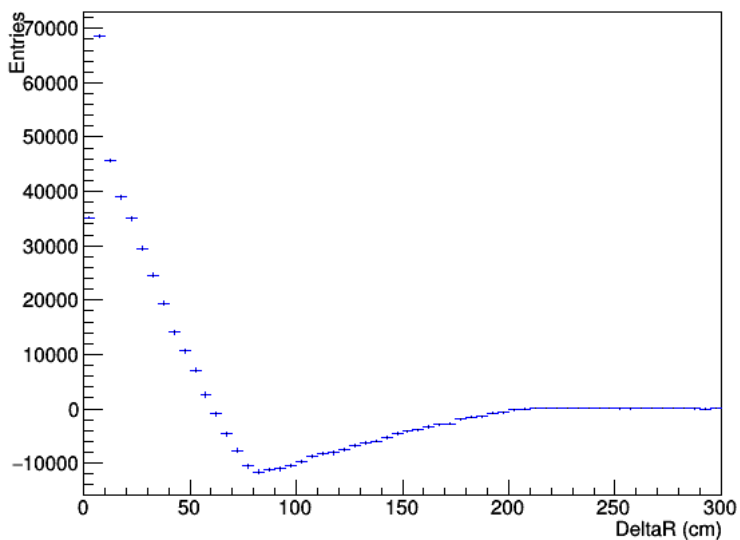


Figure 6.27: The shortest distance between the muon track and the Michel electron, off-time window subtracted.

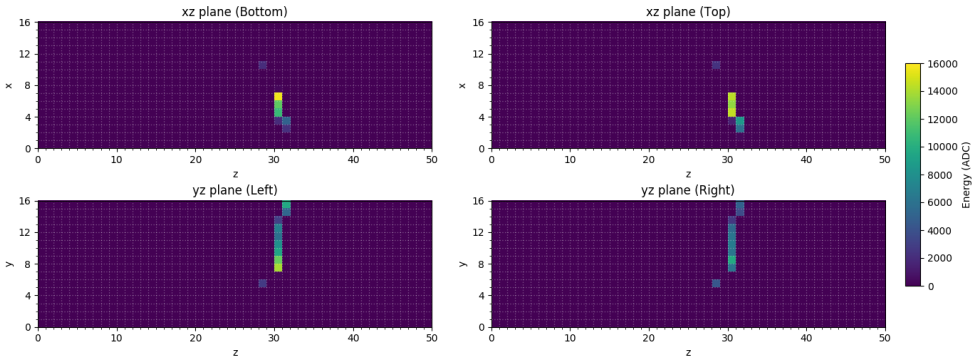


Figure 6.28: Muon decay and subsequent Michel electron interaction in the Phase 1 detector.

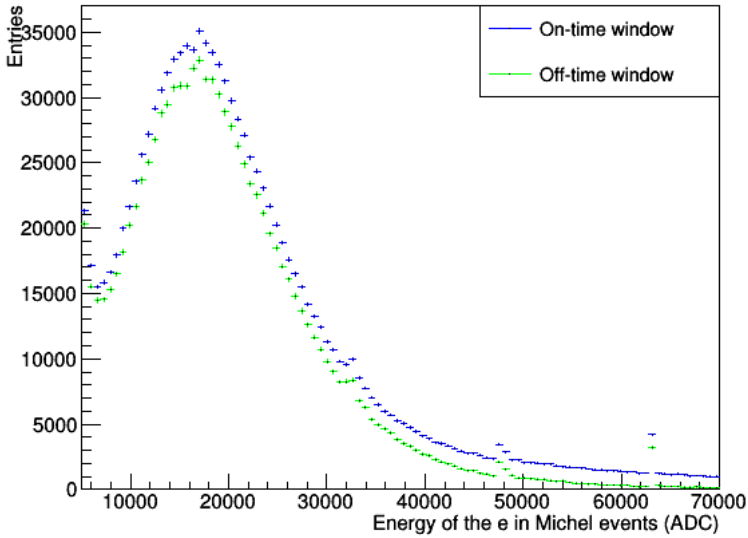


Figure 6.29: The energy of the Michel electrons for the on-time and off-time window.

6.5.2 Spallation neutrons

Similar to the study of Michel electrons, one can search for spallation neutrons produced by muons inside the detector with the same on- and off-time window technique.

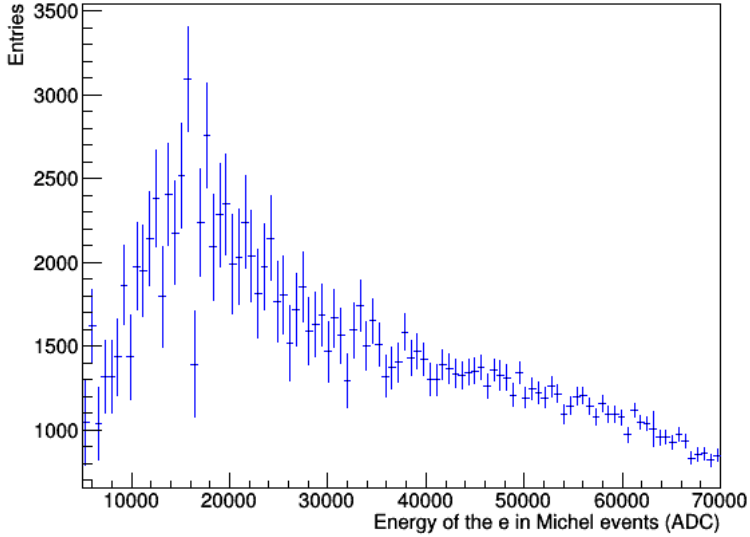


Figure 6.30: The energy of the Michel electrons, off-time window subtracted.

Figure 6.32 shows the on- and off-time windows that are used in this study. Since a much longer time difference is expected for neutrons produced by a muon than for the Michel electron signals, due to the neutron thermalisation time, the windows are now taken significantly larger.

The muons and neutrons used in this study are identified in Saffron2. The only cut used for this analysis is to not select those neutrons where an electromagnetic signal (not a muon) occurred between the muon and the neutron and if this signal and the neutron take place within the same cube. This cut is used to eliminate the BiPo⁸ background in the selected sample.

By plotting the time difference between the occurrence of the muon and the neutron it is possible to determine the neutron capture time. The on-time window is fit with an exponential plus a straight line. The last feature is used to model the background, which has a long tail. Figure 6.33 shows the fitted on-time window, with the off-time window also plotted. The neutron capture time given by the fit is $\tau_n = [64.60 \pm 1.23 \text{ (stat)} \pm 0.01 \text{ (syst)}] \mu\text{s}$.

Subtracting the off-time window from the on-time window and fitting this distribution with a simple exponential provides a second way to determine the neutron capture time. Figure 6.34 shows the subtracted time distribution

⁸ ^{214}Bi is present in the ZnS layers on the cubes and is a (γ, β) emitter that decays to ^{214}Po , which is an α emitter with a half-life of $164 \mu\text{s}$. The detection of the electron followed by the α particle provides a background for the IBD signal.

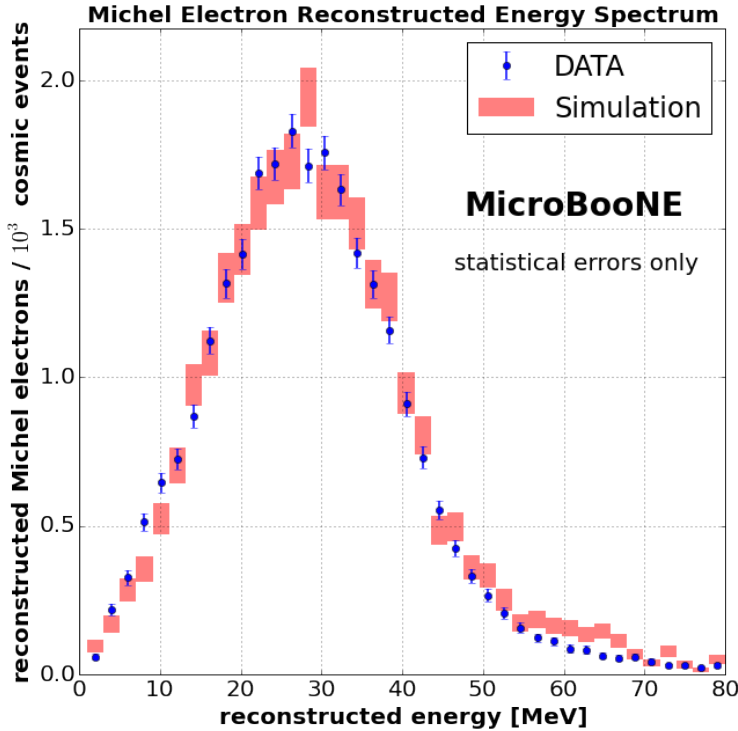


Figure 6.31: The Michel electron energy spectrum measured by the MicroBooNE experiment. The energy reconstruction for data and Monte Carlo events is compared [96].

and the exponential fit.

A neutron capture time of $\tau_n = [65.30 \pm 1.30 \text{ (stat)} \pm 0.01 \text{ (syst)}] \mu\text{s}$ is obtained.

For both values, the systematic error is determined by repeating the fit while excluding the first bin, and taking the difference in τ_n as a 1σ error.

The values for the neutron capture time found with both methods are consistent with each other. Moreover, they are also compatible with the value determined from IBD simulation $\tau_n = [62.70 \pm 0.05] \mu\text{s}$ [90].

Investigating the distance between the muon and neutron, see figures 6.35 and 6.36, shows that the neutron usually is detected close to the muon and at most 10 cubes (~ 50 cm) away. This feature will be used in the application of a muon veto. For example, one could veto only part of the detector after the passage of a muon to reduce dead-time.

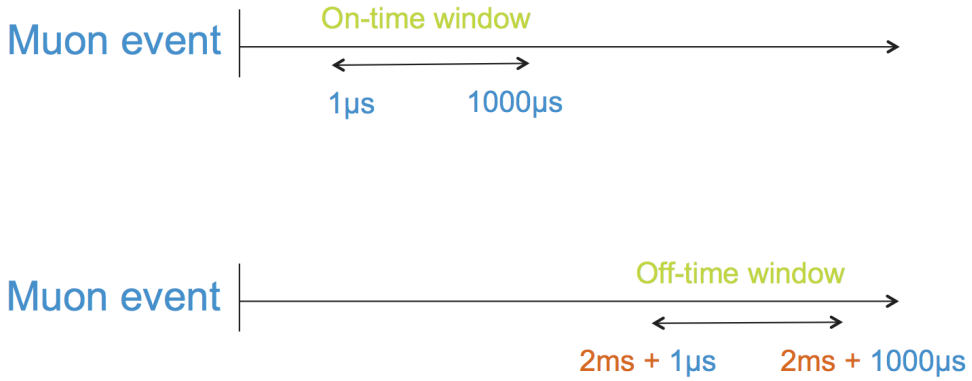


Figure 6.32: Schematic representation of the on-time and off-time window approach used for the study of spallation neutrons.

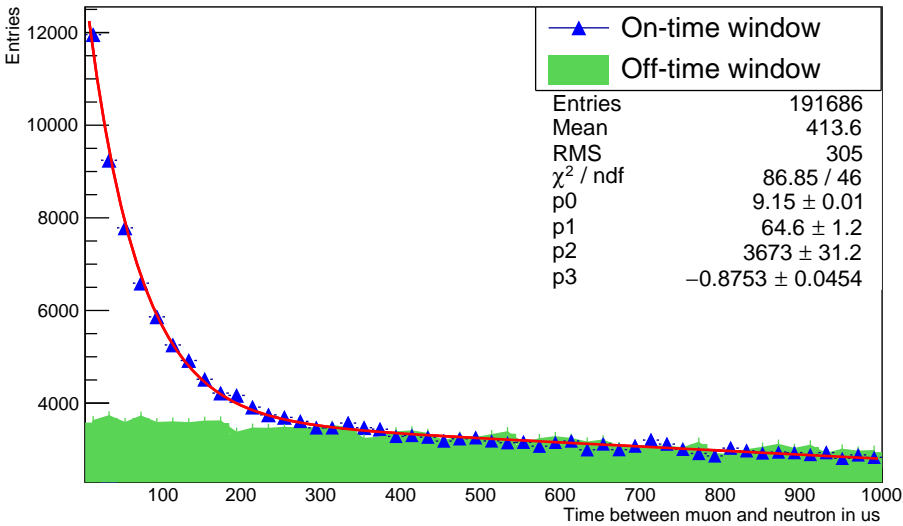


Figure 6.33: Determination of the neutron capture time by fitting an exponential plus a straight line to the on-time window. A neutron capture time of $\tau_n = [64.60 \pm 1.23 \text{ (stat)} \pm 0.01 \text{ (syst)}] \mu\text{s}$ is found. The off-time window is visible in green.

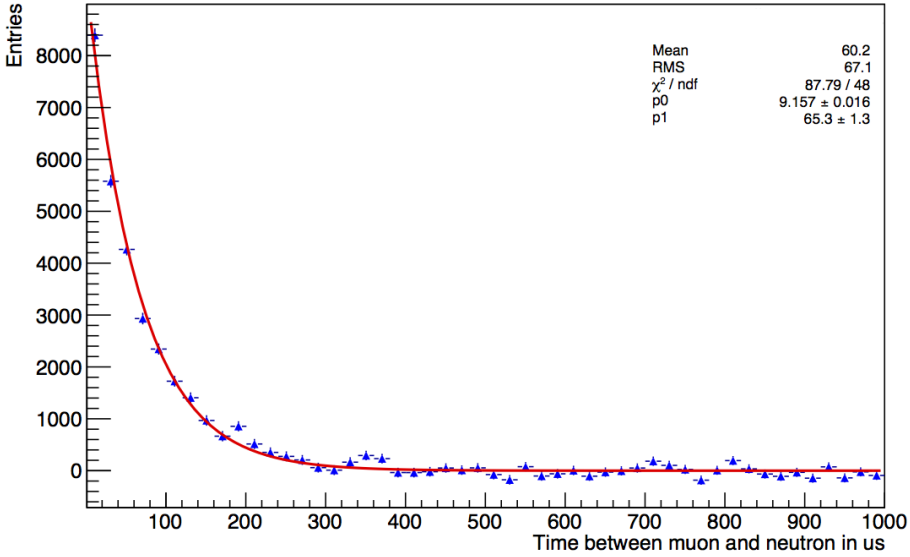


Figure 6.34: Determination of the neutron capture time by fitting an exponential to the off-time subtracted time distribution. A neutron capture time of $\tau_n = [65.30 \pm 1.30 \text{ (stat)} \pm 0.01 \text{ (syst)}] \mu\text{s}$ is obtained.

6.6 Conclusion

This chapter discusses the proto-analysis performed on the data collected with the 4-module Phase 1 detector in December. More specifically, it explains the Saffron2 analysis framework which takes care of SPeak, SEvent and object identification.

In the scope of this thesis algorithms were written to identify muonCube and muonTrack objects, see section 6.3.3. An algorithm was also started to fit a track to the muonTrack objects in order to perform a channel-to-channel basis calibration, explained in section 6.4.

It was found that the muonCube and muonTrack objects are quite pure. A clear inverse correlation with the outside pressure is observed and a pressure corrected muon rate is stable during reactor-on and reactor-off periods. This indicates low contamination by gamma's or other reactor-induced particles. Unfortunately, the muon efficiency, on the other hand, is rather low (88.3 %). Section 6.3.4 discussed the possibility to raise this efficiency after the Saffron2 processing by the identification of a third muon object.

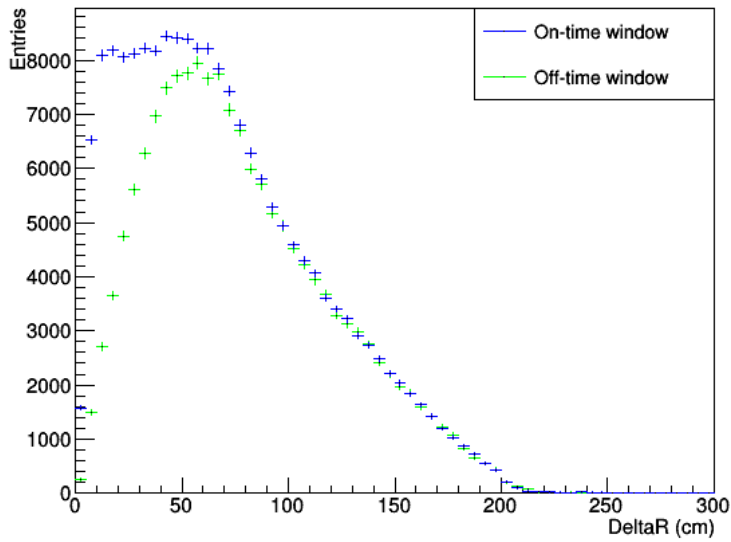


Figure 6.35: The shortest distance between the muon track and the neutron for the on-time and off-time window.

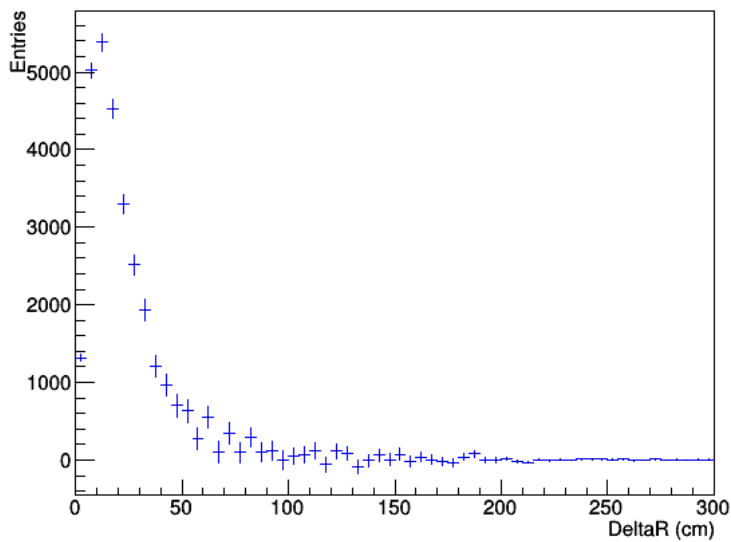


Figure 6.36: The shortest distance between the muon track and the neutron, off-time window subtracted.

Including this muonExtra object increases the muon efficiency up to 95.4 %.

After the identification of the basic objects, such as muons and neutrons, coincidences between these objects could be analysed.

A study of Michel electrons with the Phase1 data allowed to determine the muon decay time. This is found to be $\tau_\mu = [2.13 \pm 0.01 \text{ (stat)} \pm 0.05 \text{ (syst)}] \mu\text{s}$, compatible with the value quoted in literature. This result indicates that the basic Phase 1 principles are well understood.

A value for the neutron capture time on the Li screens can be found by analysing the coincidence between muons and the thereby created neutrons. This leads to a value of $\tau_n = [65.30 \pm 1.30 \text{ (stat)} \pm 0.01 \text{ (syst)}] \mu\text{s}$, in agreement with the value found from IBD simulations. Moreover it is found that neutrons interact relatively close to the muon, and almost never further away than 10 cubes. This feature could be used to improve a muon veto, by, for example, only vetoing a part of the detector around the muon.

The studies performed within the proto-analysis group had as goal to analyse the Phase 1 December data with a rudimentary approach. The main target was to understand the detector and get an initial idea about topics such as object identification, backgrounds and IBD selection cuts.

The results presented here show that the Phase 1 detector is already well understood and known physics, such as the muon decay time, can be reconstructed accurately. Several ideas were discussed on how to develop the analysis further so that the improved muon objects can be used in an efficient muon veto and for muon calibration purposes in the future.

Conclusion

7

Since their postulation in 1930 by Pauli, neutrinos have been the subject of much discussion and research. Decades of experiments have provided scientists with a clear picture of three families of neutrinos oscillating into each other. However, several results are in tension with this framework. They are collectively referred to as the neutrino anomalies.

One of these anomalies is the reactor antineutrino anomaly, which was discovered after a re-evaluation of the neutrino flux of several short-baseline reactor experiments. An updated ratio of measured over predicted rate of reactor antineutrinos was found to deviate from unity at the 98.6 % C.L.. This result could be explained by a fault in the flux predictions, but the existence of a sterile neutrino could also cause this anomaly.

Sensitive experiments are needed to resolve the inconsistencies in the neutrino sector. One of these experiments is SoLid, which targets to resolve the reactor antineutrino anomaly by performing a very short baseline measurement of the neutrino spectrum at the BR2 reactor at SCK•CEN. With a novel technology, using $5 \times 5 \times 5 \text{ cm}^3$ PVT scintillator cubes equipped with $^6\text{LiF:ZnS(Ag)}$ neutron sensitive screens, it aims to detect inverse beta decay interactions from the reactor antineutrinos.

The work of this thesis started in the summer of 2014 with the construction of the large-scale prototype SubModule 1, consisting of 2304 cubes structured in 9 frames, which was designed to evaluate the feasibility of the technology. The construction took place at Ghent University, where I was responsible for operations during construction and where I was also involved in the frame commissioning.

Due to planned reactor refurbishments and a long on-site commissioning period, SM1 was only able to collect a few days of reactor-on data in February 2015. Despite this, some electronics issues and relatively low light-yield, the prototype was able to demonstrate that neutrons can be distinguished from

other particle interactions and that the high position precision of the detector provides an efficient way to reduce backgrounds.

As the SoLid detector is located above ground it will suffer from high cosmic ray induced backgrounds. Since cosmic muons and neutrons can generate IBD backgrounds, it is very important to understand these interactions in order to be able to distinguish them from the signal. In the scope of this thesis a dedicated cosmic simulation package “CosmicGen” was developed. The simulation results showed good agreement with SM1 data, indicating that the simulation chain was accurate.

A study of Michel electrons following muon decay performed with the SM1 data provided a muon decay time compatible with the value quoted in literature. This indicated both a good understanding of the basic properties of the SM1 prototype, such as timing and object identification, and showed that it is possible to identify prompt-delayed signals, as is the aim when searching for IBD signals.

Using the experience and results obtained with the prototype, the full-scale Phase 1 detector, consisting of 12800 cubes structured in 50 frames, was built between December 2016 and November 2017. Several upgrades regarding light-yield and electronics performances were made. The construction and frame commissioning again took place at Ghent University. My tasks consisted of material procurement, training of manpower, construction and quality assurance of the frames.

In October 2017, 4 out of 5 modules of the Phase 1 detector were transported to the BR2 reactor. After a relatively short installation and on-site commissioning period, the detector collected reactor-on and -off data during December. This data was used as a burn sample in the proto-IBD analysis group. The aim of this group was to understand the basic behaviour of the detector and to perform initial studies on data quality, basic object reconstruction, backgrounds and IBD signals.

My task within the proto-IBD group was to reconstruct muon objects so they could be used in a muon veto for the IBD search. Analysis of the muons also showed a stable behaviour of most detector planes and of the detector over time. By investigating Michel electrons following a muon, the muon decay time could be reconstructed accurately. The identification of neutrons after a muon interaction, allowed for the measurement of the neutron capture time.

All these results, and others from the proto-IBD group, showed that the Phase 1 detector is well understood and is capable of reconstructing well-known physical processes, such as the muon decay. These analyses were performed in a rudimentary way, but provide a decent basis for further studies,

which will be performed in the SoLid Collaboration.

It is expected that the SoLid experiment will be able to make a sensitive measurement over the course of a few years, to either confirm or reject the existence of a sterile neutrino. Thereby solving one of the most debated issues in particle physics.

Nederlandstalige samenvatting

8

Sinds hun postulatie in 1930 door Pauli, zijn neutrinos het onderwerp geweest van veel onderzoek en discussie. Tientallen jaren van experimententele waarnemingen hebben een duidelijk beeld gevormd van 3 smaken neutrinos die in elkaar oscilleren. Desondanks de vele resultaten die deze theorie staven, zijn er toch enkele data sets die niet compatibel blijken te zijn. Deze worden gezamenlijk de “neutrino anomalieën” genoemd.

Eén van deze anomalieën is de reactor antineutrino anomalie, dewelke pas aan het licht kwam na de her-evaluatie van de neutrino flux van enkele kortereafstand reactor experimenten. Een geüpdatete waarde van de ratio van gemeten over voorspeld aantal reactor antineutrinos blijkt af te wijken van één in de 98.6 % C.L.. Dit resultaat kan worden verklaard door een fout in de flux berekeningen, maar ook door het bestaan van een steriel neutrino.

Nauwkeurige experimenten zijn nodig om de anomalieën in de neutrino sector te kunnen verklaren. Een van deze experimenten is SoLid, met als doel het ontrafelen van de reactor antineutrino anomalie door het meten van een zeer kortereafstand neutrino spectrum aan de BR2 reactor in het SCK•CEN. Gebruikmakend van een nieuwe technologie, gebaseerd op de combinatie van $5 \times 5 \times 5 \text{ cm}^3$ PVT scintillatie kubussen en ${}^6\text{LiF:ZnS(Ag)}$ neutron gevoelige plaatjes, detecteert SoLid reactor antineutrinos via het invers beta-verval (IBV) proces.

Deze thesis startte in 2014 met de bouw van een grootschalig prototype, SubModule 1 (SM1), gemaakt uit 2304 kubussen gepositioneerd in 9 frames. Het doel van dit prototype was het testen van de technologie op grote schaal. De constructie vond plaats in de Universiteit Gent, waar ik verantwoordelijk was voor de activiteiten tijdens de constructie en waar ik ook intensief betrokken was bij de kwaliteitscontrole van de individuele frames.

Door een gepland onderhoud van de BR2 reactor en een lange inbedrijf-

stelling ter plaatse, heeft SM1 slechts enkele dagen reactor-aan data kunnen waarnemen in februari 2015. Ondanks deze tegenslag, enkele elektronica problemen en een relatief lage lichtopbrengst, kon het prototype toch aantonen dat neutronen in de detector konden onderscheiden worden van andere deeltjes en dat de nauwkeurige positiebepaling een krachtig instrument is in het identificeren van achtergronden.

Aangezien de SoLid detector zich bovengronds bevindt, zullen er hoge kosmische achtergronden worden waargenomen. Aangezien kosmische neutronen en muonen achtergronden kunnen genereren voor het invers beta-verval, is het uitermate belangrijk om deze interacties goed te kunnen onderscheiden van het gezochte signaal. In het kader van deze thesis werd daarom een toegewijd kosmisch simulatie pakket "CosmicGen" ontwikkeld. De SM1 data en simulatie waren compatibel, hetgeen aantoont dat de kosmische simulatie keten betrouwbaar is.

Uit een studie met de SM1 data van de Michel elektronen die volgen op het muon verval, kon een waarde van de muon verval tijd bepaald worden dewelke in overeenstemming is met wat in de literatuur wordt vermeld. Deze studie kon aantonen dat de basis principes van de prototype detector, zoals timing en object identificatie, goed begrepen zijn, alsook de mogelijkheid van het identificeren van een prompt-uitgesteld signaal. Dit laatste is namelijk ook het doel bij het uitvoeren van een IBV analyse.

Gebruikmakend van de ervaring en resultaten verkregen met de SM1 prototype detector, werd de volledige Phase 1 detector, gemaakt uit 12800 kubussen verdeeld in 50 frames, gebouwd tussen december 2016 en november 2017. Verschillende upgrades aangaande lichtopbrengst en elektronica werden doorgevoerd. De constructie en kwaliteitscontrole van de frames vond opnieuw plaats in de Universiteit Gent. Mijn taken bestonden eruit om de stock van materialen op te volgen, mankracht op te leiden, constructie uit te voeren en de kwaliteit van de individuele frames te testen en indien nodig te verbeteren.

In oktober 2017 werden 4 van de 5 Phase 1 modules getransporteerd naar de BR2 reactor. Na een relatief korte installatie en ingebruikstelling periode, kon Phase1 reeds reactor-aan en -uit data verzamelen in december. Deze data werden gebruikt als test-sample voor de proto-IBV analyse groep. Het doel van deze groep was om de basis principes van de detector te begrijpen, initiële studies uit te voeren omtrent data kwaliteit, basis object reconstructie, achtergronden en invers beta-verval parameters.

Mijn bijdrage aan de proto-IBV groep bestond er uit om muon objecten te reconstrueren zodat deze konden gebruikt worden in een muon veto in de IBV analyse. Onderzoek van deze muonen toonde ook aan dat de detector

stabil was over de duur van de data-periode en dat de meeste detector frames onderling ook gelijkaardig gedrag vertoonden. De muon vervaltijd kon opnieuw accuraat worden bepaald uit een studie van de Michel elektronen. Daarnaast kon een studie van neutronen gecreëerd door muonen de neutron invang-tijd bepalen.

Al deze resultaten, en andere waargenomen in de proto-IBV groep, konden aantonen dat de Phase 1 detector relatief goed begrepen is en stabiel gedrag vertoont. Het bleek ook mogelijk om gekende fysische processen, zoals het verval van het muon, nauwkeurig waar te nemen. Deze analyses werden uitgevoerd op een rudimentaire manier, maar bieden wel een goede basis voor verdere studies die zullen uitgevoerd worden binnen de SoLid Collaboratie.

Het wordt verwacht dat het SoLid experiment de komende jaren een nauwkeurige meting zal uitvoeren, dewelke het bestaan van het steriel neutrino zal kunnen bevestigen of weerleggen. Daarbij zal het een van de meest gedebatteerde vraagstukken binnen de deeltjesfysica kunnen oplossen.

ALOA (A Lot Of Abbreviations)

C

- Calipso: Calibration per plane for SoLid
- CC: Charged current
- CROSS: Calibration on site SoLid

D

- DAQ: Data acquisition

E

- EB: Electronics box
- EM: Electromagnetic

F

- FFT: Fast Fourier transform

H

- HEU core: Highly enriched uranium core
- HDPE: High density polyethylene
- HV: High voltage

I

- IBD: Inverse beta decay
- ID: Identification

M

- MC: Monte Carlo
- MCNP: Monte Carlo n-particle
- MPPC: Multi-pixel photon counter

N

- NC: Neutral current

P

- PA: Pixel avalanche
- PCB: Printed circuit board
- PMNS matrix: Pontecorvo Maki Nakagawas Sakata matrix
- PoT: Peak over threshold
- PVT: Polyvinyl toluene

R

- RAA: Reactor antineutrino anomaly
- RMS: Root mean square
- RO: ReadOut simulation

S

- Saffron: SoLid analysis framework
- SBL: Short baseline
- SM: Standard Model of particle physics
- SM1: SubModule 1
- SoLid: Search for Oscillations with a ^6Li detector

V

- VSBL: Very short baseline

W

- WLS fibres: Wavelength shifting fibres

List of Figures

1.1	The elementary particles and forces of the Standard Model of particle physics.	4
1.2	Energy spectrum of the electron in the beta decay.	5
1.3	Mass distribution of the Z boson	7
1.4	The normal and inverted neutrino mass hierarchy.	11
1.5	The Super-Kamiokande experiment.	12
1.6	The SNO experiment.	13
1.7	Solar and KamLAND neutrino parameter space.	15
1.8	MINOS neutrino parameter space.	16
1.9	RENO χ^2 distribution as a function of $\sin^2(2\theta_{13})$	17
1.10	The observed deficit of neutrinos in radioactive source experiments.	18
1.11	$R^{\bar{\nu}_e}$ measurements at several short baseline reactor neutrino experiments.	20
1.12	$R^{\bar{\nu}_e}$ measurements vs. baseline of several short baseline reactor neutrino experiments.	21
1.13	Prompt energy spectrum with 5 MeV distortion.	22
1.14	The reactor antineutrino anomaly.	24
1.15	Allowed parameter region for reactor experiments.	25
1.16	Allowed parameter region for a global data set.	25
1.17	The STEREO experiment.	27
1.18	The PROSPECT experiment.	27
1.19	The SOX experiment.	28
2.1	Layout of the BR2 building at the SoLid level.	33
2.2	The BR2 twisted matrix core from above.	33
2.3	Signal due to the positron (top) and neutron (bottom) capture.	37
2.4	SoLid composite scintillator detection unit.	37
2.5	Partly assembled NEMENIX prototype detector.	38

2.6	NEMENIX placed in front of the BR2 reactor.	39
3.1	Diagram of the prototype detector, exploded frame, fibre read-out and cube assembly.	43
3.2	A SM1 cube in an open Tyvek wrapper with ${}^6\text{Li}$ screen on top (left) and a wrapped SM1 cube with 2 perpendicular fibres (right).	44
3.3	Picture of the side of an SM1 frame.	44
3.4	The SM1 prototype with the bottom and back side of the shielding and the steel plate attached.	45
3.5	Picture of a partly filled SM1 frame.	47
3.6	Pictures illustrating the SM1 plane commissioning set-up.	48
3.7	The SM1 prototype within its shielding installed in front of the R1 port of the BR2 reactor.	49
3.8	Sketch of the two positions of the ${}^{241}\text{Am}{}^9\text{Be}$ source.	50
3.9	Examples of the digital irregularities and periodic noise found in the data.	51
3.10	A charged particle signal and a neutron signal waveform.	52
4.1	Sketch of the CosmicGen bounding box and generation surface.	58
4.2	The SM1 coordinate system and definition of the zenith (θ) and azimuthal (ϕ) angle.	58
4.3	Energy distribution of cosmic muons simulated with 3 different generators, without a bounding box.	60
4.4	Energy distribution of cosmic muons simulated with 3 different generators, with a bounding box of SM1 size.	60
4.5	Zenith angle distribution of cosmic muons simulated with 3 different generators, without bounding box.	61
4.6	Zenith angle distribution of cosmic muons simulated with 3 different generators, with bounding box of SM1 size.	61
4.7	Azimuthal angle distribution of cosmic muons simulated with 3 different generators, without bounding box.	62
4.8	Azimuthal angle distribution of cosmic muons simulated with 3 different generators, with bounding box of SM1 size.	62
4.9	Energy distribution of cosmic neutrons simulated with 2 different generators.	64
4.10	Energy distribution of cosmic neutrons simulated with 2 different generators with a bounding box of SM1 size.	64
4.11	Zenith angle distribution of cosmic neutrons simulated with 2 different generators, without bounding box.	67

4.12	Zenith angle distribution of cosmic neutrons simulated with 2 different generators, with bounding box of SM1 size.	67
4.13	Azimuthal angle distribution of cosmic neutrons simulated with 2 different generators, without bounding box.	68
4.14	Azimuthal angle distribution of cosmic neutrons simulated with 2 different generators, with bounding box of SM1 size.	68
4.15	Geant4 simulation of the SM1 detector, with an indication of the SoLid coordinate system.	69
4.16	Sketches of the 3 different bounding boxes imposed on the Geant4 simulation model of the BR2 building.	70
4.17	Sketches of the 3 different bounding boxes imposed on the Geant4 simulation model of the BR2 building, plus the 350 m × 350 m generation surface.	71
4.18	Comparison of the cosine θ distribution of muon tracks for the Guang based Monte Carlo tuples and data tuples.	73
4.19	Comparison of the azimuthal angle distribution of muon tracks for the Guang based Monte Carlo tuples and data tuples.	74
4.20	Comparison of the energy distribution of muon cubes for the Guang based Monte Carlo tuples and data tuples.	75
4.21	Determination of the muon track and cube rate in the SM1 detector.	76
4.22	Schematic representation of the on-time and off-time window approach used for the study of Michel electrons.	76
4.23	Determination of the muon decay time by fitting an exponential plus a constant to the on-time window.	77
4.24	Determination of the muon decay time by fitting an exponential to the off-time subtracted time distribution.	78
4.25	The shortest distance between the muon track and the Michel electron for the on-time and off-time window.	79
4.26	The shortest distance between the muon track and the Michel electron, off-time window subtracted.	79
4.27	The energy of the Michel electrons for the on-time and off-time window.	80
4.28	The energy of the Michel electrons, off-time window subtracted.	80
5.1	Picture of a Phase 1 module with electronics boxes attached in a test set-up at the Ghent University lab.	86
5.2	Picture of 1 Phase 1 module inserted in the container.	87
5.3	The left figure shows the HDPE plates on top of the container. The right figure shows the closed water wall from the side.	87

5.4	Picture of 4 modules inserted in the container, plus 2 HDPE plates, one at the front and 1 at the back of the container.	88
5.5	Picture showing the storage box for a cut batch of Li with a paper documenting the necessary information (left). The set-up used in the cutting process of the plain Li screens is shown on the right.	90
5.6	Pictures of the wooden tool (left) and the press (right) used to cut the punched Li screens.	91
5.7	Pictures showing the washing, rinsing (left) and drying (right) of cubes.	91
5.8	Pictures showing the database workstation (left) and the transfer tray plus cube materials (right).	92
5.9	Pictures showing the metal template used to position the cube correctly within the Tyvek (left) and the cube storage box (right).	93
5.10	Picture showing the correct orientation of the frame for construction based on the position of the holes.	93
5.11	Picture showing the back of an aluminium frame equipped with a big Tyvek sheet.	94
5.12	Picture of a corner of an Al frame. The HDPE bars and the corner cubes are visible.	94
5.13	Picture of the corner cube and how the bar-code was orientated.	95
5.14	Picture of the MPPC on the PCB. An A3 reference sheet was used to keep track of all information about the MPPCs installed on a given frame.	97
5.15	Picture of the 2 types of connectors with a fibre inserted. The MPPC connector with MPPC is visible on the left and the mirror connector on the right.	97
5.16	Pictures showing the connection between MPPC and fibre (left) and the installation of the connector in the frame with help of the dedicated tool (right).	98
5.17	Application of optical grease with the help of a syringe for the MPPC connector (left) and the mirror connector (right).	99
5.18	Picture showing the top side of a frame with both MPPC and mirror connectors installed.	100
5.19	Calipso set-up for the EM source measurements.	101
5.20	Calipso set-up for the neutron source measurements.	102
5.21	Light-yield ratio from data and Monte Carlo measured with the neutron source before (left) and after (right) fixing the frame.	102

6.1	Sketches of the Geant4 geometry of the BR2 building and Phase 1 detector, plus the used bounding box.	107
6.2	Diagram of the threshold trigger (above) and the neutron trigger (below). The blue block indicates the time block following the trigger. The orange blocks indicate the part of the waveform that is stored [92].	109
6.3	Mean amplitude versus mean IonA value for cubes processed by the SOnlineNeutronID algorithm.	111
6.4	MuonTrack event in the Phase 1 detector.	113
6.5	MuonCube event in the Phase 1 detector.	113
6.6	Number of vertical (V) channels as a function of the SEvent energy for simulated muons not tagged as muonCube or muonTrack.	114
6.7	Number of horizontal (H) channels as a function of the SEvent energy for simulated muons not tagged as muonCube or muonTrack.	115
6.8	Number of horizontal (H) versus vertical (V) channels for simulated muons not tagged as muonCube or muonTrack.	115
6.9	Number of vertical (V) channels as a function of the SEvent energy for simulated muons not tagged as muonCube, muonTrack or with the extra cut.	117
6.10	Number of horizontal (H) channels as a function of the SEvent energy for simulated muons not tagged as muonCube, muonTrack or with the extra cut.	118
6.11	Number of horizontal (H) versus vertical (V) channels for simulated muons not tagged as muonCube, muonTrack or with the extra cut.	118
6.12	Determination of the muonTrack rate in Phase 1.	119
6.13	Determination of the muonCube rate in Phase 1.	119
6.14	Distribution of muonCube and muonTrack interactions over the detector planes.	120
6.15	Correlation of environmental parameters, outside temperature and outside pressure, with the muon rate.	122
6.16	Muon rate distribution before pressure correction.	123
6.17	Muon rate distribution after pressure correction.	123
6.18	Fit to a muonTrack object for the horizontal channels (top) and vertical channels (bottom) separately.	124
6.19	Distribution of dE versus dx for isolated cubes in a muonTrack object.	125
6.20	Distribution of dE/dx for values of dx between 5.5 and 6 cm.	126

6.21	Distribution of the difference between the reconstructed pathlength obtained with the fit and the simulated pathlength. . . .	126
6.22	Bad fit to a muonTrack object for the horizontal channels (top) and vertical channels (bottom) separately.	127
6.23	Schematic representation of the on-time and off-time window approach used for the study of Michel electrons.	128
6.24	Determination of the muon decay time by fitting an exponential plus a constant to the on-time window.	129
6.25	Determination of the muon decay time by fitting an exponential to the off-time subtracted time distribution.	130
6.26	The shortest distance between the muon track and the Michel electron for the on-time and off-time window.	131
6.27	The shortest distance between the muon track and the Michel electron, off-time window subtracted.	131
6.28	Muon decay and subsequent Michel electron interaction in the Phase 1 detector.	132
6.29	The energy of the Michel electrons for the on-time and off-time window.	132
6.30	The energy of the Michel electrons, off-time window subtracted.	133
6.31	The Michel electron energy spectrum measured by the Micro-BooNE experiment.	134
6.32	Schematic representation of the on-time and off-time window approach used for the study of spallation neutrons.	135
6.33	Determination of the neutron capture time by fitting an exponential plus a straight line to the on-time window.	135
6.34	Determination of the neutron capture time by fitting an exponential to the off-time subtracted time distribution.	136
6.35	The shortest distance between the muon track and the neutron for the on-time and off-time window.	137
6.36	The shortest distance between the muon track and the neutron, off-time window subtracted.	137

List of Tables

1.1	The elementary fermions	3
1.2	Summary of the neutrino oscillation parameters.	14
2.1	Summary of the BR2 properties.	34
3.1	Masses and hydrogen content of detector components.	47
3.2	Summary of data taken with SM1.	51
4.1	Comparison of the muon rate and energy for the 3 cosmic muon generators.	59
4.2	Comparison of the neutron rate and energy for the 2 cosmic neutron generators.	65
6.1	Available Geant4 and RO simulations.	108

Bibliography

- [1] J.J. Thompson, "On the structure of the atom," *Philosophical Magazine and Journal of Science*, vol. 7, 1904.
- [2] J.J. Thompson, "Cathode Rays," *Philosophical Magazine and Journal of Science*, vol. 5, 1897.
- [3] E. Rutherford, "The Scattering of α and β Particles by Matter and the Structure of the Atom," *Philosophical Magazine and Journal of Science*, vol. 21, 1911.
- [4] E. Rutherford, "Collision of alpha Particles with Light Atoms; An Anomalous Effect in Nitrogen," *Philosophical Magazine and Journal of Science*, vol. 37, 1919.
- [5] J. Chadwick, "Possible Existence of a Neutron," *Nature*, p. 312, 1932.
- [6] M. Gell-Mann, "A schematic model of baryons and mesons," *Phys. Lett.*, vol. 8, 1964.
- [7] G. Zweig, "An SU(3) model for strong interaction symmetry and its breaking," *CERN Geneva - TH. 401 (REC.JAN. 64)*, 1964.
- [8] CERN, "The Standard Model," *CERN Document Server*.
- [9] J. Beringer et al., "Review of Particle Physics," *Phys. Rev. D*, vol. 86, p. 010001, 2012.
- [10] R. Mcknie, "Ghost traps: the hunt for dark matter," *Cosmos*, 2015.
- [11] CMS Collaboration, "Observation of a new boson at a mass of 125 GeV with the CMS experiment at the LHC," *Phys. Lett. B*, vol. 716, p. 30, 2012.
- [12] ATLAS Collaboration, "Observation of a new particle in the search for the Standard Model Higgs boson with the ATLAS detector at the LHC," *Phys. Lett. B*, vol. 716, pp. 1–29, 2012.

- [13] M. Thomson, *Modern particle physics*. Cambridge University Press, 2015.
- [14] K. N. Abazajian, "Light sterile neutrinos: A white paper," *arXiv:1204.5379*, 2012.
- [15] NEMO Collaboration, "Physics goals - Neutrinos," <http://nemo.in2p3.fr/physics/neutrinos.php>, 2004.
- [16] E. Fermi, "Quantum Theory of Radiation," *Reviews of Modern Physics*, vol. 4, 1932.
- [17] F. Reines et al., "Detection of the free antineutrino," *Phys. Rev.*, vol. 117, p. 159, 1960.
- [18] L. Lederman et al., "Observation of High-Energy Neutrino Reactions and the Existence of Two Kinds of Neutrinos," *Phys. Rev. Letters*, vol. 9, 1962.
- [19] M. L. Perl, "The new particles produced in electron-positron annihilation," *SLAC-PUB-1652*, 1975.
- [20] DONUT collaboration, "Observation of tau neutrino interactions," *Phys. Lett. B*, vol. 504, pp. 218–224, 2000.
- [21] ALEPH Collaboration (D. DeCamp et al.), "Determination of the number of light neutrino species," *Phys. Lett. B*, vol. 231, no. 4, pp. 519–529, 1989.
- [22] The ALEPH Collaboration, "Precision Electroweak Measurements on the Z Resonance," *Physics Reports*, vol. 427, no. 257, 2006.
- [23] Alpher et al., "The Origin of Chemical Elements," *Phys. Rev.*, vol. 73, 1948.
- [24] R. Davis, Jr. and D. S. Harmer and K. C. Hoffman, "Search for neutrinos from the sun," *Phys. Rev. Lett.*, vol. 20, p. 1205, 1968.
- [25] K. S. Hirata et al., "Observation of ^8B solar neutrinos in the Kamiokande-II detector," *Phys. Rev. Lett.*, vol. 63, no. 1, p. 16, 1989.
- [26] G. Conforto et al., "A complete solution to neutrino mixing," *Astropart. Phys.*, vol. 5, pp. 147–158, 1996.
- [27] B. Pontecorvo, "Neutrino Experiments and the Problem of Conservation of Leptonic Charge," *Sov. Phys. JETP*, vol. 26, pp. 984–988, 1968.
- [28] S. Eidelman et al., "Particle Data Group - The Review of Particle Physics," *Phys. Lett. B*, vol. 592, p. chapter 13, revised 2005.

- [29] A. Bettini, *Introduction to elementary particle physics*. Cambridge, 6 ed., 2008.
- [30] D. Griffiths, *Introduction to elementary particles*. Wiley VCH, 2008.
- [31] S. Mikheyev, P. Smirnov and A. Yu., "Resonance enhancement of oscillations in matter and solar neutrino spectroscopy," *Soviet Journal of Nuclear Physics*, vol. 42, 1985.
- [32] L. Wolfenstein, "Neutrino oscillations in matter," *Phys. Rev. D.*, vol. 17, 1978.
- [33] Hewett, J.L. et al., "Fundamental physics at the intensity frontier," *FERMILAB-CONF-12-879-PPD*, 2012.
- [34] The Super-Kamiokande Collaboration, Y. Fukuda et al., "Evidence for oscillation of atmospheric neutrinos," *Phys. Rev. Lett.*, vol. 81, pp. 1562–1567, 1998.
- [35] Super-Kamiokande Collaboration, "Outline of Super-Kamiokande experiment," <http://www-sk.icrr.u-tokyo.ac.jp/sk/index-e.html>, 2007.
- [36] The SNO Collaboration, "Measurement of Charged Current Interactions Produced by 8B Solar Neutrinos at the Sudbury Neutrino Observatory," *Phys. Rev. Lett.*, vol. 87, no. 071301, 2001.
- [37] Lynn Yarris, "Two Years of SNO Prove the Case: Solar Neutrinos Really Do Change," *ScienceBeat*, 2002.
- [38] D. V. Forero et al., "Neutrino oscillations refitted," *Phys. Rev. D*, vol. 90, p. 093006, 2014.
- [39] The KamLAND Collaboration, "Precision Measurement of Neutrino Oscillation Parameters with KamLAND," *Phys. Rev. Lett.*, vol. 100, p. 221803, 2008.
- [40] The MINOS Collaboration, "Measurement of the Neutrino Mass Splitting and Flavor Mixing by MINOS," *Phys. Rev. Lett.*, vol. 106, p. 181801, 2011.
- [41] The Daya Bay Collaboration, "Observation of Electron-Antineutrino Disappearance at Daya Bay," *Phys. Rev. Letters*, vol. 108, 2012.
- [42] RENO Collaboration, "Observation of Reactor Electron Antineutrinos Disappearance in the RENO Experiment," *Phys. Rev. Lett.*, vol. 108, p. 191802, 2012.

- [43] LSND Collaboration, "Evidence for $\bar{\nu}_\mu \rightarrow \bar{\nu}_e$ oscillations from the LSND Experiment at the Los Alamos Meson Physics Facility," *Phys. Rev. Lett.*, vol. 77, p. 3082, 1996.
- [44] A. A. Aguilar-Arevalo et al. (MiniBooNE Collaboration), "Event excess in the MiniBooNE search for $\bar{\nu}_\mu \rightarrow \bar{\nu}_e$ oscillations," *Phys. Rev. Lett.*, vol. 105, p. 181801, 2010.
- [45] GALLEX Collaboration, "Final results of the ^{51}Cr neutrino source experiments in GALLEX," *Phys. Lett. B*, vol. 420, no. 1, pp. 114–126, 1998.
- [46] J. N. Abdurashitov et al., "The Russian-American gallium experiment (SAGE) Cr neutrino source measurement," *Phys. Rev. Lett.*, vol. 77, p. 4708, 1996.
- [47] T. Schwetz, "Neutrinomassenspektrum: normal oder invertiert, und wieviele Masseneigenzustände gibt es?," *Seminar DPG Tagung*, 25th March 2014.
- [48] Y. Declais et al., "Study of reactor anti-neutrino interaction with proton at Bugey nuclear power plant," *Phys.Lett. B*, vol. 338, 1994.
- [49] A.I. Afonin et al., "A study of the reaction $\bar{\nu}_e + p \rightarrow e^+ + n$ on a nuclear reactor," *JETP*, vol. 94, 1988.
- [50] J.L. Vuilleumier et al., "New Limits on Oscillation Parameters for Electron Anti-neutrinos," *Phys.Lett. B*, vol. 114, 1982.
- [51] G. Mention et al., "The reactor antineutrino anomaly," *Phys. Rev. D*, vol. 83, p. 073006, 2011.
- [52] C. Giunti et al., "Updated global 3+1 analysis of short-baseline neutrino oscillations," *JHEP*, vol. 06, no. 135, 2017.
- [53] Double Chooz Collaboration, "Improved measurements of the neutrino mixing angle θ_{13} with the Double Chooz detector," *JHEP*, vol. 10, p. 086, 2014.
- [54] Pau Novella, "The Antineutrino Energy Structure in Reactor Experiments," *Advances in High Energy Physics*, 2015.
- [55] Patrick Huber, "NEOS data and the origin of the 5 MeV bump in the reactor antineutrino spectrum," *Phys. Rev. Lett.*, vol. 118, p. 042502, 2017.

- [56] J. Kopp et al., "Sterile Neutrinos or Flux Uncertainties? - Status of the Reactor Anti-Neutrino Anomaly," *JHEP*, vol. 11, no. 099, 2017.
- [57] L. Manzillas for the STEREO collaboration, "STEREO: Search for sterile neutrinos at the ILL," *Proceedings Of Science*, vol. arXiv:1702.02498, 2017.
- [58] PROSPECT Collaboration, "PROSPECT—A Precision Oscillation and Spectrum Experiment," <https://prospect.yale.edu/>, 2018.
- [59] L. Ludhova, SOX. IKP-2 Neutrino Group.
- [60] SCK•CEN, *BR2: Research reactor with multiple applications*. SCK•CEN, 2011.
- [61] T. A. Mueller et al., "Improved predictions of reactor antineutrino spectra," *Phys. Rev. C*, vol. 83, p. 054615, 2011.
- [62] V.M. Bui, L. Giot, M. Fallot et al., "Antineutrino emission and gamma background characteristics from a thermal research reactor," *arXiv:1602.07522*.
- [63] The SoLid Collaboration, "A novel segmented-scintillator antineutrino detector," *arXiv:1703.01683*, 2017.
- [64] Eljen Technology, "GENERAL PURPOSE: EJ-200, EJ-204, EJ-208, EJ-212," www.eljentechnology.com, 2016.
- [65] F. Yermia et al., "Search for oscillation with a lithium-6 detector at SCK•CEN BR2 research reactor," *Seminar Conseil Scientifique IN2P3*.
- [66] Saint-Gobain Crystals, "Plastic Scintillating Fibers," www.crystals.saint-gobain.com, 2017.
- [67] makeitfrom.com, "2017A Aluminium," , 2018.
- [68] Hamamatsu, "MPPC (multi-pixel photon counter)," www.Hamamatsu.com, 2013.
- [69] The SoLid Collaboration, "Performance of a full scale prototype detector at the BR2 reactor for the SoLid experiment," *JINST*, 2018.
- [70] Mathieu Labare, "Internal Communication on proton content," *SoLid DocDB*, 2016.
- [71] C. Moortgat P. Van Mulders, "Plane commissioning and attenuation study for SoLid module 1," *SoLid Technical note*, 2015.

- [72] D. Saunders, "First Data Reconstruction and Inverse Beta Decay Analysis at the Large Scale SoLid Prototype Detector," *solid-experiment.org*, 2017.
- [73] J. Allison et al., "Geant 4: a simulation toolkit," *Nuclear instruments and methods in physics research*, vol. 506, no. 3, 2003.
- [74] Doug Wright et al., "Monte Carlo Simulation of Proton-induced Cosmic-ray Cascades in the Atmosphere," http://nuclear.llnl.gov/simulation/doc_cry_v1.7.
- [75] D. Reyna, "A simple parameterization of the cosmic-ray muon momentum spectra at the surface as a function of zenith angle," *arXiv:hep-ph/0604145*.
- [76] M. Guan et al., "A parameterization of the cosmic-ray muon flux at sea-level," *arXiv:1509.06176*, 2015.
- [77] M. S. Gordon et al., "Measurement of the flux and energy spectrum of cosmic-ray induced neutrons on the ground," *Nuclear Science*, vol. 51, no. 6, 2004.
- [78] Corsika, "CORSIKA: an Air Shower Simulation Program," <https://www.ikp.kit.edu/corsika/>, 2017.
- [79] L. Ghys, S. Ihantola and J. Park, "Internal communication on the first release of the SoLid RO code," *SoLid DocDB*, 2016.
- [80] I. Pinera, "Status on cosmogenic muons and neutrons simulation," *SoLid Technical note*, 2016.
- [81] L. Michel, "Interaction between Four Half-Spin Particles and the Decay of the μ -Meson," *Proceedings of the Physical Society*, vol. 63, no. 5, 1949.
- [82] J. Beringer et al., "Summary tables: Leptons," *PDG booklet*, 2016.
- [83] L. Kalousis, "Muons and after muon events in SM1," *SoLid Technical note*, 2016.
- [84] The SoLid Collaboration, "The SoLid anti-neutrino detector's readout system," *JINST*, vol. 12, 2017.
- [85] V. Pestel, "Neutron calibration of the SoLid detector," *EPS poster*, 2017.
- [86] Coenen Plastics N.V., "," www.coenenplastics.be.

- [87] Saint-Gobain Crystals, "Assembly materials," *www.crystals.saint-gobain.com*, 2018.
- [88] L. Kalousis, "Internal communication on CosmicGen settings," *SoLid DocDB*, 2018.
- [89] Maja Verstraeten, "Internal Communication on Read-out simulation," *SoLid DocDB*, 2018.
- [90] Y. Abreu, "Internal communication on IBD simulation," *SoLid DocDB*, 2018.
- [91] CERN, "ROOT," *root.cern.ch*, 2018.
- [92] Daniel Saunders, "Internal Communication on triggers in Phase 1," *SoLid DocDB*, 2018.
- [93] D. Boursette, "Internal communication on cube reconstruction," *SoLid DocDB*, 2018.
- [94] S. Vercaemer, "Internal communication on muon veto time," *SoLid DocDB*, 2018.
- [95] Giel Vandierendonck, "Internal Communication on environmental correlations with muon rates," *SoLid DocDB*, 2018.
- [96] The MicroBooNE Collaboration, "Michel Electron Reconstruction Using Cosmic-Ray Data from the MicroBooNE LArTPC," *JINST*, vol. 12, no. 9, 2017.

